Faculdade de Engenharia da Universidade do Porto

A 2D Stress Analysis of Zirconia Dental Implants: A Comparison Study

Leonor Gonçalves Piqueiro

PROVISIONAL VERSION

Thesis submitted to Faculdade de Engenharia da Universidade do Porto as a requirement to obtain the MSc Degree in Bioengineering

Under the supervision of:
Professor Jorge Américo Oliveira Pinto Belinha
Professor Renato Manuel Natal Jorge

June, 2016

Resumo

Ao longo dos anos, a saúde da boca, bem como o sorriso têm ganho importância, devido ao facto de ser uma das mais importantes capacidades de comunicação de uma pessoa. De facto, a frequência de próteses dentárias removíveis entre os adultos variou entre 13 e 29%, enquanto a frequência das próteses dentárias fixas foi a maior na Suécia (45%) e na Suíça (34%). Ainda assim, os tratamentos de implantes dentários oferecem uma solução que poderá gerar resultados mais satisfatórios para pacientes que não se conseguem adaptar às dentaduras convencionais ou aqueles que já tenham comprometido o osso local.

Existem dois tipos de implantes dentários, que são as próteses dentárias removíveis (RDPs) e as próteses dentárias fixas (FDPs). Os tipos e restauração mencionados possuem nomes diferentes de acordo com a fixação (ou inexistência de fixação) ao osso. As próteses dentárias são aquelas que serão mais aprofundadas neste estudo. Estas próteses são constituídas por três elementos principais, que são a coroa, o abutment e o implante dentário propriamente dito.

A integridade biomecânica dos implantes compreende o comportamento mecânico dos materiais do implante, especialmente, Zircónia. As restaurações de zircónia possuem um papel importante nas FPDs, devido à sua vulnerabilidade mecânica.

Neste trabalho foram usadas técnicas avançadas de discretização numérica – meshless methods – mais especificamente, o Natural Neighbour Radial Point Interpolation Method (NNRPIM) e o Radial Point Interpolation Method (RPIM), mas também, o Método dos Elementos Finitos.

O principal objectivo deste trabalho foi compreender o comportamento mecânico dos implantes em zircónia e a resposta do tecido ósseo na presença destes implantes, bem como comparar os três métodos numéricos utilizados neste trabalho, FEM, RPIM e NNRPIM.

Os resultados obtidos mostram que os meshless methods são capazes de produzir campos de deslocamento e tensão mais precisos e suaves quando comparados com malhas de elementos finitos.

Página em branco

Abstract

Throughout the years, the health of the mouth and the smile have an increasing importance, due to the fact that is one of the most important interactive communication skills of a person. In fact, the frequency of removable dental prosthesis among adults varied between 13 and 29%, while the frequency of fixed dental prosthesis was the highest in Sweden (45%) and Switzerland (34%). Yet, dental implant treatments offers a solution that may generate more satisfactory outcomes for patients who are not able to adapt to conventional dentures or who have already compromised local host bone.

There are two types of dental implants, which are the removable dental prosthesis (RDPs) and the fixed dental prosthesis (FDPs). The aforementioned types of restorations have different names according to the fixation (or absence of fixation) to the bone. Fixed dental prostheses are the ones that will be mainly focused in this study. These prostheses are constituted by three key elements, which are the crown, the abutment and the dental implant itself. The biomechanical integrity of implants comprises the mechanical behavior of implant materials, especially zirconia. Zirconia restorations have found their indications for FPDs supported by teeth implants due to its mechanical reliability.

It was used advanced discretization numerical techniques – meshless methods – more specifically, the Natural Neighbour Radial Point Interpolation Method (NNRPIM) and the Radial Point Interpolation Method (RPIM), and also the Finite Element Method (FEM)

.The main goal of this work was to understand the mechanical behavior of zirconia implants and the bone tissue response in the presence of such implants and also compare the three numerical methods used in this work, FEM, RPIM and NNRPIM.

The results obtained show that meshless methods are capable to produce more accurate and smooth displacement and stress fields when compared to finite element meshes.

Página em branco

Acknowledgements/Agradecimentos

Em primeiro lugar, gostaria de agradecer ao Professor Jorge Belinha, pelo incansável apoio e por estar sempre disponível ao longo de todo este último semestre. Por todas as dúvidas esclarecidas, por todas as vezes que me ajudo a entender qual o melhor caminho a seguir após cada etapa.

Aos meus amigos Ana Faria, Ana Pereira, José Ribeiro, Madalena Peyroteo e Maria Magalhães por todos os almoços de quarta-feira, mas também por estes 5 anos incríveis que sem vocês não teriam sido a mesma coisa. Aprendi muito com vocês e espero continuar a aprender no futuro. Mas um obrigado especial à Madalena por me aturares 5 meses em Londres. Muito obrigado a todos.

Aos meus amigos do ginásio com quem passei uma boa parte da minha vida, são como uma segunda família para mim, sem dúvida. Por me ouvirem falar, mesmo que não vos interesse nada, por me animarem quando estou mais em baixo e por me terem permitido conquistar tanto. Quer ao nível pessoal, quer a nível técnico. Obrigada.

À Operação Tide 2014, só tenho a dizer 'Obrigada'. Obrigada por me terem deixado caminhar com vocês, aprender com vocês, viver com vocês, e tantas outras coisas que é difícil descrever por palavras. Muito Obrigada por me fazerem parte deste Caminho.

Ao meu irmão Henrique, por ser sempre o meu melhor amigo em todas as situações. Por me mostrar que vale sempre a pena lutar pelos nossos objetivos e que nada é impossível, basta querer e acreditar em nós mesmo. Obrigada por tudo.

Por fim, aos meus pais, muito obrigada, por me apoiarem sempre, em todas as situações e por acreditarem sempre em mim. Obrigada por me proporcionarem todas as aventuras que vivi até aqui, desde 5 meses em Londres, até uns dia na Colômbia. Obrigada por serem os meus maiores exemplos e por nunca me deixarem de desistir de nenhum sonho. Obrigada por tudo.

Página em branco

Funding

The author truly acknowledge the logistic conditions provided by Ministério da Educação e Ciência– Fundação para a Ciência e a Tecnologia (Portugal), under project funding UID/EMS/50022/2013 (funding provided by the inter-institutional projects from LAETA) and project NORTE-01-0145-FEDER-000022 - SciTech - Science and Technology for Competitive and Sustainable Industries, cofinanced by Programa Operacional Regional do Norte (NORTE2020), through Fundo Europeu de Desenvolvimento Regional (FEDER).
Additionally, the author truly acknowledge the work conditions provided by the department of Mechanical Engineering from FEUP and INEGI.

Página em branco

Índice

List of figures

List of tables

Abbreviations

DEM	Diffuse Element Method
EFGM	Element-Free Galerkin Method
FEM	Finite Element Method
GUI	Graphical User Interface
MFEM	Meshless Finite Element Method
MLPG	Meshless Local Petrov-Galerkin
MLS	Moving Least Square
NEM	Natural Element Method
NNFEM	Natural Neighbour Finite Element Method
NNRPIM	Natural Neighbour Radial Point Interpolation Method
PIM	Point Interpolation Method
RBF	Radial Basis Functions
RKPM	Reproducing Kernel Particle Method
RPIM	Radial Point Interpolation Method
SED	Strain Energy Density
SPH	Smooth Particle Hydrodynamics

Chapter 1

Introduction

Throughout the years, the importance of the health of the mouth and smile have increased, being one of the most important interactive communication skills of a person. Patients and consumers, now demand, not only a healthy mouth, but also a perfect smile. However, the main purpose of dental restorations is to replace missing teeth and, in addition, restore teeth that have been hardly damaged or, for any reason, are not aesthetic, either because of colour, form or contour.[1] In order to determine if a single missing tooth can be replaced, it is necessary in the first instance, to analyse if the tooth in question can be restored or not.[2]

1.1 Meshless Methods

There is a vast quantity of numerical methods, and they can be defined and classified by three fundamental modules: the field approximation (or interpolation) function, the used formulation and the integration.[3] From this point of view, it is possible to define the Finite Element Method (FEM) and the Meshless Methods as numerical methods.

The Finite Element Method was firstly developed to solve structural problems in the aerospace industry, in the early 1960s and, ever since, has been extended to solve a wide range of problems, from heat transfer to electromagnetics.[4]

The Finite Element Method is a very recognized and optimized method, often applied to a widespread variety of engineering fields, as well as to distinct sciences. According to this method, a more complex problem can be simplified by dividing the problem's domain into smaller elements, which are, usually, triangles. This means that the domain of the problem is discretized, and the field function is obtained by means of consecutive interpolations by simple functions, so called shape functions. In other words, instead of seeking a solution function for the entire domain, FEM intends to formulate the solution function for each element previously created and after combines them properly to obtain the solution for the whole domain. This method requires a mesh to divide the whole domain into smaller elements. The discretization

of the problem domain includes the process of creating the mesh, elements, their respective nodes and defining boundary conditions.[4,5]

This method is very effective and successful due to the local character of approximations, the ability to deal with complex geometrical domains and the existence of a large set of approximation schemes adapted to various problems but embedded in a unified formulation.[6]

Yet, FEM presents two major drawbacks. First, FEM's approximate solutions present limited regularity, by way of, the solution itself, in most cases, is continuous, but some of its derivatives are discontinuous at elements boundaries leading to difficulties of interpretation and the use of unsatisfactory smoothing techniques. Second, generating adequate discretization meshes is a difficult task, in particular, in complex three-dimensional domains. For example, as a result of the lack of efficient mesh generators able to dynamically adjust the size of each individual element, the development of auto-adaptive methods is limited.[6]

Thus, when analysing more complex geometries, FEM can easily generate highly distorted elements, causing shape functions to have low quality and compromising the performance of it.[5]

Considering the issues mentioned before, and with the intention to create new solutions that would fulfil the existing problems, meshless methods were created. Moreover, the stress and displacement fields produced with meshless methods, relating the analysis of structural problems, are, usually, much more uniform and close to the analytical solution than those created by low order element meshes (three and four nodes). On the contrary of Finite Element Methods, which uses the element mesh to obtain the approximation, meshless methods build the approximation based on nothing but an arbitrary nodal set, without any knowledge of the relation between nodes, at first instance.[7]

It was only in the middle 90s that meshless methods came into focus of interest for numerically solving partial differential equations, especially in the computational mechanics community.[3,8] Despite this fact, this methods have rapidly evolved, solving many of their initial problems, such as accuracy, imposition of essential boundary conditions, numerical integration, stability and many others.[9] The type of functions used initially for meshless methods were approximation functions, since the implementation of the influence-domain concept was easier and the background integration scheme was nodal independent.[3]

One of the first meshless method is the Smooth Particle Hydrodynamics (SPH) method, which was created to solve problems in astrophysics and, later on, fluid dynamics. Although SPH and their corrected versions were based on a strong form, other methods were based on a weak form. One of the first meshless methods based on a global weak form and one of the most popular, developed in 1994, was the Element-Free Galerkin method (EFGM).[7] This method was developed having in mind the concept created in the Diffuse Element Method (DEM), which, by its turn was the first meshless method using the Moving Least Square(MLS) approximants in the construction of the shape functions.[6] The Reproducing Kernel Particle Method (RKPM) was also

a very successful method and it was developed one year later than EFG, but this method has its origin in wavelets on the contrary to the Element-Free Galerkin method and was based in two different methods, the SPH and the Meshless Local Petrov-Galerkin (MLPG).[7] Meshless Methods have some major advantages such as *(i)* h-adaptivity is simpler to incorporate in Meshless Methods than in mesh-based methods *(ii)* problems with moving discontinuities such as crack propagation, shear bands and phase transformation can be treated with ease *(iii)* large deformation can be handled more robustly *(iv)* higher-order continuous shape functions *(v)* non-local interpolation character *(vi)* no mesh alignment sensitivity. Besides these improvements, there also some disadvantages, in particular, the fact that approximation Meshless Methods do not satisfy the Kronecker delta property, making the imposition of essential and natural boundary conditions difficult.[7] This is the immediate consequence, in the referred meshless methods, of using approximation functions instead of interpolation functions.[5]

Meanwhile, this obstacle was solved by exploring the advantages of both mesh-free methods and finite element methods, by means, hybrid methods, also called interpolation meshless methods.[7] Some of this newly developed meshless methods were the Point Interpolation Method (PIM), the Point Assembly Method, the Natural Neighbour Finite Element Method (NNFEM) or Natural Element Method (NEM) and the Meshless Finite Element Method (MFEM).[5] As a consequence of the evolution of the first meshless method, PIM, which initially used the original polynomial basis function, it was possible to start using a radial basis function for solving partial differential equations. This combination allows the generation of the Radial Point Interpolation Method (RPIM). The radial basis functions used in the first works done with this method were the Gaussian and the multiquadric radial basis functions.[5] Recently, having RPIM and the natural neighbours geometric concept as starting point, it was developed a new concept, the Natural Neighbour Radial Point Interpolation Method (NNRPIM).

1.1.1. Radial Point Interpolation Method

The Radial Point Interpolation Method started with the Point Interpolation Method.[10]

Having in mind that methods that uses MLS approximation for the construction of shape functions have issues related with the imposition of essential and natural boundary conditions, PIM was proposed.[10] Starting with only a group of arbitrarily distributed points, this technique consisted in constructing polynomial interpolants that possessed the Kronecker delta property as shape functions. This means that they pass through every single node, which fixes the issue of the essential and natural boundary imposition. However, this method has too many numerical problems. For instance, the perfect alignment of the nodes produces singular solutions in the interpolation function construction process. As a result, this technique evolved and originated the Radial Point Interpolation Method (RPIM). [3,11]

In order to stabilize the procedure, the Radial Basis Function (RBF) was added in the construction process of the interpolation function. In addition to the benefit mentioned before, the RBF allowed the removal of the possible singularities existent in PIM. Moreover, since the RPIM uses the concept of 'influence-domain', it creates sparse and banded stiffness matrices, which are more adequate to complex geometries problems.[3]

Due to all of the aforementioned advantages, together with the high convergence of the method, it is still used nowadays.

1.1.2. Natural Neighbour Radial Point Interpolation Method

The NNRPIM is one of the most recent developments in Radial Point Interpolators (RPI) and it uses the natural neighbour concept, which was firstly introduced by Sibson for data fitting and field smoothing.[12] This method results from the combination of the RPI and the Natural Neighbours geometric concept.[3]

The major difference between this method and the one described before, RPIM, is the way the nodal connectivity is enforced. In RPIM it was used the concept of 'influence-domain' and it is replaced by the 'influence-cell' concept, when considering the NNRPIM method.[3]

Having in mind the influence-cells, the NNRPIM relies on both geometrical (Voronoï diagrams[13]) and mathematical (Delaunay tessellation[14]) constructions. Hence, considering Voronoï cells, departing from an arbitrary set of nodes, a set of influence-cells are created. The Delaunay triangles, which are the dual of the Voronoï cells, are applied to create a node-depending background mesh used in numerical integration of the interpolation functions of the method in question.[3]

Due to the fact that NNRPIM interpolation functions, used in the Galerkin weak form, are constructed in a similar manner to the RPIM, it also possess the Kronecker delta property.[3] As a result of the way nodal connectivity is imposed, NNRPIM possesses smoother and more accurate displacements and stress fields when compared to results obtained with other methods, especially, FEM. Moreover, considering that the integration mesh is total dependent from the initial nodal distribution, NNRPIM can be considered a truly meshless method.

Even though NNRPIM is a recent developed meshless method, it already has been extended to numerous fields, such as the static analysis of isotropic and orthotropic plates, the functionally graded material plate analysis, the 3D shell-like approach for laminated plates and shells.[3]

Also, this method was already applied to biomechanics, with highlights to bone structures, since the non-convex boundaries and the material discontinuities in the bone structure, are easily handled by the NNRPIM. Because of this characteristics, meshless methods were already applied to bone tissue analysis and, more recently, Belinha and co-workers presented a new bone tissue remodelling algorithm relying on the meshless method accuracy.[3]

1.2 Objectives

The main purposes of this thesis are:

- Perform an elasto-static analysis of a dental implant, applying a concentrated load, using three numerical methods: FEM, RPIM and NNRPIM

- Compare the performance of all three methods, especially FEM, against the two meshless methods.

- Understand the mechanical behaviour of zirconia implants and the bone tissue response in the presence of such implants.

1.3 Document Structure

This thesis is composed by 7 main chapters, which are: Introduction, Meshless Methods, Solid Mechanics Fundamentals, FEMAS, Dental Implants, Numerical Examples and Conclusions and Future Work.

In the first chapter, **Introduction**, is presented a brief state-of-the-art regarding the origin of numerical methods, in particular, meshless methods in general and specifically the RPIM and NNRPIM. Also, the objectives of this work are defined.

In the second chapter, **Meshless Methods**, the two highlighted meshless methods are carefully presented, as well as their formulation.

In the third chapter, **Solid Mechanics Fundamentals**, it is presented and explained the basic notions of solid mechanics which are important to better understand some aspects of this work.

In the fourth chapter, **FEMAS**, it is presented and explained the software used in this thesis.

In the fifth chapter, **Dental Implants**, it is presented a state-of-the-art regarding dental implants, mainly considering their constitution, the materials and also the bone.

In the sixth chapter, **Numerical Examples**, are presented some works already done about the numerical problems solved along the development of this thesis. Also, using the software described in chapter 4, a dental implant is analysed and all the results obtained are presented.

In seventh chapter, **Conclusions and Future Work**, it is presented the conclusions about the work done and suggestions for possible works based on this one.

Chapter 2

Meshless Methods

The work here presented was developed having in mind two of the most recently developed meshless methods: the RPIM and the NNRPIM. After a brief description of the procedure of meshless methods in general and an overall presentation of RPIM and NNRPIM, it is now possible to present a thoroughly explanation of them both.

2.1 General Meshless Method Procedure

The outline respected by most meshless methods and the majority of other nodal dependent discretization numerical methods is as follows: first, it is necessary to study the problem geometry and establish the solid domain and the contour. Then, the essential and natural boundary conditions are identified, as it is possible to see in Figure 2.1a. Afterwards, as it is shown in Figure 2.1b and c, the problem domain and boundary is numerically discretized by a nodal set following a regular or irregular distribution.[3]

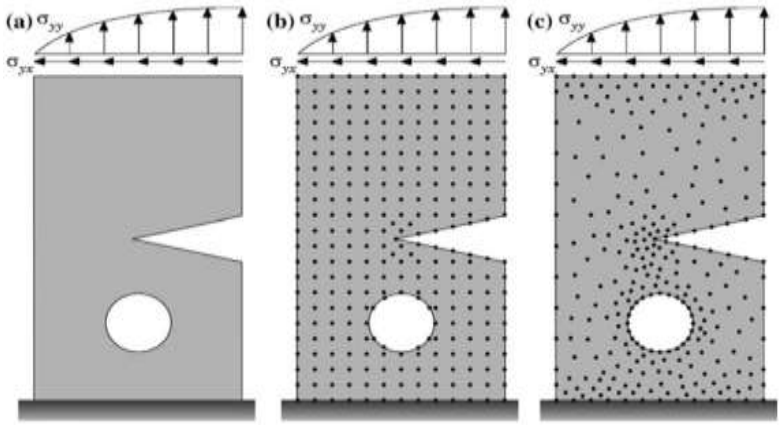

Figure 2.1 a. Problem domain with the essential and natural boundaries applied. **b.**Regular nodal discretization. **c.**Irregular nodal discretization[3]

Considering that it is not required, for meshless methods, any kind of previous information about the relation between the nodes towards the construction of the approximation (or interpolation) functions of the unknown variable field functions, the nodal distribution do not form a mesh. In fact, the only information necessary by truly meshless methods is the spatial location of each node discretized in the problem domain. The nodal discretization has a direct effect on the numerical analysis outcome and consequently, affects the method performance. An even nodal distribution as seen in Figure 2.1b leads, generally, to more accurate results and on the opposite, an uneven discretization of the nodes, Figure 2.1c, can often present lower accuracy. Despite this fact, locations with predictable stress concentrations, such as: domain discontinuities, crack tips, as seen in Figure 2.1 , among others, should present a higher nodal density when compared with locations in which smooth stress distributions are expected. In pursuance of solving both issues named before, it is possible to add extra nodes, only on the locations with predictable stress concentrations while maintaining a regular mesh on the rest of the problem domain, therefore, not increasing the computational cost significantly.[3]

Once it is obtained the problem domain discretization, it is now possible to get the nodal connectivity. While in FEM this is obtained using a predefined finite element mesh, in which it is known a priori which nodes belong to the same element and, consequently, interact directly between themselves. The boundary nodes interact with boundary nodes of nearby elements. On the other hand, in meshless methods, such connectivity is ensured by overlapping the influence-domains, when it comes to RPIM and influence-cells, when regarding NNRPIM.

Subsequently, it is created a background integration mesh, which can either be nodal dependent or independent, the later having a higher accuracy. The integration mesh can, at least, have the size of the problem domain, but in the cases in which it is larger, it cannot affect too much the final results. Afterwards, it is possible to obtain the field variables under study by using either approximation or interpolation shape functions, based on the combination of Radial Basis Functions (RBF) with polynomial basis functions.[3]

2.2 RPIM Formulation

2.2.1. Influence-domains and nodal connectivity

After the initial nodal discretization of the problem domain, it is necessary to impose the nodal connectivity between each and every node.

In order to find the nodal connectivity it is necessary to overlap the influence-domain of each node. The influence-domains are obtained through a process in which, firstly, it is settled an area (in case the problem is 2D) or a volume (in case the problem is 3D). Then, it is necessary to search for a specified number of nodes inside the previously established zone. As it is possible

to observe in Figure 2.2, there are influence-domains with different size and shape. Yet, the variation of this parameters along the problem domain affects the performance and the final solution of the meshless method. This said, it is important that all the influence-domains in the problem contain approximately the same number of nodes. Irregular domain boundaries or node clusters in the nodal distribution can lead to unbalanced influenced-domains. Regardless the used meshless technique, according to the literature, it is recommended using between n=[9,16] nodes for 2D problems and n=[27,70] nodes for 3D problems.[7,11,15-17]

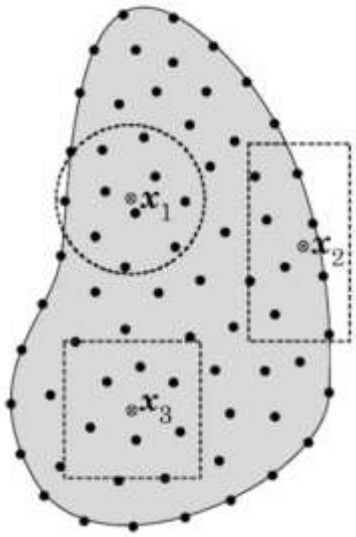

Figure 2.2 Influence-domains with different sizes and shapes[3]

The number of nodes inside each influence-domain does not depend on the density of the nodal discretization and once selected, the value is valid for all domain discretization within the same analysis.

2.2.2. Numerical Integration

Based on the RPIM, a new meshless method has recently proven better results than other meshless RPIM approaches based on Gauss-Legendre integration schemes. Even though using a stabilized nodal integration, the extra time spent in this process does not pay the increased accuracy of the final solution.[11,18] This said, in RPIM, the differential equations are integrated using the Gauss-Legendre integration scheme. In order to ensure this, firstly, a background mesh is created. The connection of the nodes discretizing the problem domain gives origin to cells. These are the ones that will later compose the background mesh.

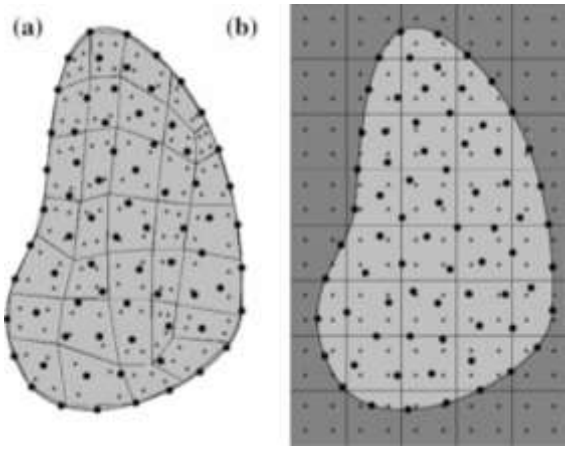

Figure 2.3 a. Fitted Gaussian background mesh. **b.**General Gaussian integration mesh.[3]

This mesh can either fit the solid-domain, as seen in Figure 2.3a, where no pos-treatment is needed, or, as it is possible to see in Figure 2.3b, be larger than the solid domain. In the latter case, the points outside the solid domain have to be removed.[3]

After all the solid domain is divided in a regular grid, each grid-cell is filled with integration points respecting the Gauss-Legendre quadrature rule. Taking as example Figure 2.4a, it is represented one grid-cell of the total background mesh. The initial quadrilateral is transformed in an isoparametric square, as seen in Figure 2.4b. Then, the Gauss-Legendre quadrature points are distributed inside the isoparametric square, and, in this case, it was used a 2x2 quadrature, Figure 2.4b.[19,20]

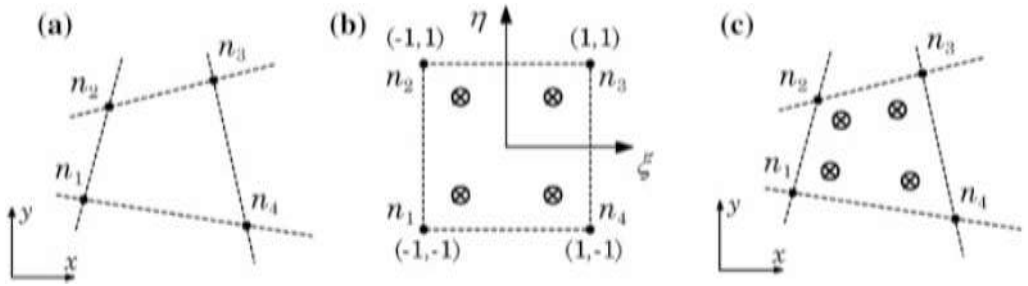

Figure 2.4 a. Initial grid-cell. **b.**Isoparametric square with integration points. **c.**Initial quadrature cell with integration points[3]

Later, with the intention to obtain the Cartesian coordinates of the quadrature points, isoparametric interpolation functions were used, and the results is the one presented in Figure 2.4c. The integration weight of the quadrature point is obtained multiplying the isoparametric weight of the quadrature point with the inverse of the Jacobian matrix determinant of the respective grid-cell.[3] The following tables display the location and the weights of the isoparametric integration points for quadrilateral and triangular element background meshes, respectively.

Table 2.1 Integration points coordinates and weights for quadrilateral ‘cells’.

Points	ξ	η	Weight	Representation
1	0	0	4	
a	$-\frac{1}{\sqrt{3}}$	$-\frac{1}{\sqrt{3}}$	1	
b	$+\frac{1}{\sqrt{3}}$	$-\frac{1}{\sqrt{3}}$	1	
c	$-\frac{1}{\sqrt{3}}$	$+\frac{1}{\sqrt{3}}$	1	
d	$+\frac{1}{\sqrt{3}}$	$+\frac{1}{\sqrt{3}}$	1	
a	$-\sqrt{3/5}$	$-\sqrt{3/5}$	$\frac{25}{81}$	
b	0	$-\sqrt{3/5}$	$\frac{40}{81}$	
c	$+\sqrt{3/5}$	$-\sqrt{3/5}$	$\frac{25}{81}$	
d	$-\sqrt{3/5}$	0	$\frac{40}{81}$	
e	0	0	$\frac{64}{81}$	
f	$+\sqrt{3/5}$	0	$\frac{40}{81}$	
g	$-\sqrt{3/5}$	$+\sqrt{3/5}$	$\frac{25}{81}$	
h	0	$+\sqrt{3/5}$	$\frac{40}{81}$	
i	$+\sqrt{3/5}$	$+\sqrt{3/5}$	$\frac{25}{81}$	

Table 2.2 Integration points coordinates and weights for triangular ‘cells’.

Points	ξ	η	Weight	Representation
a	$\frac{1}{3}$	$\frac{1}{3}$	$\frac{1}{2}$	
a	$\frac{1}{6}$	$\frac{1}{6}$	$\frac{1}{6}$	
b	$\frac{2}{3}$	$\frac{1}{6}$	$\frac{1}{6}$	OR
c	$\frac{1}{6}$	$\frac{2}{3}$	$\frac{1}{6}$	

a	$\frac{1}{3}$	$\frac{1}{3}$	$-\frac{27}{96}$	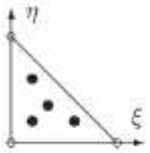
b	$\frac{1}{5}$	$\frac{1}{5}$	$\frac{25}{96}$	
c	$\frac{3}{5}$	$\frac{1}{5}$	$\frac{25}{96}$	
d	$\frac{1}{5}$	$\frac{3}{5}$	$\frac{25}{96}$	

2.3 NNRPIM Formulation

2.3.1. Natural Neighbours

First introduced in 1980, as a way to obtain influence-cells, the concept of natural neighbours was created and is used by the NNRPIM, in order to determine the nodal connectivity. In opposition to the RPIM, which relies on the use of influence-domains.[21] The influence-cells are determined based on the geometric and spatial relations between the Voronoï cells, obtained from the Voronoï diagram of the nodal distribution. This concept was firstly introduced by Sibson for data fitting and field smoothing.[12]

Initially it is necessary to consider a nodal set, N, discretized in the space domain $\Omega \in \mathbb{R}^2$, $N = \{n_1, n_2, \dots, n_N\}$, and also $X = \{x_1, x_2, \dots, x_X\}$. The Voronoï diagram of *N* is the assembly of *i* sub-regions V_i, closed and convex, in which, each sub-region is associated to the node n_i in a way that any point in the interior of V_i is closer to n_i than any other node n_j.[3]

$$V_i = \{x_I \in \mathbb{R}^2 : \|x_I - x_i\| < \|x_I - x_j\|, \forall i \neq j\} \quad \text{(eq. 2.1)}$$

being $\|.\|$ the distance between x_I, an interest point and the nodes with coordinates defined by x_i e x_j. Thus, the Voronoï diagram is defined by:

$$V = \{V_1, V_2, \dots, V_N\} \quad \text{(eq. 2.2)}$$

In Figure 2.5a, it is represented a nodal set in a two-dimensional space. Considering that the purpose is to determine the Voronoï cell V_0 of the node n_0, initially, it is necessary to choose the potential neighbours.[3]

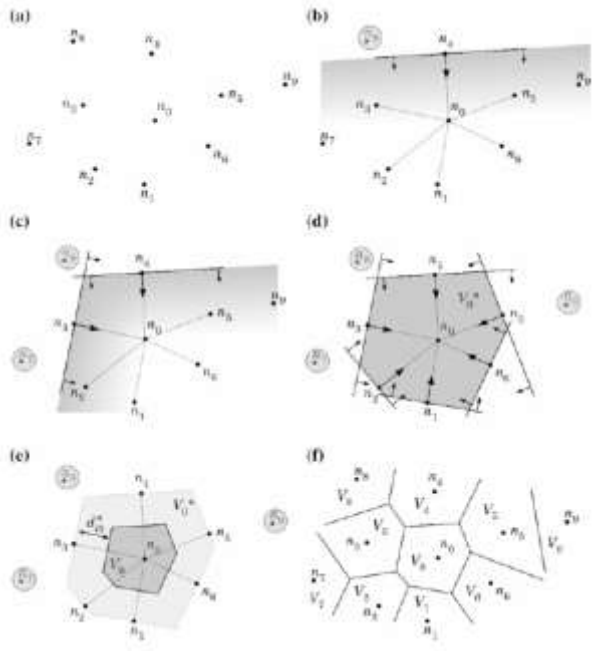

Figure 2.5 a. Initial nodal set. **b.**First trial plane. **c.**Second trial plane. **d.**Provisional Voronoï cell. **e.**Voronoï cell from node n_0. **f.**Voronoï diagram.[3]

The nodes that are not included in the provisional selection are discarded. After this step, one of the nodes is selected as potential neighbour, for instance node n_4, as seen in Figure 2.5b, it determined a vector u_{40}.

$$u_{40} = \frac{(x_0 - x_4)}{\|x_0 - x_4\|} \qquad \text{(eq. 2.3)}$$

In which $u_{40} = \{u_{40}, v_{40}, w_{40}\}$. Afterwards a plane is defined. All the nodes that do not respect the following condition are discarded:

$$u_{40}x + v_{40}y + w_{40}z \geq (u_{40}x_4 + v_{40}y_4 + w_{40}z_4) \qquad \text{(eq. 2.4)}$$

This procedure is repeated for each and every node of the initial set of nodes, as it is possible to observe in Figure 2.5c. In Figure 2.5d, it is represented all of the 6 natural neighbours of node n_0, and it is possible to see that nodes n_7, n_8 and n_9 does not belong to the referred cluster, because they do not respect the equation 2.4, mentioned before.[3]

Having already obtained the provisional Voronoï cell, it is now possible to obtain a definitive one, as shown in Figure 2.5e. The distance between node n_0 and the boundary of the Voronoï cell, V_0 is half of node's n_0 and the neighbour node in question Euclidian norm. So, this distance is given by the following equation:

$$d_{0i}^{*} = \frac{d_{0i}}{2} = \frac{\|x_0 - x_i\|}{2} \qquad \text{(eq. 2.5)}$$

In order to obtain the remaining Voronoi cells, a similar procedure is applied, as seen in Figure 2.5f.[3]

2.3.2. Influence-Cells and Nodal Connectivity

As mentioned before in this work, in meshless methods, the nodal connectivity is obtained by overlapping the influence-domains of each interest point. In order to respond to difficulties that can affect the efficiency of the meshless methods when using blind influence-domains, the concept of influence-cells was created.[22]

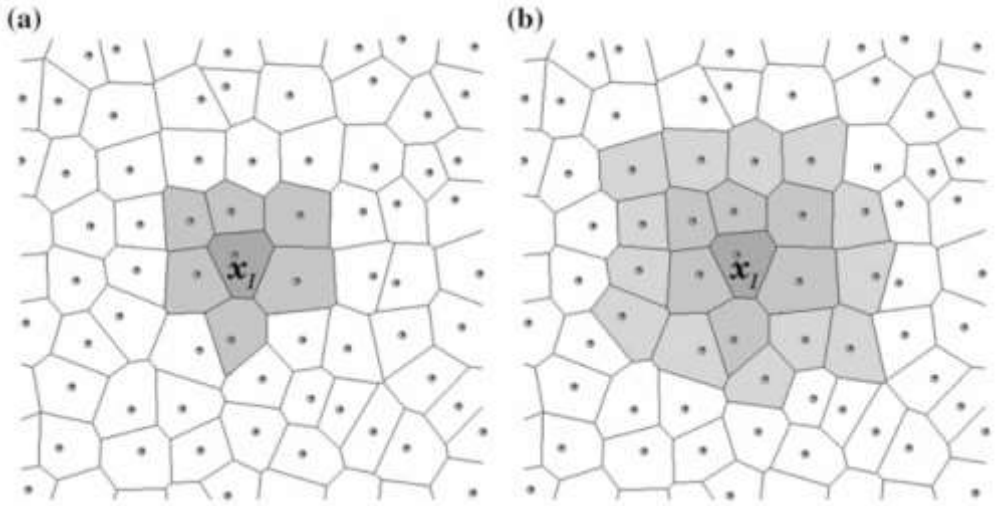

Figure 2.6 a. First degree influence-cell. **b.**Second degree influence-cell.[3]

Regarding the level of nodal connectivity, influence-cells can be either "First degree influence-cells" or "Second degree influence-cells", as seen in Figure 2.6a and 2.6b, respectively. According to the literature, "First degree influence-cells" are composed by only these natural neighbours and "Second degree influence-cells" contain, not only the first degree natural neighbour of a certain point of interest, but also, the natural neighbours of all the nodes belonging to the first degree of influence cells. Thus, the first degree influence-cell is naturally smaller than the second degree influence-cell. Therefore, as expected, the use of second degree influence-cells generally leads to better numerical results.

2.3.3. Numerical Integration

The Natural Neighbour Radial Point Interpolation Method (NNRPIM) uses a nodal based integration scheme proposed by Belinha and co-workers[3] The most important advantage of this scheme is that the background integration scheme is constructed using uniquely the nodal distribution spatial information. Since there is no information besides the spatial location of

the nodes discretizing the problem domain, is also necessary to: establish the nodal connectivity, determine the integration points and construct the shape functions. Hence, following the construction of the Voronoï diagram, it is possible to obtain a nodal dependent integration mesh based purely on the nodal distribution spatial information.

In order for this to be done, it is necessary to divide each of the Voronoï cells of the previously obtained Voronoï diagram and divide them into smaller sub-cells.

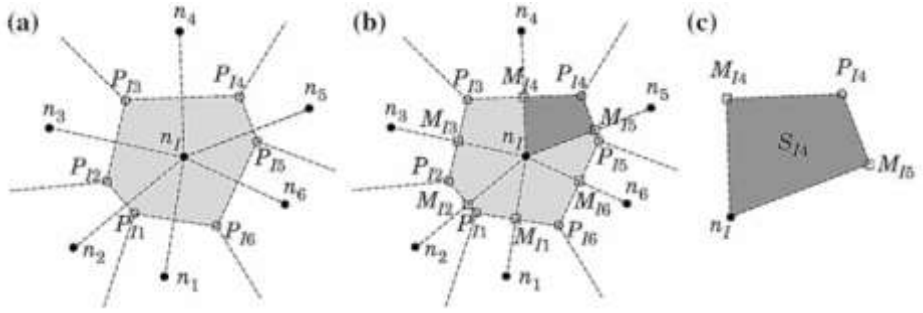

Figure 2.7 a. Voronoï cell and respective intersection points (P_{Ii}). **b.**Middle points (M_{Ii}) and the respective generated quadrilaterals. **c.**Quadilateral[3]

In Figure 2.7a is possible to observe a constructed Voronoï cell, V_I, of node n_I, based on its natural neighbours. Afterwards, the corners P_{Ii} of the polygonal shape defined by V_I are determined, Figure 2.7a. Then, the middle points, M_{Ii}, between n_I and each neighbour node, n_i are obtained, Figure 2.7b. Hence, the Voronoï cells are divided in n quadrilateral sub-cells, S_{Ii}, in which n is the number of natural neighbours of node n_I, as seen in both Figure 2.7b and 2.7c.

If the N nodes discretizing the problem domain are irregularly scattered, the sub-cells that are originated are quadrilateral, on the other hand, if the field nodes N discretizing the problem domain are scattered in a regular nodal distribution, the Voronoï cells are divided in triangles, as sub-cells, instead of quadrilateral, as seen in Figure 2.8.

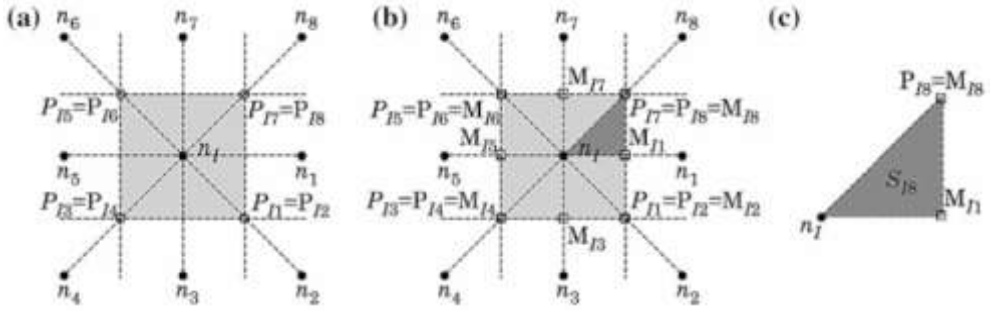

Figure 2.8 a. Voronoï cell and respective intersection points (P_{Ii}). **b.**Middle points (M_{Ii}) and the respective generated quadrilaterals. **c.**Quadilateral[3]

The procedure to obtain sub-cells in case of a regular discretization of the problem domain is the same mentioned previously for the case of an irregular discretization of the problem domain. Due to the fact that it is always possible to divide a Voronoï cell, V_I, in n sub-cells, S_{Ii},

being n the total number of natural neighbours of n_i, therefore, the area of the Voronoï cell, V_I, can be determined using the area of the n sub-cells S_{Ii}:

$$A_{V_I} = \sum_{i=1}^{n} A_{S_{Ii}}, \forall A_{S_{Ii}} \geq 0 \qquad \text{(eq. 2.6)}$$

In which, A_{V_I} is the area of the Voronoï cell V_I and $A_{S_{Ii}}$ is the area of the sub-cell S_{Ii}.

In order to obtain the simplest integration scheme that can be established, using sub-cells with either triangular or quadrilateral shape, a single integration point is placed in the barycentre of the sub-cells. Consequently, spatial location of each integration point is determined on each sub-cell, Figure 2.9, being the weight of each integration point the area of the respective sub-cell.

The example pictured below only uses 1 integration point in each cell. However, it is possible to add more integration points.

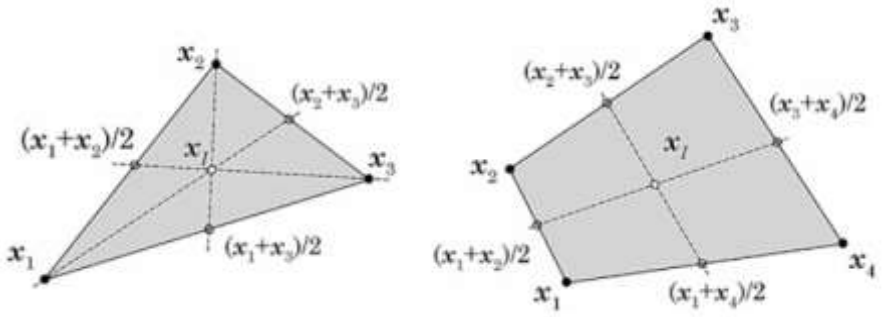

Figure 2.9 Triangular and quadrilateral shapes and the respective integration points.[3]

Regarding this subject, initially, the sub-cell is divided again, although this time only as quadrilaterals, as seen in Figure 2.10, then, it is possible to apply the Gauss-Legendre quadrature to the obtained sub-quadrilaterals in order to obtain the integration points.[19,20]

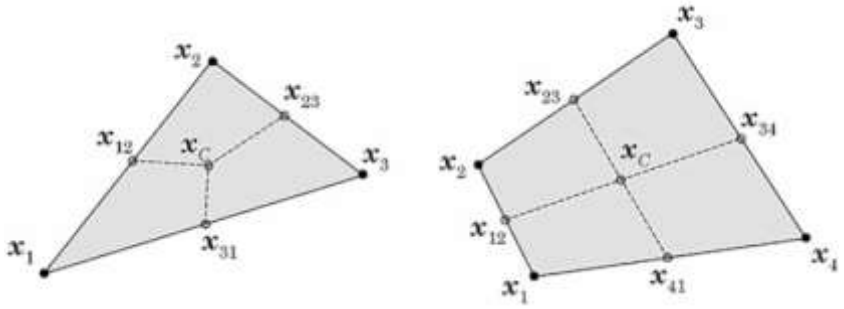

Figure 2.10 Division in quadrilaterals of the sub-cells[3]

Afterwards, the process follows as it was described, in section 2.2.2, for the RPIM using quadrilateral integration. The resultant integration is as follows, in Figure 2.11.

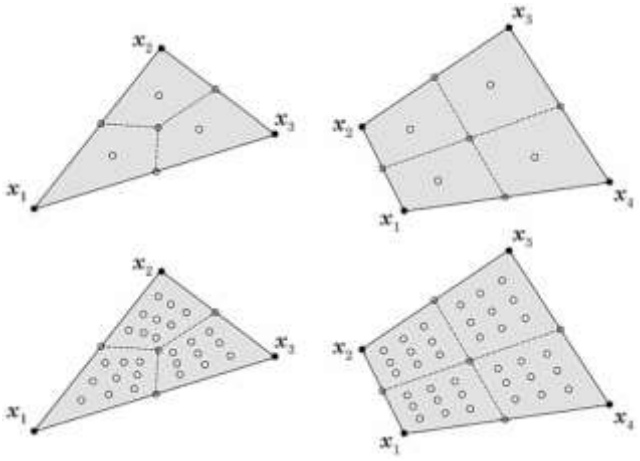

Figure 2.11 Triangular and rectangular shape and respective integration points, x_I, using the Gauss-Legendre integration scheme.[3]

In Figure 2.11 are shown distinct integration schemes for the triangular and the quadrilateral sub-cells. Nevertheless, adding more integration points does not increase significantly the solution accuracy and, in addition, greatly increases the computational cost.[3] Therefore, this work follows the suggestion from Belinha[3] and only uses one integration point per sub-cell. The domain integration mesh is obtained by repeating this process for the remaining Voronoï cells.

2.4 Shape Functions

Since the shape functions construction methodology should be able to use only the nodes discretizing the domain without the need of any pre-established mesh providing the nodal connectivity, its construction and development assume great importance in meshless methods.[7]

Both RPIM and NNRPIM use the same shape functions, based on a combination of radial basis functions with polynomial functions. The combination of these functions eliminates some issues such as the possible singularities created by methods that only use polynomial functions.[11,18]

One of the biggest advantages of both these method's shape functions is that they possess the Kronecker delta property, meaning that they are interpolating shape functions.

First of all, it is necessary to consider an influence domain that has a set of arbitrarily distributed nodes $P_i(x_i)$ $(i = 1,2,\dots,n)$, being *n* the number of nodes in the influence domain of $\boldsymbol{x}$ and consider, also, a shape function (in this case, approximation function) $u(\boldsymbol{x})$ in the referred influence domain. Radial PIM constructs the approximation functions $u(\boldsymbol{x})$ to pass through all these node points using radial basis function (RBF), $B_i(\boldsymbol{x})$, and polynomial basis function, $P_j(\boldsymbol{x})$.[11,18]

Thus,

$$u(x) = \sum_{i=1}^{n} B_i(x)a_i + \sum_{j=1}^{m} P_j(x)b_j = B^T(x)a + P^T(x)b \qquad \text{(eq. 2.7)}$$

In equation 2.7, a_i is the coefficient for $B_i(\boldsymbol{x})$, and b_j is the coefficient for $P_j(\boldsymbol{x})$. Moreover, *n* is the number of nodes in an domain of $\boldsymbol{x}$, *m* is the polynomial term which is usually $m < n$.

In equation 2.8 are defined the vectors

$$\begin{aligned} a &= [a_1, a_2, a_3, \dots, a_n]^T, \\ b &= [b_1, b_2, b_3, \dots, b_m]^T, \\ B^T &= [B_1(x), B_2(x), B_3(x), \dots, B_n(x)], \\ P^T &= [P_1(x), P_2(x), P_3(x), \dots, P_m(x)], \end{aligned} \qquad \text{(eq. 2.8)}$$

Above is defined the radial basis function, which is a function of distance r:

$$\begin{aligned} B_i(x) &= B_i(r_i) \\ r_i &= \sqrt{[(x - x_i)^2 + (y - y_i)^2]} \end{aligned} \qquad \text{(eq. 2.9)}$$

The monomial terms of the polynomial basis functions are as follows:

$$P^T(x) = [1, x, y, x^2, xy, y^2, \dots] \qquad \text{(eq. 2.10)}$$

The radial term transforms a multidimension into one-dimension, and the polynomial term improves the polynomial accuracy of the interpolation. According to Wang et al[18] and his research, addition of polynomial terms does not improve greatly the accuracy for non-polynomial functions, but it was revealed that there was no guarantee that the interpolating condition could be satisfied without the addition of polynomial terms.

Additionally, the coefficients should be constrained in order to assure the uniqueness of the interpolation. Constrains presented in equation 2.11 are usually imposed:

$$\sum_{i=1}^{n} P_j(x_i, y_i) a_i = 0, \; j = 1,2, \dots, m \qquad \text{(eq. 2.11)}$$

It can be expressed in matrix form, as follows:

$$\begin{bmatrix} B_0 & P_0 \\ P_0^T & 0 \end{bmatrix} \begin{Bmatrix} a \\ b \end{Bmatrix} = \begin{Bmatrix} u^e \\ 0 \end{Bmatrix} \quad or \quad G \begin{Bmatrix} a \\ b \end{Bmatrix} = \begin{Bmatrix} u^e \\ 0 \end{Bmatrix} \qquad \text{(eq. 2.12)}$$

The distance is directionless, $B_k(x_i, y_i) = B_i(x_k, y_k)$. If the inverse of the matrix **G** exists, consequently, it is possible to obtain a unique solution:

$$\begin{Bmatrix} a \\ b \end{Bmatrix} = G^{-1} \begin{Bmatrix} u^e \\ 0 \end{Bmatrix} \qquad \text{(eq. 2.13)}$$

As result, the interpolation is expressed as:

$$u(x) = [B^T(x)P^T(x)]G^{-1}\begin{Bmatrix} u^e \\ 0 \end{Bmatrix} = \varphi(x)u^e \quad \text{(eq. 2.14)}$$

Being $\varphi(x)$ the shape function defined by:

$$\varphi(x) = [\Phi_1(x), \Phi_2(x), \dots, \Phi_i(x), \dots, \Phi_n(x)] \quad \text{(eq. 2.15)}$$

Since shape functions from both RPIM and NNRPIM, as already said, respect the Kronecker delta property,

$$\varphi_i(x_j) = \begin{cases} 1, & i = j, \ \ j = 1,2,\dots,n \\ 0, & i \neq j, \ \ j = 1,2,\dots,n \end{cases} \quad \text{(eq. 2.16)}$$

This means they pass through every single node within the influence-domain (or influence-cell), in opposition to approximation shape functions which do not. When comparing approximation shape functions to interpolation shape function, the latter ones have reduced computational costs associated, due to using direct imposition methods, which allows to easily impose the essential and natural boundary conditions.[11,18]

Chapter 3

Solid Mechanics Fundamentals

Solids and structures subjected to loads or forces become stressed. The stresses lead to strains, which can be interpreted as deformations or relative displacements. Solid mechanics aim is to understand the relationship between stress and strain, as well as, the relationship between strain and displacements.[3] Depending on the solid material stress-strain curve, solids can show different behaviours.

In the present work, all solids were considered as being linear-elastic, it means that the relationship between stress and strain is assumed to be linear and after the removal of the applied load, the solid returns to its undeformed shape. Additionally, since this is a static study, only static loads were applied and considered, meaning that stresses, strains and displacements are not considered as a function of time.

Also, there are anisotropic and isotropic materials. The first ones are materials in which the properties varies with the directions. On this type of materials the deformation caused by a load applied in a certain direction is different from the deformation caused by the same load applied in a different direction. Isotropic materials are a special case of anisotropic materials, since only two independent material properties need to be known, the Young modulus (E) and the Poisson ratio (v). In this work, only isotropic material were used.[3]

3.1 Stress Components

Due to the application of external loads, internal forces are produced. As represented in equation 3.1, these internal forces are defined by the variation of force per unit of area and are entitled stress.

$$T = \lim_{\Delta A \to 0} \frac{\Delta F}{\Delta A} \qquad \text{(eq. 3.1)}$$

On a certain point, the stress a body is under is given by the following stress tensor:

$$\tau = \begin{bmatrix} \sigma_{xx} & \tau_{xy} & \tau_{xz} \\ \tau_{yx} & \sigma_{yy} & \tau_{yz} \\ \tau_{zx} & \tau_{zy} & \sigma_{zz} \end{bmatrix} \quad \text{(eq. 3.2)}$$

This tensor can also be written as a vector:

$$\sigma = \{\sigma_{xx}\sigma_{yy}\sigma_{zz}\tau_{xy}\tau_{yz}\tau_{zx}\}^{T} \quad \text{(eq. 3.3)}$$

Stress can be divided into two categories, normal stress, which is perpendicular to the plane in question, denotes by the letter σ and shear stress, which is tangential to the plane in which it acts, denoted by the letter τ.[23]

3.2 Equilibrium equations

Although stresses vary according to the volume of the body, these cannot vary randomly between two given points. An infinitesimal element is characterized by three dimensional equilibrium equation, which are:

$$\begin{aligned} \frac{\partial_{\sigma_{xx}}}{\partial_x} + \frac{\partial_{\tau_{yx}}}{\partial_y} + \frac{\partial_{\tau_{zx}}}{\partial_z} + F_x = 0 \\ \frac{\partial_{\tau_{xy}}}{\partial_x} + \frac{\partial_{\sigma_{yy}}}{\partial_y} + \frac{\partial_{\tau_{zy}}}{\partial_z} + F_y = 0 \\ \frac{\partial_{\tau_{xz}}}{\partial_x} + \frac{\partial_{\tau_{yz}}}{\partial_y} + \frac{\partial_{\sigma_{zz}}}{\partial_z} + F_z = 0 \end{aligned} \quad \text{(eq. 3.4)}$$

And must be verified for every point throughout the volume of the body.[23]

3.3 Components of strain

Due to the fact that no material is perfectly rigid, when subject to external loads, a body will become deformed. Regarding the deformable body presented in Figure 3.1, prior to applying any external loads, point Q was in a certain space location, but as soon as external loads are applied, this leads to a change on the location giving origin to any point location, q.

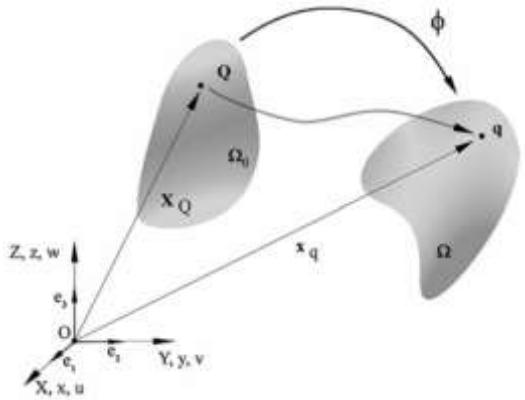

Figure 3.1 Linear deformation of a virtual body[3]

The equation that defines the displacement field, for any given point of the solid is:

$$u(u,v,w) = \begin{Bmatrix} u(x,y,z) \\ v(x,y,z) \\ w(x,y,z) \end{Bmatrix} \qquad \text{(eq. 3.5)}$$

Strain and displacements are related according to the following equations,

$$\begin{array}{ll} \varepsilon_{xx}\dfrac{\partial u}{\partial x} & Y_{xy} = \dfrac{\partial v}{\partial x} + \dfrac{\partial u}{\partial y} \\ \varepsilon_{yy}\dfrac{\partial v}{\partial y} & Y_{yz} = \dfrac{\partial w}{\partial y} + \dfrac{\partial v}{\partial z} \\ \varepsilon_{zz}\dfrac{\partial w}{\partial z} & Y_{zx} = \dfrac{\partial u}{\partial z} + \dfrac{\partial w}{dx} \end{array} \qquad \text{(eq. 3.6)}$$

Similarly to what happens in stress, there is also two types of strain. The normal strain, which can be represented by the letter ε, and represents the relative change of length of a certain line segment. On the other hand, the shear strain is represented by the letter γ and refers to the change in angle of two previously perpendicular line segments.[23]

The strain tensor comes:

$$\varepsilon = \begin{bmatrix} \varepsilon_{xx} & \gamma_{xy} & \gamma_{xz} \\ \gamma_{yx} & \gamma_{yy} & \gamma_{yz} \\ \gamma_{zx} & \gamma_{zy} & \varepsilon_{zz} \end{bmatrix} \qquad \text{(eq.3.7)}$$

The equations presented in 3.6 can be represented in matrix form as the product of the partial differential equation operator matrix ***L*** and the displacement field ***u***.

$$\varepsilon = \boldsymbol{Lu} \qquad \text{(eq.3.8)}$$

Where ***L*** is given by,

$$\boldsymbol{L} = \begin{bmatrix} \frac{\partial}{\partial x} & 0 & 0 & \frac{\partial}{\partial y} & 0 & \frac{\partial}{\partial z} \\ 0 & \frac{\partial}{\partial y} & 0 & \frac{\partial}{\partial x} & \frac{\partial}{\partial z} & 0 \\ 0 & 0 & \frac{\partial}{\partial z} & 0 & \frac{\partial}{\partial y} & \frac{\partial}{\partial x} \end{bmatrix}^{\boldsymbol{T}} \qquad \text{..... (eq. 3.9)}$$

3.4 Constitutive equations

Due to all solids considered in this work were isotropic, besides the fact that not only is the material completely defined by just its Elastic Modulus and Poisson's ratio, but also, by the components of stress and strain relation, which is given by the generalized Hooke's Law.[23]

$$\boldsymbol{\sigma} = \boldsymbol{c}\,\boldsymbol{\varepsilon} \qquad \text{(eq. 3.10)}$$

In which, c is the constitutive matrix of the material, defined by:

$$\boldsymbol{c} = \frac{E}{(1+\nu)(1-2\nu)} \begin{bmatrix} 1-\nu & \nu & \nu & 0 & 0 & 0 \\ \nu & 1-\nu & \nu & 0 & 0 & 0 \\ \nu & \nu & 1-\nu & 0 & 0 & 0 \\ 0 & 0 & 0 & (1-2\nu) & 0 & 0 \\ 0 & 0 & 0 & 0 & (1-2\nu) & 0 \\ 0 & 0 & 0 & 0 & 0 & (1-2\nu) \end{bmatrix} \qquad \text{(eq. 3.11)}$$

This constitutive matrix can also be obtained by inverting the compliance elasticity matrix, $c = s^{-1}$. In equations 3.12 and 3.13 are defined the plane stress and plane strain, respectively, for the general anisotropic material case, the compliance elasticity matrix *s*.

$$S_{plane\ stress} = \begin{bmatrix} \frac{1}{E_{11}} & -\frac{\nu_{21}}{E_{22}} & 0 \\ -\frac{\nu_{12}}{E_{11}} & \frac{1}{E_{22}} & 0 \\ 0 & 0 & \frac{1}{G_{12}} \end{bmatrix} \qquad \text{(eq. 3.12)}$$

$$S_{plane\ strain} = \begin{bmatrix} \frac{1-\nu_{31}\nu_{13}}{E_{11}} & -\frac{\nu_{12}+\nu_{31}\nu_{23}}{E_{22}} & 0 \\ -\frac{\nu_{12}+\nu_{32}\nu_{13}}{E_{11}} & \frac{1-\nu_{32}\nu_{23}}{E_{22}} & 0 \\ 0 & 0 & \frac{1}{G_{12}} \end{bmatrix} \qquad \text{(eq. 3.13)}$$

being E_{ij} the elastic modulus, ν_{ij} the material Poisson coefficient and G_{ij} the distortion modulus in material direction *i* and *j*. It is possible to align the constitutive matrix c with a new material referential *Ox'y'* defined by $i' = \{i'_x, i'_y\}$ and $j' = \{-i'_y, i'_x\}$, which are versors of the new material referential. Hence,

$$c' = T^T c T \qquad \text{(eq. 3.14)}$$

where the transformation matrix T is defined by,

$$T = \begin{bmatrix} cos^2\,\alpha & sin^2\,\alpha & -\sin 2\alpha \\ sin^2\,\alpha & cos^2\,\alpha & \sin 2\alpha \\ \sin\alpha\cdot\cos\alpha & -\sin\alpha\cdot\cos\alpha & cos^2\alpha - sin^2\alpha \end{bmatrix} \quad \text{(eq. 3.15)}$$

the angle α is the angle between the original material axis *Ox* and the new material axis O'_x: $\alpha = \cos^{-1}(i \cdot i')$.

3.5 Strong form and weak form formulation

The partial differential system equations are strong forms of the governing system of equations for solids. The strong form, in contrast to a weak form, requires strong continuity on the dependent field variables. Whatsoever functions that define these field variables have to be differentiable up to the order of the partial differential equations that exist in the strong form of the system. On the other hand, the weak form requires a weaker consistency on the adopted approximation (or interpolation) functions.

By reason of the weaker requirements on the field variables, and the integral operation, a formulation based on a weak form, usually produces a set of discretized system equations that give much more accurate results, especially for problems of complex geometry. These are the reasons why so many prefer the weak form to obtain the approximated solution. However, accuracy is dependent on the density of the mesh discretizing the problem domain.[3,24]

3.5.1. Galerkin weak form

The Galerkin weak form is a variational principle based on the energy principle. Between all possible displacement configurations satisfying the compatibility conditions, the essential boundary conditions and the initial and final time conditions, the real solution correspondent configuration in the one that minimizes the Lagrangian functional **L**,

$$L = T - U + W_f \quad \text{(eq. 3.16)}$$

Where T is the kinetic energy, U is the strain energy and W_f is the work produced by the external forces.

The variables above can be replaced by the equations that defines them, which can be written as,

$$L = \frac{1}{2}\int_\Omega \rho \mathring{\mathbf{u}}^T \mathring{\mathbf{u}}\, d\Omega - \frac{1}{2}\int_\Omega \varepsilon^T \sigma\, d\Omega + \int_\Omega u^T b\, d\Omega + \int_{\Gamma_t} u^T f\, d\Gamma \quad \text{(eq. 3.17)}$$

Where the solid volume is defined by Ω, $\mathring{u}$ is the displacement first derivative with respect to time and ρ is the solid mass density. ε is the strain vector and σ is the stress vector. Lastly, u represents the displacement, b the body forces and Γ_t the traction boundary where the external forces f are applied.

Minimizing equation 3.17, the following is obtained:

$$\delta \int_{t_1}^{t_2} \left[\frac{1}{2} \int_{\Omega} \rho \mathring{u}^{\,T} \mathring{u} \, d\Omega - \frac{1}{2} \int_{\Omega} \varepsilon^T \sigma \, d\Omega + \int_{\Omega} u^T b \, d\Omega + \int_{\Gamma_t} u^T f \, d\Gamma \right] dt = 0 \qquad \text{(eq. 3.18)}$$

Moving the variation operator δ inside the integrals,

$$\int_{t_1}^{t_2} \left[\frac{1}{2} \int_{\Omega} \delta(\rho \mathring{u}^{\,T} \mathring{u}) d\Omega - \frac{1}{2} \int_{\Omega} \delta(\varepsilon^T \sigma) d\Omega + \int_{\Omega} \delta u^T b \, d\Omega + \int_{\Gamma_t} \delta u^T f \, d\Gamma \right] dt = 0 \qquad \text{(eq. 3.19)}$$

Due to the fact that in this work only static problems were considered, the first term of the equation 3.19 can be discard, which leads to:

$$\int_{t_1}^{t_2} \left[-\frac{1}{2} \int_{\Omega} \delta(\varepsilon^T \sigma) d\Omega + \int_{\Omega} \delta u^T b \, d\Omega + \int_{\Gamma_t} \delta u^T f \, d\Gamma \right] dt = 0 \qquad \text{(eq. 3.20)}$$

Considering the equation 3.20, there are some simplifications that can be made to the first term of the integral. The integrand function can be written as:

$$\delta(\varepsilon^T \sigma) = \delta \varepsilon^T \sigma + \varepsilon^T \delta \sigma \qquad \text{(eq. 3.21)}$$

Since both terms are scalars, in equation 3.21,

$$\varepsilon^T \delta \sigma = (\varepsilon^T \delta \sigma)^T = \delta \sigma^T \varepsilon \qquad \text{(eq. 3.22)}$$

According to the generalized Hooke's law shown in 3.10, and the symmetric property of material shown in 3.11, $c^T = c$, it is possible to write:

$$\delta \sigma^T \varepsilon = \delta \varepsilon^T \sigma \qquad \text{(eq. 3.23)}$$

Hence, by replacing equation 3.23 in equation 3.21,

$$\delta(\varepsilon^T \sigma) = 2(\delta \varepsilon^T \sigma) \qquad \text{.....(eq. 3.24)}$$

Substituting equation 3.24 in equation 3.20

$$\int_{t_1}^{t_2} \left[- \int_{\Omega} \delta(\varepsilon^T \sigma) d\Omega + \int_{\Omega} \delta u^T b \, d\Omega + \int_{\Gamma_t} \delta u^T f \, d\Gamma \right] dt = 0 \qquad \text{.....(eq. 3.25)}$$

If it is pretended for the time integration to be valid for any pair of initial and final time, t_1 and t_2, respectively, the integrand from equation 3.25 must be null. This leads to the "Galerkin weak form" equation,

$$-\int_{\Omega} \delta\varepsilon^T \sigma d\Omega + \int_{\Omega} \delta u^T b \, d\Omega + \int_{\Gamma_t} \delta u^T f \, d\Gamma = 0 \qquad \text{(eq. 3.26)}$$

Replacing equations 3.8 and 3.10 In equation 3.26, the generic Galerkin weak form written in terms of displacement is obtained,

$$\int_{\Omega} \delta(\boldsymbol{L}\,\boldsymbol{u})^T \boldsymbol{c}\,(\boldsymbol{L}\,\boldsymbol{u}) d\Omega - \int_{\Omega} \delta u^T b \, d\Omega - \int_{\Gamma_t} \delta u^T f \, d\Gamma = 0 \qquad \text{(eq. 3.27)}$$

3.6 Discrete System Equations

Having as base the principle of virtual work, the discrete equations for meshless methods are obtained by using the meshless shape functions as trial and test functions. The meshless trial function $u(x_I)$ Is given by,

$$u(x_i) = \sum_{i=1}^{n} \varphi_i(x_I) u_i \qquad \text{(eq. 3.28)}$$

in which $\varphi_i(x_I)$ is the meshless approximation or interpolation function and u_i are the nodal displacements of the *n* nodes belonging to the influence-domain of interest node x_i.

It is known that the NNRPIM interpolation function satisfies the condition,

$$\varphi_i(x_j) = \delta_{ij} \qquad \text{(eq. 3.29)}$$

Where δ_{ij} is the Kronecker delta, being $\delta_{ij} = 1 \; if \; i = j$ and $\delta_{ij} = 0 \; if \; i \neq j$.

Following equation 3.24, the test function (or virtual displacements) are defined as,

$$du(x_i) = \sum_{i=1}^{n} \varphi_i(x_I) du_i \qquad \text{(eq. 3.30)}$$

Where du_i are the nodal values for the test function.

Since that in the presented work it was studied only two-dimensional problems considering the plane strain or the plane stress assumptions, each node x_i discretizing the problem domain has two degrees of freedom: $u_i = \{u_i, v_i\}$. Thus, in order to interpolate the virtual displacement at the interest point x_I, it is possible to write:

$$\delta u(x_I) = \delta u_I = I\begin{Bmatrix}\phi_I\\ \phi_I\end{Bmatrix}\delta u_s = \begin{bmatrix}\varphi_1(x_I) & 0 & \dots & \varphi_n(x_I) & 0\\ 0 & \varphi_1(x_I) & \dots & 0 & \varphi_n(x_I)\end{bmatrix}\begin{Bmatrix}\delta u_1\\ \delta v_1\\ \dots\\ \delta u_n\\ \delta v_n\end{Bmatrix} = H_I\delta u_s \text{ (eq. 3.31)}$$

being I a 2x2 identity matrix. Equation 3.27 can be re-written as follows:

$$\delta L = \delta u^T \int_\Omega B_I^T\, cB_I d\Omega u - \delta u_s^T \int_\Omega H_I^T\, b d\Omega - \delta u_s^T \int_{\Gamma_i} H_I^T\, \bar{t} d\Gamma_t = 0 \qquad \text{(eq. 3.32)}$$

The equation system can be presented in the matrix form: $Ku = f$. Being K the stiffness matrix (first term of eq. 3.32), u the displacement field vector and $f = f_b + f_t$ the vector of applied forces (f_b is the second term of eq. 3.32 and f_t is the third term of eq. 3.32). Since the RPI shape function possesses the delta Kronecker property, the essential boundary conditions can be directly applied in the stiffness matrix. In order to determine the stress field, it is necessary to determine: the displacement field by solving the linear equation system $K^{-1}f = u$, the strain in an interest point, $x_I \in \Omega$, which can be obtained using $\varepsilon(x_I) = Lu(x_I)$, and lastly, considering the Hooke Law, to solve the equation 3.33.

$$\sigma(x_I) = c(x_I)\varepsilon(x_I) \qquad \text{(eq. 3.33)}$$

Afterwards, the strain energy density (SED) field for the considered load case is determined using stress field and the strain field. The SED for an interest point x_I is obtained through equation 3.34

$$U(x_I) = \frac{1}{2}\int_{\Omega_I} \sigma(x_I)^T \varepsilon(x_I)\, d\Omega_I \qquad \text{(eq. 3.34)}$$

Additionally, it is possible to obtain the three principal stresses $\sigma(x_I)$, for each interest point x_I, $\det(\Lambda(x_I) - \sigma(x_I)_i I) = 0$, and the three principal directions $n(x_I)_i$: $(\Lambda(x_I) - \sigma(x_I)_i I)n(x_I)_i = 0$, being $\Lambda(x_I)$ the Cauchy stress tensor obtained for the interest point and I a 2x2 identity matrix. Using the three principal stresses $\sigma(x_I)_i$ and the following expression (eq. 3.35)

$$\bar{\sigma}(x_I) = \sqrt{\frac{1}{2}((\sigma(x_I)_1 - \sigma(x_I)_2)^2 + (\sigma(x_I)_2 - \sigma(x_I)_3)^2 + (\sigma(x_I)_3 - \sigma(x_I)_1)^2)} \qquad \text{(eq. 3.35)}$$

The Von Mises effective stress of the interest point x_I is obtained.

Chapter 4

FEMAS

This chapter contains a brief introduction to the software used throughout this work and the standard parameters used in both meshless methods, RPIM and NNRPIM.

4.1 FEMAS

Developed at FEUP and implemented in the commercial software Matlab, FEMAS, is a meshless computational framework that uses the formulation presented in Chapter 2. This program possesses a graphical user interface (GUI), allowing to build the numerical model and analyse it using several numerical discretization techniques. In Figure 4.1 is an image from the program here described.

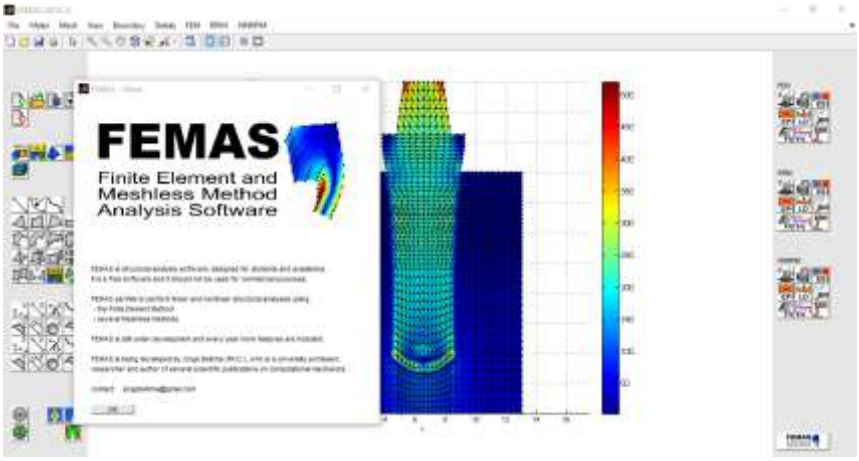

Figure 4.1 FEMAS initial presentation

For comparison purposes, FEMAS can perform numerical analysis using the RPIM, NNRPIM and FEM and can, currently, execute the following analyses:

- Static linear-elastic
- Elasto-plastic
- Crack opening path
- Bone tissue remodelling
- Free vibration
- Buckling
- Fluid Flow (low velocities)

Using this software is possible to work in both 2D and 3D problems. So, the software allows to build autonomously the 2D or 3D numerical model, in which the user controls the nodal discretization, the material disposition and the location of both essential an natural boundary conditions. All these tasks can be executed in the program without usage of any external CAD software. Nevertheless, meshless generated in other CAD programs can also be imported and used in FEMAS. Besides this, the computational framework uses the classical three-dimensional deformation theory (when talking about 3D problems) and the plane stress and plane strain two-dimensional deformation theory (for 2D problems) and also allows the use of both isotropic and anisotropic materials, which the user can choose. The workflow of the elastic-static analysis performed by FEMAS is constituted by three steps, the pre-process, the process and the post-process.

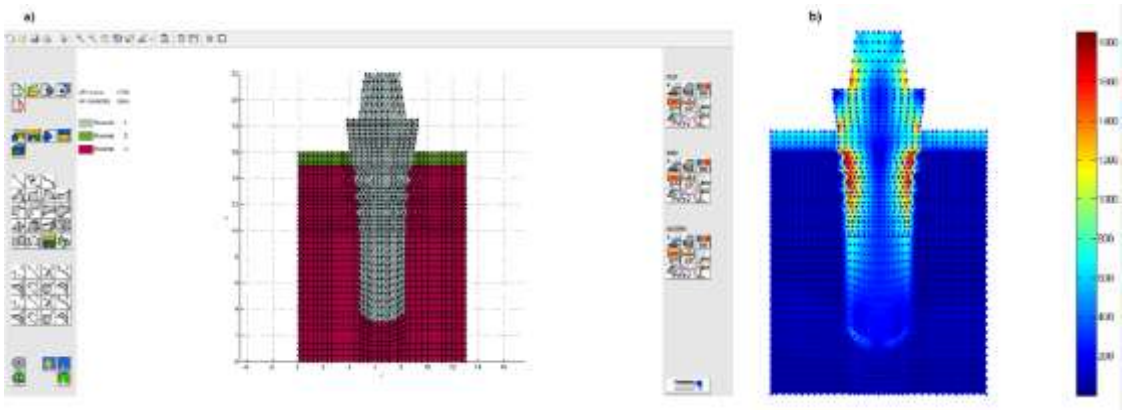

Figure 4.2 a.2D Model of a dental implant built in FEMAS **b.**Stress field of dental implant obtained in FEMAS

Moreover, FEMAS allows to present the displacement, stress and strain fields along with the solid domain using both figures and arrays, which permits further data analyses. In Figure 4.2, it is presented a model built in FEMAS and also a stress field obtained with an analysis in FEMAS.

The following parameters were also used in all RPIM and NNRPIM analysis throughout this work, as recommended by the literature.[3]

Table 4.1 RPIM Parameters

RPIM	
2D	**3D**
Nodes in the influence-domain: **16**	Nodes in the influence-domain: **70**
c = **0.0001**	c = **0.0001**
P = **0.9999**	P = **0.9999**
Polynomial Basis: **Constant**	Polynomial Basis: **Constant**
Integration Points: **1 per triangle**	Integration Points: **1 per triangle**

Table 4.2 NNRPIM Parameters

NNRPIM	
2D	**3D**
c = **0.0001**	c = **0.0001**
P = **0.9999**	P = **0.9999**
Influence-cell: **2nd Order**	Influence-cell: **2nd Order**
Polynomial Basis: **Constant**	Polynomial Basis: **Constant**
Integration Points: **1 per sub-cell**	Integration Points: **1 per sub-cell**

Chapter 5

Dental Implants

At least half of the population from Switzerland and UK have some kind of dental restoration by the year of 1993. In fact, the frequency of removable dental prosthesis (RDPs) among adults varied between 13 and 29%, while the frequency of fixed dental prosthesis (FDP) was the highest in Sweden (45%) and Switzerland (34%).[1]

According to Zitzmann et al[1], the proportion of adults using dental restorations is strongly linked with the age, in which, older patients are the ones where the use of this ones is higher. As well, sociodemographic and economic factors have high influence in the usage of dental restorations, since people living in rural areas, with limited access to education, lower social levels and lower incomes have presented a higher prevalence of dental prosthesis than people living in more centre and urbanized areas, with higher education and social levels. It is assumed that this difference is related to an easy access to dental services by the latter ones.[1]

Dental Implant Treatments offers a solution that may generate more satisfactory outcomes for patients who are not able to adapt to conventional dentures or who have already compromised local host bone. The reported 10-year survival rate is approximately 90%, making it a fairly predictable modality of treatment.[25]

Since there is a high impact on society from the lack of teeth, as it was possible to observe from the data shown previously, it is important to address some time on this topic and observe what happens to both implant and bone when a FDP is made, and an implant is placed in the mouth.

5.1. Types of Implants

Dental prosthesis can be from two types, either removable or fixed and are termed removable dental prosthesis (RDPs) and fixed dental prosthesis (FDPs), respectively. In this work it will be mainly studied the latter ones.

Fixed restorations can be sustained, by its term, for dental implants or not. Fixed restorations can also be subdivided into two main types, crowns and fixed dental prosthesis, also called bridges. However, single crowns are not considered a subdivision, since, by definition, fixed prosthesis are replacing one or more teeth and are associated with alveolar structures. Fixed prosthesis are often applied in cases where the soft tissue is fragile and there is gag reflex from the point of view from the patient.[1]

The number of patients using fixed dental prosthesis instead of RDPs have been increasing, due to a recent widespread availability of osseointegrated dental implants, yet, the price of this implants is, sometimes, still a limiting factor.

Due to the preservation of the structure of adjacent teeth and better comfort, aesthetic outcome, functions and stability, osseointegrated dental implants are, most of the time, preferable to conventional dentures.[25]

5.2. Implants Description

The dental implant was designed to be placed in the jawbone and it is used to replace a missing tooth. Its localization allows the creation of a strong and solid foundation for replacement teeth, by merging with the existent natural bone. There are three main elements in the composition of a dental implant, which are the crown, the abutment and the dental implant itself, seen from the exterior to the interior of it. As it is possible to observe from Fig. 5.1, the crown is the most exterior part of the implant and it is the part which is actually visible. It is a replacement tooth and it is custom made, in order to match the natural teeth and look as similar as the original one. The second component is the abutment, which is a connector placed between the crown and the dental implant. It is important because it will maintain the implant solid. Finally, the last component, which is the dental implant itself, serves as substitute for the tooth root and it has a cylindrical shape, slightly tapered with a rough surface.[26]

Figure 5.1 Constitution of an Implant

The implant's surface has to be rough enough towards an easier attachment and stability, and simultaneously, minimizing bone loss associated with site preparation, and slightly minimizing implant volume. In other words, it is supposed to improve the anchoring capacity with bone maintenance, no loss in bone contact area, and no reduction in mechanical strength of the implant. Implants with roughened surfaces have been recommended for single-stage treatment procedures in aesthetic zone and have been proven successful. According to several authors, bone healing and apposition adjacent to dental implants have improved because of the characteristics of surfaces such as the ones here described.[27]

Improvements in implants surface, may improve the prospects of implant survival and reduce the probability of implant failure, for any given healing period.

Many all-ceramic systems have been proposed in the search for the ultimate aesthetic restorative material. In pursuance of an improvement aesthetical outcome of FPD restorations, dental researchers are nowadays directed towards metal-free prosthetic restorations, giving more consistence look of soft tissue in contact with FPD, being these influenced by two factors: mucosal thickness and typology of restorative material. Instead of porcelain fused to metal restorations and restorations, which are more commonly used, it can be adopted metal-free restorations. This permits to preserve soft tissue colour more similar to the natural one. Ceramics such as spinel, alumina and ceramic reinforced with lithium disilicate, have been proposed for the construction of metal free restorations having precise indications for fixed partial dentures.[28]

5.3. Used Materials for Implants

The biomechanical integrity of implants comprises the mechanical behaviour of implant materials, surface/induced bone micromechanics, and adaptive bone remodelling. Once implants are placed with intimate apposition of bone at the surgical site, there is an immediate response at the interface which involves adsorption of tissue fluid and cell binding proteins.[29,30] The existent critical gap between host bone and the implant surface is likely filled by newly formed bone and non-collagenous protein-rich cement line.[31–34]

Many all-ceramic systems have been proposed in the search for the ultimate aesthetic restorative material. In order to improve this outcome of FPD restorations, dental research is nowadays directed towards metal-free prosthetic restorations, which (as already mentioned) allow to preserve soft tissue colour more similar to the natural one than porcelain fused to metal restorations. The natural look of soft tissue in contact with fixed partial dentures is influenced by two factors: musical thickness and typology of restorative material.[28]

Many ceramic, such as spinel, alumina and ceramic reinforced with lithium disilicate have been proposed for the construction of metal-free restorations, however, this reinforced ceramics can only be used to replace anterior teeth with single crown restorations or maximum with three units FPDs. On the other hand, ZrO_2 restorations have a wider application field and

can also be used on molars. Other ceramic technologies only allow the construction of structures that are resistant to chewing stresses on an anterior teeth.[28,35]

5.3.1. Zirconia

The height of the abutment is fundamental to obtain ZrO_2 frameworks with correct shape and dimension to ensure mechanical resistance of restoration.

Zirconia is a crystalline dioxide of zirconium having analogous mechanical properties to those of metals and its colour is very similar to tooth colour. A volumetric change in the crystal is due to a force on the zirconia surface caused by a transition between the different crystalline reticulations and it is where the stress is applied. This crystalline modification is followed by an expansion that seals the crack. Zirconia Dioxide (ZrO_2) can be stabilized with Yttrium Oxide (Y_2O_3) which will guarantee better mechanical properties than other combinations. Although its sintering is much more difficult, this is the principal kind of zirconia considered for current medical applications.[28]

The first use of zirconia oxide for medical purposes was in an orthopaedic application, in which the research was focused on the mechanical behaviour of zirconia, as well as, on its wear and the integration with bone and muscle. Zirconium oxide creates less flogistic reaction in tissue than other restorative material, such as titanium. Inflammatory infiltrate, micro-vessel density, and vascular endothelial growth factor expression were found to be higher around the titanium caps than around the zirconium oxide ones.[28]

Regarding the zirconia mechanical properties, they are similar to those of stainless steel, in which the resistance to traction can be as high as 900-1200 MPa and its compression resistance is about 2000 MPa. Cyclical stresses are also well tolerated by this kind of material. According to Cales, it was necessary around 50 billion cycles to break the samples, when applying an intermittent force of 28 kN to zirconia substrates. Despite this, with a force in excess of 90 kN, the same author found that structure failure of the samples occurred after just 15 cycles. It is also known that surface treatments can modify the physical properties of zirconia and the exposure to wetness for an extended period of time can have a detrimental effect on its properties. Tinschert et al. reported a fracture load for ZrO_2 of over 2000 N. Sundh et al. measured fracture loads in the range of 2700-4100 N, and whereas Luthy et al. asserted that zirconia core could fracture under a load of 706 N. However, these results are not directly compatible because the methods of measurement were not standardized between studies. [28,36]

Zirconia restorations have found their indications for FPDs supported by teeth or implants. Due to the mechanical reliability of this material, single tooth restorations and fixed partial dentures with a single pontic element are possible on both anterior and posterior elements. Ageing Zirconia can have detrimental effects on its mechanical properties. Mechanical stresses and wetness exposure are critical to accelerate this process. Nowadays, effects of ageing

zirconium oxide used for oral rehabilitation are not yet well known. Resistance values decrease into clinical acceptable values, although ageing reduce mechanical features of Zirconia. It has not only a colour similar to teeth but it is also opaque, being an advantage for the technician.[28]

Even though many types of zirconia-containing ceramic systems are currently available, only three are used to date in dentistry. These are yttrium cation-doped tetragonal zirconia polycristals (3Y-TZP), magnesium cation-doped partially stabilized zirconia (Mg-PSZ) and zirconia-toughened alumina (ZTA).

The mechanical properties of 3Y-TZP strongly depend on its grain size. While above a critical grain size, this system is less stable and more susceptible to spontaneous transformations induced by stress, whereas smaller grain sizes (< 1μm) are associated with a lower transformation rate. Moreover, below a certain grain size (≈ 0.2μm), the transformation is not possible, leading to reduced fracture toughness. These are well above those of all other available dental ceramics, with a flexural strength in the 800-1000 MPa and a fracture toughness in the 6-8 MPa$\sqrt{m}$ range.[37]

One of the main advantages of zirconia-toughened alumina is that there is a very limited shrinkage having, yet, a greater amount of porosity than that of sintered 3Y-TZP, which was seen previously. The In-Ceram® and Zirconia® processed by slip-casting, both of them commercially available dental products, have a significantly higher flexural strength (630±58 MPa), when compared to the machined material (476±50 MPa) and have no significant difference in fracture toughness. In some of the newly developed ZTA for biomedical applications, excellent mechanical properties are obtained by promoting a fine and uniform dispersion of zirconia grains in an alumina matrix.[37]

Although a considerable amount of research has been dedicated to magnesia partially stabilized zirconia (Mg-PSZ) for possible biomedical applications, this material has not been successful mainly due to the presence of porosity, associated with large grain size (30-60 μm) that can induce wear.[37]

Since this work will mainly focus on the implant materials, it is important to know the Poisson's coefficient, as well as the elasticity modulus (E). For the specific case of zirconia, the coefficient of Poisson (v) is 0.25 and the Young's modulus is 245 GPa. Having in mind that the bone's elastic modulus is presumed to be 10-30 GPa, the zirconia flexural modulus is approximately 16 times higher than that.[38,39]

Moreover, since this is a biomechanical analysis it is important to know the value of the Maximum Compressive Strength of the Zirconia. The literature reports a value of 900MPa for the Maximum Compressive Strength of the Zirconia.[40,41]

5.3.2. Bone

Over a long period of human evolution and adaptation, hard tissues such as bone and teeth have developed desirable mechanical properties along with their own hierarchical structures.

Bone is still functional as a supporting tissue for much harder and stiffer implants, which allows to conclude that intact bone enables remarkable adaptation associated with strain energy dissipation in the human body.[34]

Bone consists of directional structural features across several hierarchical scales, ranging from nanoscale crystals and molecules to the microscopic range.[42,43]A two-phase arrangement of an anisometric bone mineral called hydroxyl apatite, preferentially oriented in a collagen matrix is the foundational unit.[44,45] According to Griffith's[46] theory of brittle fracture, the smaller the individual sample, the higher the strength is, because smaller samples contain less and smaller defects. Having this in mind, nanoscale bone apatite crystals enable a higher strength than bulk sintered apatite block.[34]

Many experimental studies show that the bone mechanical properties depend on the bone composition and on the bone porosity (directly related with the bone density).

At the macrostructure level, bone can be distinguished in two types: cortical (or compact), highly densified bone tissue, and cancellous (or trabecular), which shows a considerably smaller apparent density. Even though types of bone (cortical and trabecular) are most easily well-known by their degree of porosity or density, true differentiation comes from histological evaluation of the tissue's microstructure. And the mechanical behaviour is also different.[3,42,47-52]

In cortical bone the mechanical properties are influenced greatly by the porosity, the mineralisation level and the organization of the solid matrix. In opposition to cortical bone, the mechanical properties of cancellous bone vary significantly.[42]

From the literature it was possible to assemble in Table 5.1 the properties of five cases of different types of bone. Despite all of this five cases have different Young Modulus for both Cortical and Trabecular Bone, all of them have the same Poisson's coefficient: v=0.3. All of this five cases were used in the presented study.

As it was already mentioned in section 5.3.1, it is important for this study to know the value of the Compressive stress of the bone. According to Belinha[3], the bone Maximum Compression Stress for the density used in this study is about 50MPa.[3]

Table 5.1 Mechanical Properties of bone cases

Case	Cortical Bone Young Modulus (MPa)	Trabecular Bone Young Modulus (MPa)	Ref
1	10000	250	53
2	11500	2130	54
3	13400	790	4
4	13700	1000	55
5	14800	1850	56

Chapter 6

Numerical Examples

Throughout the years there have been many works studying the numerical analysis in implants, especially dental implants. Due to the fact that components in a dental implant bone system are extremely complex geometrically, the most common analysis performed has been finite element analysis.[4]

FEM has been used in implant dentistry since 1976 (Weinstein at al.[57]) after Atmaram and Mohamed[58-60] , studied the distribution of stress alongside a single tooth implant. This allowed a better understanding of the effect of elastic parameters and the geometry of the implant, as well as implant length variation and pseudo-periodontal ligament incorporation. Borchers and Reichart[61] and Cook et al.[62] performed a 3D finite element analysis of an implant at different stages of bone interface development and applied the method to porous rooted dental implants, respectively. Meroueh et al.[63] performed the same analysis for an osseointegrated cylindrical implant. Williams et al.[64] carried out an FEA on a cantilevered prostheses on dental implants, and Akpinar et al.[65] used FEA to simulate the combination of a natural tooth and implant.[4]

Towards making the modelling and solving process possible, certain assumptions needed to be done, since the principal difficulty in simulating the mechanical behaviour of dental implants is the modelling of human bone tissue and its response to applied mechanical force. Due to the complexity of the mechanical characterization of bone and its interaction with implant systems, the assumption made include a detailed geometry of the bone and implant to be modelled, material properties, boundary conditions and interface between bone and implant.[4,66,67]

If the goal is to obtain more accurate stress predictions, advanced digital imaging techniques can be applied to model the bone geometry more realistically. Also, the anisotropic and non-homogeneous nature of the material must be considered and the boundary conditions must be carefully treated with the use of computational modelling techniques. Moreover,

modelling of the bone-implant interface should incorporate the actual osseointegration contact area in cortical bone and the detailed trabecular bone contact pattern through the use of contact algorithms in FEM.[4]

More recently, studies considering the FEM model done by Chou et al.[68] analysed a two-dimensional four-node finite element. Furthermore, Lian et al.[69] proposed a FEM model having in consideration a two-dimensional three-node element. In the first of these two works, the implant system was submitted to an occlusal load, F_0 = 100 N applied directly in the crown, inclined 11º in relation to the implant longitudinal axis and it is suggested a second load condition referring an uniform distributed pressure along the outer surface of the cortical bone (500 kPa) which intend to simulate the effect of the mandibular flexure. In this same analysis, the model is constrained in the basis along x and y direction.[3]

Meshless methods have also been applied in this field, becoming more effective and used throughout the years. As shown by Belinha and co-workers, the proposed algorithm for bone remodelling presented by them, combined with the NNRPIM is capable of reproducing trabecular distributions very close to the clinical results and much better predictions when compared with the FEM. Under the implant is possible to observe high-density horizontally oriented regions connecting the cortical layers on the bone periphery and a closer look allows to verify that using a meshless approach is likely to achieve results that resembles much more real trabecular structures when compared with results obtained with FEM.[3,68,69]

6.1. The work

The numerical model analysed in this work was built based on 3D images provided by zirconia implant manufacturer (Ceraroot®, Barcelona, Spain), are presented in Figure 6.1a. From the 3D geometry, two section views were obtained. Since the provided zirconia implant is not perfectly cylindrical, the two section views optimized the minimum and maximum 2D geometries that can be obtained from the 3D model, Figure 6.1b and Figure 6.1c.

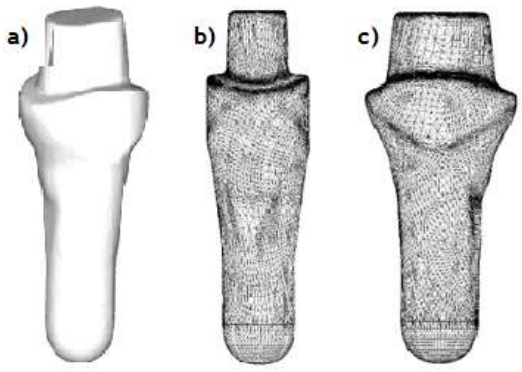

Figure 6.1 a)3D model of the zirconia implant. **b)**2D view showing the minimum geometric dimensions. **c)**2D view showing the maximum geometric dimensions.

In order to study the mechanical behaviour of the zirconia implant and the corresponding bone response, the implant was inserted in a cubic block of bone, as Figure 6.2a shows. Then, 2D section cuts were performed, respecting the optimized geometries previously presented, Figure 6.2b and 6.2c. In the end, 2D dental implant system, respecting dimensions suggested in other research works[69], were obtained.

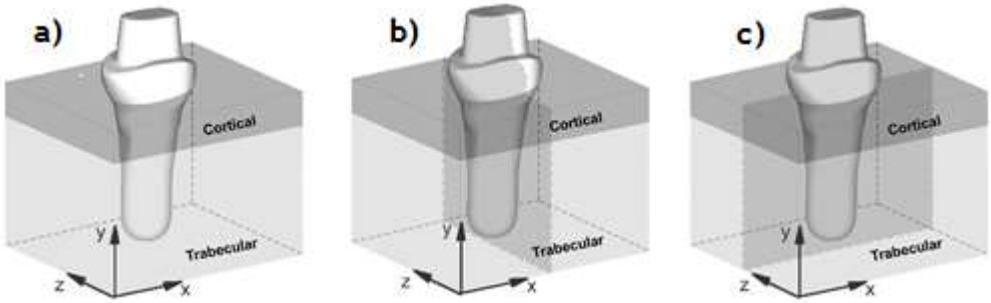

Figure 6.2 a)3D model of the zirconia implant inserted in the bone block. **b)**2D section cut capturing the minimum geometric dimensions. **c)**2D section cut capturing the maximum geometric dimensions.

There were created two models, one which was called 'Model 1' having 2.6mm in x direction and another which was called 'Model 2' being slightly thicker, having 3.5mm, as it is possible to observe in Figure 6.3a and Figure 6.3b, respectively. Both view had 12mm length.

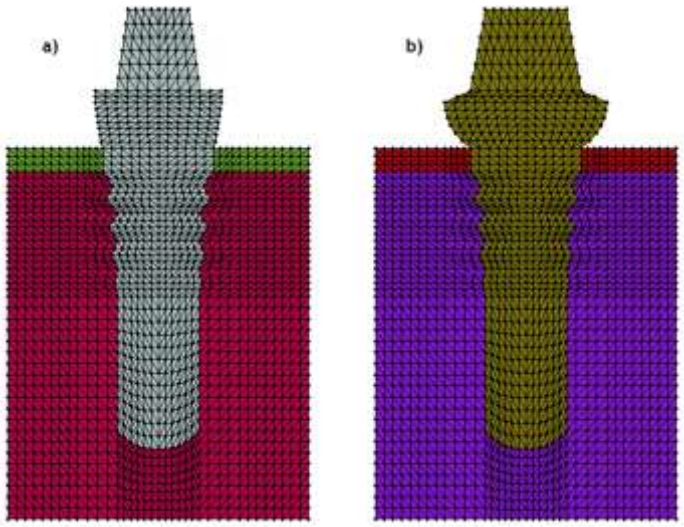

Figure 6.3 a. Model 1**. b.**Model 2

As it is possible to observe in Figure 6.3, there are three diverse materials, in each model: the zirconia, the cortical bone and the trabecular bone. The first one is the material from which the implant is made (grey in Model 1 and green in Model 2). The second one is a cortical bone layer (green in Model 1 and red in Model 2), and the latter one is a trabecular bone layer (Bordeaux in Model 1 and purple in Model 2). The mechanical properties of the distinct

materials presented were shown previously in this work, in sections 5.3.1 and 5.3.2, respectively. In this work, there were used five different types of bone, where the Young modulus of both Cortical and Trabecular bone varied, according to Table 5.1.[70]

One of the main purposes of the present study is to compare the results obtained with the proposed numerical approach with other algorithms, such as the finite element method. Due to the fact that there were two different models, which had different meshes, the number of nodes in each one was also different. The 'Model 1' mesh had 1725 nodes and 'Model 2' mesh had 1758 nodes.

After each mesh was constructed, the essential and natural boundary conditions were applied as suggested in the work of Chou et al.[68] with some adjustments. The load applied, as in the mentioned work, was 100 N, and were tested all inclinations from 90º to 10º with intervals of 10º, instead just the 11º angle suggested in the literature[68]. Also, the uniform distributed pressure along the outer surface was not applied. The movement of the model was blocked in x direction in the lateral faces and along y in the basis, as shown in Figure 6.4a, constituting the essential boundary conditions. In Figure 6.4b, is an example of a model with an applied load at an inclination of 70º.

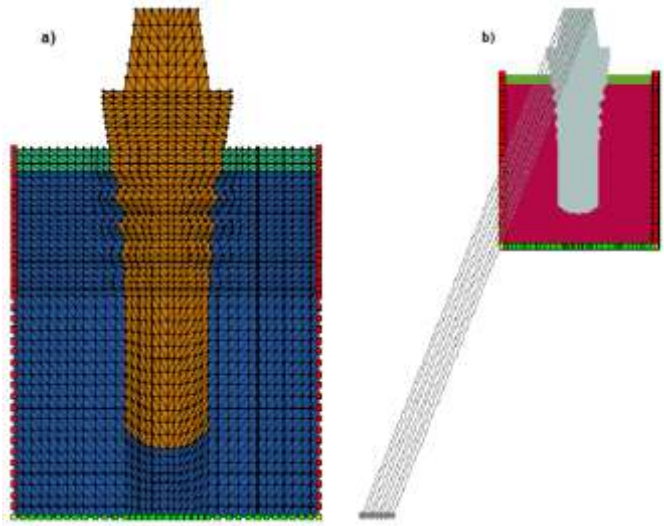

Figure 6.4 a. Model with essential boundary conditions **b.**Model with essential boundary conditions and applied load at 70º

Once all the parameters are settled, it is possible to perform a static linear-elastic analysis. With this analysis it is possible to obtain, for instance, the Von Mises stress map of each model. The maps for all the models are presented in appendix 1 FigureA.1, FigureA.2, FigureA.3, FigureA.4, FigureA.5, FigureA.6, FigureA.7, FigureA.8, FigureA.9 and FigureA.10. Each figure represent a stress map for one model and one type of bone that is why there are 10 different. In each one, the first line corresponds to FEM analysis, the second line to RPIM analysis and the third line to NNRPIM analysis. Besides, each column represents an angle from 10º to 90º from

left to right, respectively. In Figure 6.5 it is represented an example of this tension maps from 'Model 1', type of bone 1, at an angle of 10º and that was analysed with FEM. As it is possible to observe, the areas where the stress is higher are inside the implant, where the colour is red and correspond to higher values of stress. The dark blue is the place where the stress is lower and corresponds essentially to the trabecular bone.

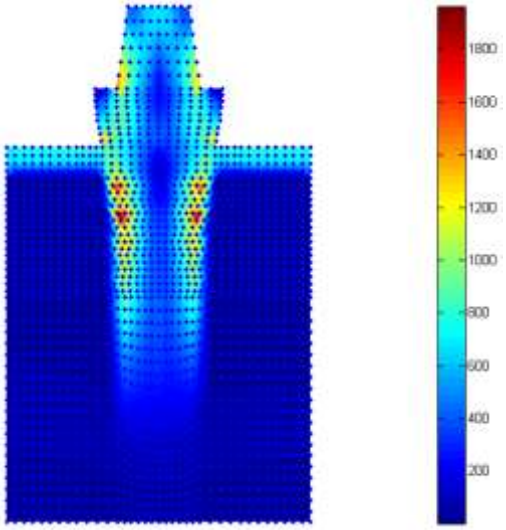

Figure 6.5 Stress map from type of bone 1, 'Model 1', angle 10º, analysed with FEM

The interface between the implant and the bone is the zone with greater interest for this study. In order to study the stress created by the applied load in this area, after each stress map was obtained, it was chosen a line of points on the implant side and a line of points on the bone side, as Figure 6.6 shows. The line was obtained based on Matlab script created by the author, through reading the Excel files that were extracted from each of the results originated by FEMAS.

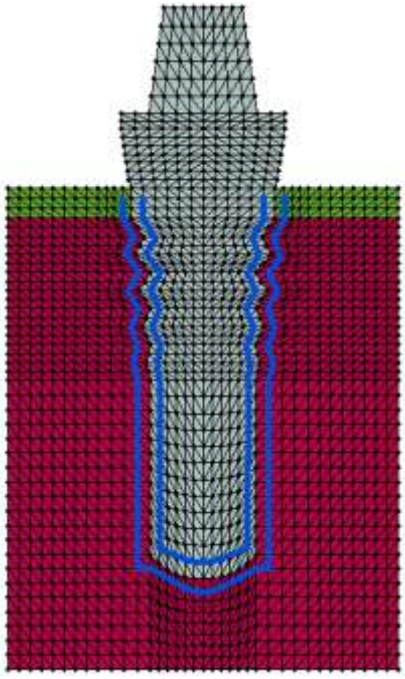

Figure 6.6 Model of a dental implant with the two lines selected

The main purpose for this analysis is comparing the three methods mentioned before, FEM, RPIM and NNRPIM, for each model, on the perspective of both bone and implant, for each type of bone and for all angles, pointed out previously. Having this comparison in mind, for each case, it was built a graph which are presented in appendix 2. The graphics allow to analyse how the stress vary along the selected line. In Figure 6.7a and 6.7b are examples of these graphs. The first one (Figure 6.7a) is in respect of bone side and the other one (Figure 6.7b) is in respect of implant side.

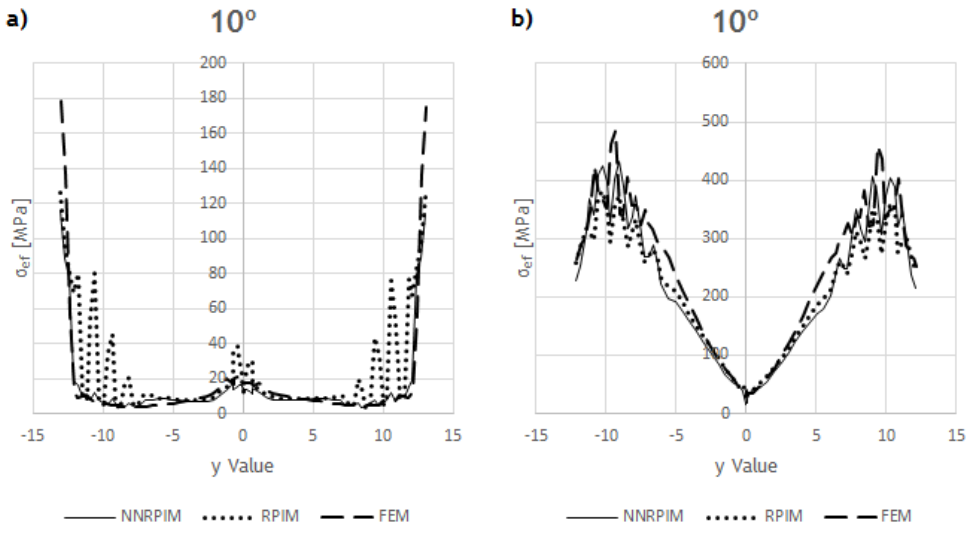

Figure 6.7 a. Stress distribution from bone side, from 'Model 1', for an angle of 10º **b.**Stress distribution from implant side, from 'Model 1', for an angle of 10º

Although there weren't negative values on the initial model, in interest of a better visualization of the results, it was performed a normalization of the results. Regarding this topic, the value corresponding to the lowest value of y from the line obtained previously (points 5 and 14 from Figure 6.8), corresponds to zero in the graphics, and the other values became symmetric. Thus, the values from the left side of the model (x value lower than point 5 for bone side and 14 for implant side) are negative in the graphics and values from the right side of the model (x value higher than point 5 for bone side and 14 for implant side) are positive in the graphics.

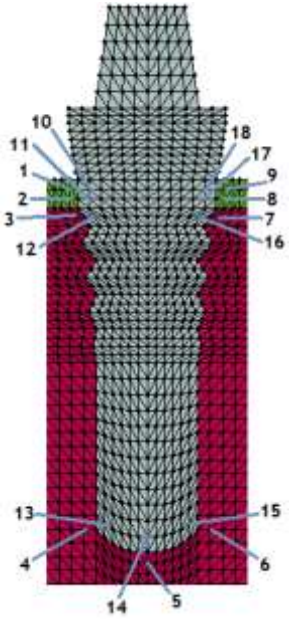

Figure 6.8 Points of interest in the model of the dental implant

Since the produced line-graphics only allow to analyse variation of data, 18 points were chosen to analyse their individual values and are indicated in Figure 6.4. Points 1 to 9, inclusive, regards to the bone side, where points 1, 2, 8 and 9 corresponds to cortical bone and the others to trabecular bone. Points 10 to 18, inclusive regards the implant. Their individual values of stress were obtained and gathered in the Tables from appendix 3, where M1 corresponds to 'Model 1' and M2 resembles to 'Model 2'. Each one of this tables has a dashed line separating the points that corresponds to the bone side and the implant side.

Afterwards, in order to better understand how stress varies in function of the angle for each method, FEM, RPIM and NNRPIM, it was constructed a graph, having this relation as a base, for each point of Figure 6.8. An example is presented below in Figure 6.9, where it is presented discrete stress values for type of bone 4, 'Model 1', and seen from implant perspective, more specially, point 16 (Figure 6.8). The values correspondent to x are the values of the tested angles, meaning, 10º, 20º, 30º, 40º, 50º, 60º, 70º, 80º and 90º, and the values correspondent to the y are the effective stress values. In this graphic are represented all the three methods tested

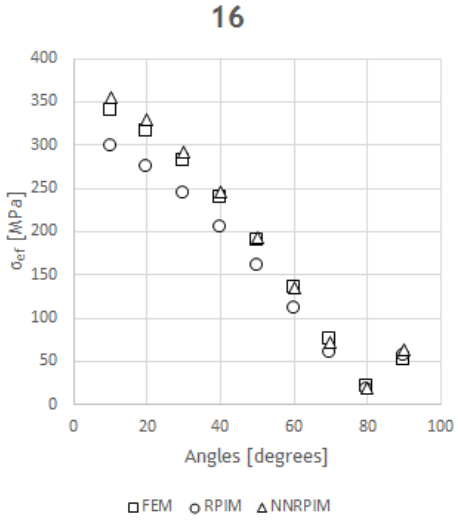

Figure 6.9 Discrete Stress Values for type of bone 4, 'Model 1' and from implant side (point 16)

All the obtained graphs are in appendix 4. The angles represented in the graphs are the angles mentioned before, from 10º to 90º with intervals of 10º.

Through the observation of the results obtained for each of the presented cases, it is possible to notice that even though the results obtained with the three methods tested (FEM, RPIM and NNRPIM) lead to quite similar stress distributions, there are some differences intrinsic to each method.

Firstly, looking to the stress maps from appendix 1, it is possible to observe that there are higher stress values from the left side of the implant, probably due to the fact that the load is applied down with inclination to the left. Despite the differences of the meshes from 'Model 1' and 'Model 2', the results obtained in both cases were similar between each other, for all types of bones, except for the type of bone 1, for higher angles (80º and 90º). In this case, the results obtained with FEM were slightly different from the ones obtained with meshless methods, where FEM had higher stress values.

Looking, now, for the graphs created having as base the selected line (appendix 2), in order to study the interface implant-bone, it is possible to see that NNRPIM and FEM have quite similar results, but, RPIM has constantly results higher than the other two referred methods, even though this results are more dissimilar for higher values of the angles. From the graphs is also possible to notice that FEM has higher values of stress than meshless methods for the points in which the absolute value of y is higher. Furthermore, the values of stress from the bone side are, generally, lower than the same ones from the side of the implant. From the bone perspective, an increasing value of the angle results in an increasing value of stress of the y values near zero. The same happens for the implant perspective, even though for lower values

of angles, in this case, the stress values for higher absolute values of y are higher than from bone side.

Regarding the results from the tables from appendix 3, although very similar, the values from 'Model 2' are all higher than the ones obtained for 'Model 1', and as it was expected, from the previous analysis, the stress values from the implant are higher than the ones from the bone, because Zirconia has a higher Young's Modulus than the bone. Regarding the two different types of bones, it is possible to observe that points 1, 2, 8 and 9 have higher values of stress than points 3, 4, 5, 6 and 7, even though all of them correspond to bone. This occurs because the first four here mentioned correspond to cortical bone and the others correspond to trabecular bone and the latter one has lower values of Young's Modulus in all five bone types than the first one.

Lastly, analysing the results obtained from the graphics which relate the stress with the angle, it is possible to say that for all cases, the best results are in points 10, 11, 12, 16, 17 and 18 and the poorest results are points, 3 and 7. The latter ones must be due to the fact that are in the interface with both the implant and with cortical bone, leading to poorer results.

Once analysed all the results through the graphs, it is important to see the results from the perspective of both bone and zirconia implant. Considering the worst cases studied from the perspective of Zirconia implant, which occurred for point 12 (Figure 6.6), for all types of bone except type 2, for angles 10º and 20º, for methods FEM and NNRPIM, for 'Model 2', the values varied around 600 MPa. Since the Maximum Compressive Strength of the Zirconia is 900MPa, the obtained value was lower, even for the minimum value of the interval cited in the literature, becoming, the value acquired in this study, 600 MPa below from the mentioned value.

Regarding the bone perspective, the value of Maximum Compression Stress (50MPa) was higher only from points 3 to 7 and the worst results were from points 1 and 9 (Figure 6.6).

Even though points 3 to 7 (Figure 6.6) were the ones which fits the most the value presented in literature, a considerable number of values are above 50MPa, especially in 'Model 2', because, as it was already referred, it has higher values than 'Model 1'. The results presented in this study don't have a good agreement with the value presented in Belinha[3], probably due to the fact that the value extracted from the literature was based on the density of the bone, and the Elastic Modulus used in Belinha's work was approximately 10 times lower than the ones used in this work. As the latter parameter has influence in the results, perhaps, if it was used Elastic Modulus suggested in Belinha, the results would be better.

Chapter 7

Conclusions and Future Work

This study is a comparative study between the Finite Element Method (FEM), the Radial Point Interpolation Method (RPIM) and the Natural Neighbour Radial Point Interpolation Method (NNRPIM) on the analysis of dental implants.

From this work, the main conclusions that can be drawn were:

- ✓ Meshless methods converge much faster than FEM. When compared with FEM, the convergence rate is similar.
- ✓ Considering the same number of nodes, even though meshless methods require a higher computational time, the same solution can be achieved using fewer nodes than FEM, which means that the same accuracy in results can be obtained through a smaller mesh
- ✓ The stress values obtained for Zirconia are very distant from the maximum compressive strength of Zirconia (900MPa).
- ✓ The difference of stress between FEM and the meshless methods is due to the fact that the influence-domain from meshless methods is bigger than the influence-domain from FEM (a single element). This leads to softer mechanical properties on the integration point, where the stress value is read.
- ✓ This work shows that meshless methods are an alternative numerical tool to analyse dental implants structures using 2D formulations.
- ✓ Form this work it is possible to say that Zirconia implants are suitable, because the Maximum Compressive Strength is never reached, even though bone has stress values near the value of Maximum Compression.

In the beginning, this work had three main goals, being the first one, perform an elasto-static analysis of a dental implant, applying a concentrated load, using three numerical

method: FEM, RPIM and NNRPIM. The second one, was to compare the performance of all three methods, especially FEM, against the two meshless methods. And the third one was to understand the mechanical behaviour of zirconia implants and the bone tissue response, in the presence of such implants. Regarding this purposes, it is possible to observe that all of them were fulfilled, which can be observed from the analysis of the results, which were obtained by an elasto-static analysis performed with FEMAS, with a concentrated load of 100N in each case. The results for FEM, RPIM and NNRPIM were obtained, which allowed a performance analysis between all of them. In order to analyse the mechanical behaviour of zirconia implants and the bone response to them, graphs were done that corroborate this behaviour, and which is analysed in section 6.1.

In the future, it would be interesting to continue this work, by testing different approaches to the same problem, for instance:

- ✓ Test with implants with the mechanical properties of titanium and PEEK.
- ✓ Perform the same analysis in a 3D model of a dental implant.
- ✓ Perform an elasto-plastic analysis.
- ✓ Analyse the bone remodelling created by dental implants.
- ✓ Compare the results obtained numerically with similar ones obtained by experimental testing

References

1. Zitzmann NU. What is the prevalence of various types of prosthetic dental restorations in Europe ? 2007:20-33. doi:10.1111/j.1600-0501.2007.01435.x.
2. Salinas TJ, Block MS, Sadan A. Fixed Partial Denture or Single-Tooth Implant Restoration ? Statistical Considerations for Sequencing. 2004:2-16. doi:10.1016/j.joms.2004.06.001.
3. Belinha J. *Meshless Methods in Biomechanics: Bone Tissue Remodelling Analysis*.; 2012. doi:10.1007/978-94-007-4174-4.
4. Geng JP, Tan KB, Liu GR. Application of finite element analysis in implant dentistry: a review of the literature. *J Prosthet Dent*. 2001;85(6):585-598. doi:10.1067/mpr.2001.115251.
5. Dinis LMJS, Natal Jorge RM, Belinha J. Analysis of plates and laminates using the natural neighbour radial point interpolation method. *Eng Anal Bound Elem*. 2008;32(3):267-279. doi:10.1016/j.enganabound.2007.08.006.
6. Nayroles B, Touzot G, Villon P. Computational Mechanics Generalizing the finite element method : Diffuse approximation and diffuse elements. 1992:307-318.
7. Phu V, Rabczuk T, Duflot M. Meshless methods : A review and computer implementation aspects. 2008;79:763-813. doi:10.1016/j.matcom.2008.01.003.
8. Belinha J, Dinis LMJS, Jorge RMN. The Meshless Methods in the Bone Tissue Remodelling Analysis. *Procedia Eng*. 2015;110:51-58. doi:10.1016/j.proeng.2015.07.009.
9. Doblaré M, Cueto E, Calvo B, Martínez M a., Garcia JM, Cegoñino J. On the employ of meshless methods in biomechanics. *Comput Methods Appl Mech Eng*. 2005;194(6-8):801-821. doi:10.1016/j.cma.2004.06.031.
10. LIU GR, GU YT. A point interpolation method for two dimensional solids. *Int J Numer Methods Eng*. 2001;50(4):937-951. doi:10.1002/1097-0207(20010210)50.
11. Wang JG, Liu GR. A point interpolation meshless method based on radial basis functions. *Int J Numer Methods Eng*. 2002;54(11):1623-1648. doi:10.1002/nme.489.
12. Sibson R. A brief description of natural neighbour interpolation. *Interpret Multivar data*. 1981. https://scholar.google.pt/scholar?q=A+brief+description+of+natural+neighbor+interpolation&btnG=&hl=pt-PT&as_sdt=0%2C5#0. Accessed February 1, 2016.
13. Voronoi G. Nouvelles applications des paramètres continus à la théorie des formes quadratiques. Deuxième mémoire. Recherches sur les paralléllòèdres primitifs. *J für die reine und Angew Math*. 134:198-287. https://eudml.org/doc/149291. Accessed February 1, 2016.
14. Delaunay B. Sur la sphere vide. *Izv Akad Nauk SSSR, Otd Mat i …*. 1934. http://galiulin.narod.ru/delaunay_.pdf. Accessed February 1, 2016.
15. Belytschko T, Lu YY, Gu L. Element-free Galerkin methods. *Int J Numer Methods Eng*.

1994;37(2):229-256. http://www.scopus.com/inward/record.url?eid=2-s2.0-0028259955&partnerID=tZOtx3y1.
16. Wing Kam Liu, Sukky Jun, Yi Fei Zhang. Reproducing kernel particle methods. *Int J Numer Methods Fluids*. 1995;20(8-9):1081-1106. http://www.scopus.com/inward/record.url?eid=2-s2.0-0029102512&partnerID=tZOtx3y1.
17. Atluri SN, Zhu T. A new Meshless Local Petrov-Galerkin (MLPG) approach in computational mechanics. *Comput Mech*. 1998;22(2):117-127. http://www.scopus.com/inward/record.url?eid=2-s2.0-0032136132&partnerID=tZOtx3y1.
18. Wang JG, Liu GR. On the optimal shape parameters of radial basis functions used for 2-D meshless methods. *Comput Methods Appl Mech Eng*. 2002;191(23-24):2611-2630. doi:10.1016/S0045-7825(01)00419-4.
19. Zienkiewicz O, Taylor R. The finite element method. 1977. http://civil.dept.shef.ac.uk/current/module/CIV4135.pdf. Accessed June 3, 2016.
20. Bathe K-J. Finite element procedures. 1996. https://dialnet.unirioja.es/servlet/libro?codigo=370662. Accessed June 3, 2016.
21. Sibson R. A vector identity for the Dirichlet tessellation. *Math Proc Cambridge Philos Soc*. 2008;87(01):151. doi:10.1017/S0305004100056589.
22. Dinis LMJS, Natal Jorge RM, Belinha J. Analysis of 3D solids using the natural neighbour radial point interpolation method. *Comput Methods Appl Mech Eng*. 2007;196(13-16):2009-2028. doi:10.1016/j.cma.2006.11.002.
23. Liu GR, Quek SS, Liu GR, Quek SS. 2 – Introduction to mechanics for solids and structures. In: *Finite Element Method*. ; 2003:12-34. doi:10.1016/B978-075065866-9/50003-7.
24. Liu GR, Quek SS, Liu GR, Quek SS. 3 – Fundamentals for finite element method. In: *Finite Element Method*. ; 2003:35-66. doi:10.1016/B978-075065866-9/50004-9.
25. Wang G, Gao X, Lo ECM. Public perceptions of dental implants: a qualitative study. *J Dent*. 2015;43(7):798-805. doi:10.1016/j.jdent.2015.04.012.
26. What are Dental Implants, Abutments and Crowns? | AAID | American Academy of Implant Dentistry. http://www.aaid-implant.org/about-dental-implants/what-are-dental-implants/. Accessed February 1, 2016.
27. Morton D, Martin WC, Ruskin JD. Single-Stage Straumann Dental Implants in the Aesthetic Zone : Considerations and. 2004:57-66. doi:10.1016/j.joms.2004.06.043.
28. Manicone PF, Iommetti PR, Raffaelli L. An overview of zirconia ceramics : Basic properties and clinical applications. 2007;35:819-826. doi:10.1016/j.jdent.2007.07.008.
29. Puleo DA, Nanci A. Understanding and controlling the bone-implant interface. *Biomaterials*. 1999;20(23-24):2311-2321. doi:10.1016/S0142-9612(99)00160-X.
30. Shibata Y, Hosaka M, Kawai H, Miyazaki T. Glow Discharge Plasma Treatment of Titanium Plates Enhances Adhesion of Osteoblast-like Cells to the Plates Through the Integrin-Mediated Mechanism. *Int J Oral Maxillofac Implant*. 2002;17(6):771-777. http://www.scopus.com/inward/record.url?eid=2-s2.0-0036836152&partnerID=tZOtx3y1.
31. Ayukawa Y, Takeshita F, Inoue T, et al. An immunoelectron microscopic localization of noncollagenous bone proteins (osteocalcin and osteopontin) at the bone-titanium interface of rat tibiae. *J Biomed Mater Res*. 1998;41(1):111-119. http://www.ncbi.nlm.nih.gov/pubmed/9641631. Accessed February 1, 2016.
32. Linder L. High-resolution microscopy of the implant-tissue interface. *Acta Orthop*. 1985;56(3):269-272. doi:10.3109/17453678508993011.
33. Murai K, Takeshita F, Ayukawa Y, Kiyoshima T, Suetsugu T, Tanaka T. Light and electron microscopic studies of bone-titanium interface in the tibiae of young and mature rats. *J Biomed Mater Res*. 1996;30(4):523-533. doi:10.1002/(SICI)1097-4636(199604)30:4<523::AID-JBM11>3.0.CO;2-I.
34. Shibata Y, Tanimoto Y, Maruyama N, Nagakura M. A review of improved fixation methods for dental implants. Part II: Biomechanical integrity at bone–implant interface. *J Prosthodont Res*. 2015;59(2):84-95. doi:10.1016/j.jpor.2015.01.003.
35. Raigrodski AJ. Concepts of Design for Contemporary Anterior All-Ceramic Restorations.

2013;28(4):46-59.
36. Cales B, Stefani Y. Mechanical Properties and Surface Analysis of Retrieved Zirconia Hip Joint Heads after an Implantation Time of Two to Three Years. *J Mater Sci*. 1994;5(6-7):376-380. doi:10.1007/BF00058967.
37. Denry I, Kelly JR. State of the art of zirconia for dental applications. 2007;4:299-307. doi:10.1016/j.dental.2007.05.007.
38. Della Bona A, Donassollo TA, Demarco FF, Barrett AA, Mecholsky JJ. Characterization and surface treatment effects on topography of a glass-infiltrated alumina/zirconia-reinforced ceramic. *Dent Mater*. 2007;23(6):769-775. doi:10.1016/j.dental.2006.06.043.
39. Ryan G, Pandit A, Apatsidis DP. Fabrication methods of porous metals for use in orthopaedic applications. *Biomaterials*. 2006;27(13):2651-2670. doi:10.1016/j.biomaterials.2005.12.002.
40. Vs FZ, Units S. Full Zirconia Vs. e.max Single Units. 2012;(August):48-50.
41. Zirconia - ZrO2, Zirconium Dioxide Properties. http://www.azom.com/properties.aspx?ArticleID=133.
42. Rho JY, Kuhn-Spearing L, Zioupos P. Mechanical properties and the hierarchical structure of bone. *Med Eng Phys*. 1998;20(2):92-102. http://www.ncbi.nlm.nih.gov/pubmed/9679227. Accessed June 14, 2016.
43. Weiner S, Wagner HD. The material bone: structure-mechanical function relations. *Annu Rev Mater Sci*. 1998;28:271-298.
44. Asefa T, Yoshina-Ishii C, MacLachlan MJ, Ozin GA. New nanocomposites: putting organic function “inside” the channel walls of periodic mesoporous silica. *J Mater Chem*. 2000;10(8):1751-1755. doi:10.1039/b000950o.
45. Zimmermann EA, Gludovatz B, Schaible E, Busse B, Ritchie RO. Fracture resistance of human cortical bone across multiple length-scales at physiological strain rates. *Biomaterials*. 2014;35(21):5472-5481. doi:10.1016/j.biomaterials.2014.03.066.
46. Griffith1921fracture.pdf.
47. Carter DR, Hayes WC. The compressive behavior of bone as a two-phase porous structure. *J Bone Joint Surg Am*. 1977;59(7):954-962. http://www.ncbi.nlm.nih.gov/pubmed/561786. Accessed June 9, 2016.
48. Carter DR, Spengler DM. Mechanical properties and composition of cortical bone. *Clin Orthop Relat Res*. 1978;(135):192-217. http://www.ncbi.nlm.nih.gov/pubmed/361320. Accessed June 9, 2016.
49. Gibson LJ, Ashby MF, Behrens JC, et al. The mechanical behaviour of cancellous bone. *J Biomech*. 1985;18(5):317-328. doi:10.1016/0021-9290(85)90287-8.
50. Goldstein SA. The mechanical properties of trabecular bone: dependence on anatomic location and function. *J Biomech*. 1987;20(11-12):1055-1061. http://www.ncbi.nlm.nih.gov/pubmed/3323197. Accessed June 9, 2016.
51. Rice JC, Cowin SC, Bowman JA. On the dependence of the elasticity and strength of cancellous bone on apparent density. *J Biomech*. 1988;21(2):155-168. http://www.ncbi.nlm.nih.gov/pubmed/3350829. Accessed June 9, 2016.
52. Martin RB. Determinants of the mechanical properties of bones. *J Biomech*. 1991;24 Suppl 1:79-88. http://www.ncbi.nlm.nih.gov/pubmed/1842337. Accessed June 9, 2016.
53. Lin D, Li Q, Li W, Swain M. Dental implant induced bone remodeling and associated algorithms. *J Mech Behav Biomed Mater*. 2009;2(5):410-432. doi:10.1016/j.jmbbm.2008.11.007.
54. Kayabaşı O, Yüzbasıoğlu E, Erzincanlı F. Static, dynamic and fatigue behaviors of dental implant using finite element method. *Adv Eng Softw*. 2006;37(10):649-658. doi:10.1016/j.advengsoft.2006.02.004.
55. Bozkaya D, Muftu S, Muftu A. Evaluation of load transfer characteristics of five different implants in compact bone at different load levels by finite elements analysis. *J Prosthet Dent*. 2004;92(6):523-530. doi:10.1016/j.prosdent.2004.07.024.
56. Meri?? G, Erkmen E, Kurt A, Eser A, ??elik G. Biomechanical evaluation of a fiber-reinforced composite prosthesis supported by implants with and without a microthread collar design. *J Dent Sci*. 2010;5(4):201-208. doi:10.1016/j.jds.2010.11.010.

57. Weinstein AM, Klawitter JJ, Anand SC, Schuessler R. Stress analysis of porous rooted dental implants. *J Dent Res*. 1976;55(5):772-777. http://www.scopus.com/inward/record.url?eid=2-s2.0-0017093130&partnerID=tZOtx3y1.
58. Mohammed H, Atmaram GH, Schoen FJ. Dental implant design: a critical review. *J Oral Implantol*. 1979;8(3):393-410. http://www.scopus.com/inward/record.url?eid=2-s2.0-0018556657&partnerID=tZOtx3y1.
59. Atmaram GH, Mohammed H. Stress analysis of single-tooth implants. I. Effect of elastic parameters and geometry of implant. *Implantologist*. 1983;3(1):24-29. http://www.scopus.com/inward/record.url?eid=2-s2.0-0020933362&partnerID=tZOtx3y1.
60. Atmaram GH, Mohammed H. Stress analysis of single-tooth implants. II. Effect of implant root-length variation and pseudo periodontal ligament incorporation. *Implantologist*. 1983;3(1):58-62. http://www.scopus.com/inward/record.url?eid=2-s2.0-0020898298&partnerID=tZOtx3y1.
61. Borchers L, Reichart P. Three-dimensional stress distribution around a dental implant at different stages of interface development. *J Dent Res*. 1983;62(2):155-159. http://www.scopus.com/inward/record.url?eid=2-s2.0-0020711801&partnerID=tZOtx3y1.
62. Cook SD, Weinstein AM, Klawitter JJ. A three-dimensional finite element analysis of a porous rooted Co-Cr-Mo alloy dental implant. *J Dent Res*. 1982;61(1):25-29. http://www.scopus.com/inward/record.url?eid=2-s2.0-0020020445&partnerID=tZOtx3y1.
63. Meroueh K. Finite element analysis of partially edentulous mandible rehabilitated with an osteointegrated cylindrical implant. *J oral …*. 1987. http://www.ncbi.nlm.nih.gov/pubmed/3077414. Accessed February 1, 2016.
64. Williams KR, Watson CJ, Murphy WM, Scott J, Gregory M, Sinobad D. Finite element analysis of fixed prostheses attached to osseointegrated implants. *Quintessence Int (Berl)*. 1990;21(7):563-570. http://www.scopus.com/inward/record.url?eid=2-s2.0-0025463278&partnerID=tZOtx3y1.
65. Akpinar I, Demirel F, Parnas L, Sahin S. A comparison of stress and strain distribution characteristics of two different rigid implant designs for distal-extension fixed prostheses. *Quintessence Int (Berl)*. 1996;27(1):11-17. http://www.scopus.com/inward/record.url?eid=2-s2.0-0029678751&partnerID=tZOtx3y1.
66. Korioth T, Versluis A. Modeling the mechanical behavior of the jaws and their related structures by finite element (FE) analysis. *Crit Rev Oral Biol …*. 1997. http://cro.sagepub.com/content/8/1/90.short. Accessed February 1, 2016.
67. Oosterwyck H Van. The influence of bone mechanical properties and implant fixation upon bone loading around oral implants. *Clin Oral …*. 1998. http://onlinelibrary.wiley.com/doi/10.1034/j.1600-0501.1996.090606.x/full. Accessed February 1, 2016.
68. Chou H-Y, Jagodnik JJ, Müftü S. Predictions of bone remodeling around dental implant systems. *J Biomech*. 2008;41(6):1365-1373. doi:10.1016/j.jbiomech.2008.01.032.
69. Lian Z, Guan H, Ivanovski S, Loo Y-C, Johnson NW, Zhang H. Effect of bone to implant contact percentage on bone remodelling surrounding a dental implant. *Int J Oral Maxillofac Surg*. 2010;39(7):690-698. doi:10.1016/j.ijom.2010.03.020.
70. JBelinha_Book_Chap_2013e.pdf.

Appendix 1

In this appendix is presented all the maps that corresponds to the Von Mises stress maps.

In each one, the first line corresponds to the Finite Element Method analysis, the second line corresponds to the Radial Point Interpolation Method analysis, and the third one corresponds to the analysis with Natural Neighbour Radial Point Interpolation Method.

For each one, the columns correspond to the angles, where, from left to right it is, 10º, 20º, 30º, 40º, 50º, 60º, 70º, 80º and 90º.

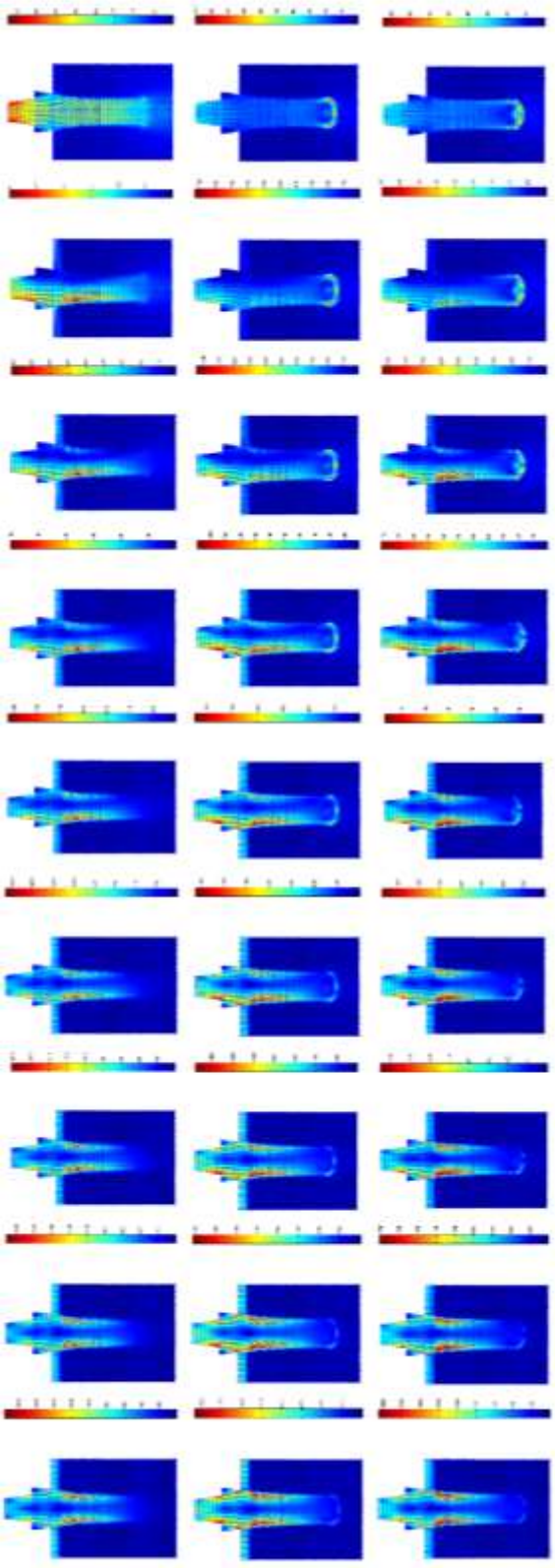

Figure A.1 Stress Map from 'Model 1' and bone type 1

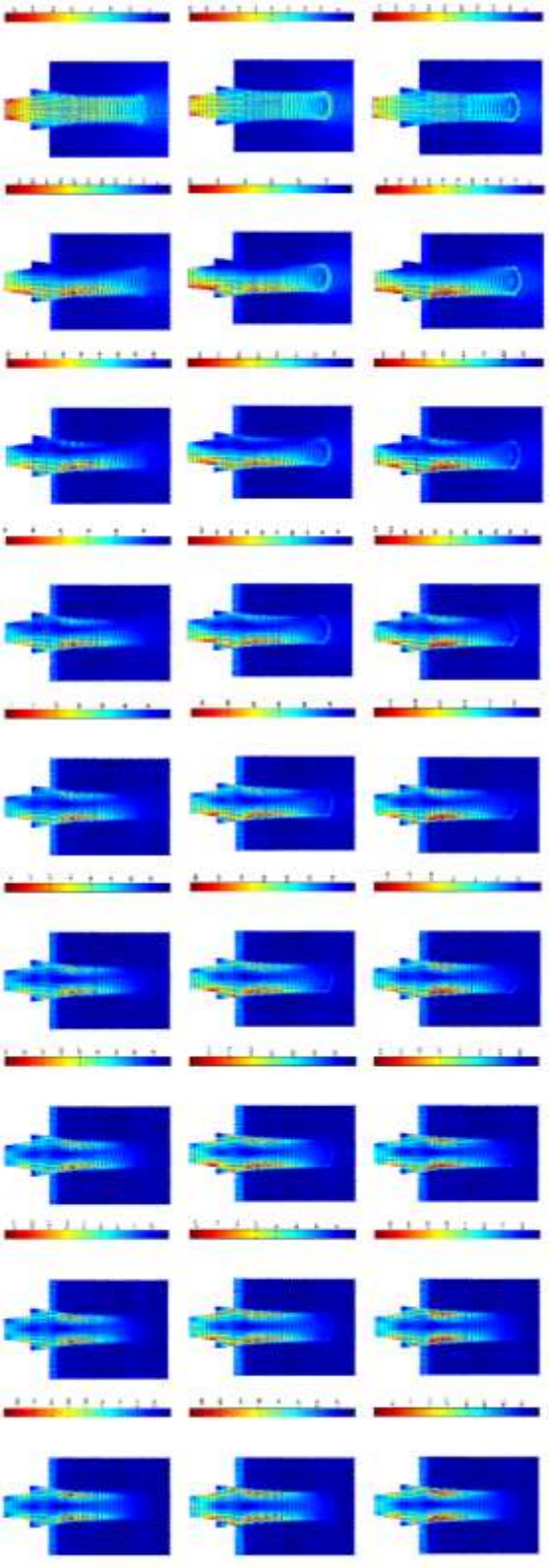

Figure A.2 Stress Map from 'Model 1' and bone type 2

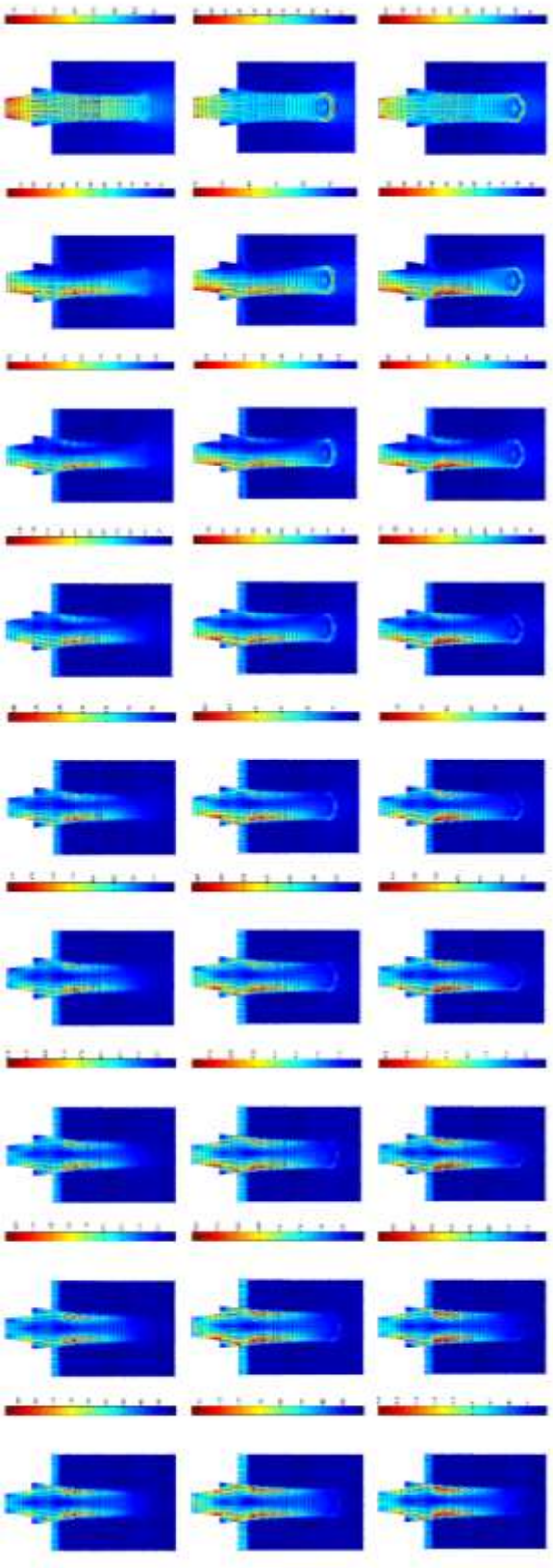

Figure A.3 Stress Map from 'Model 1' and bone type 3

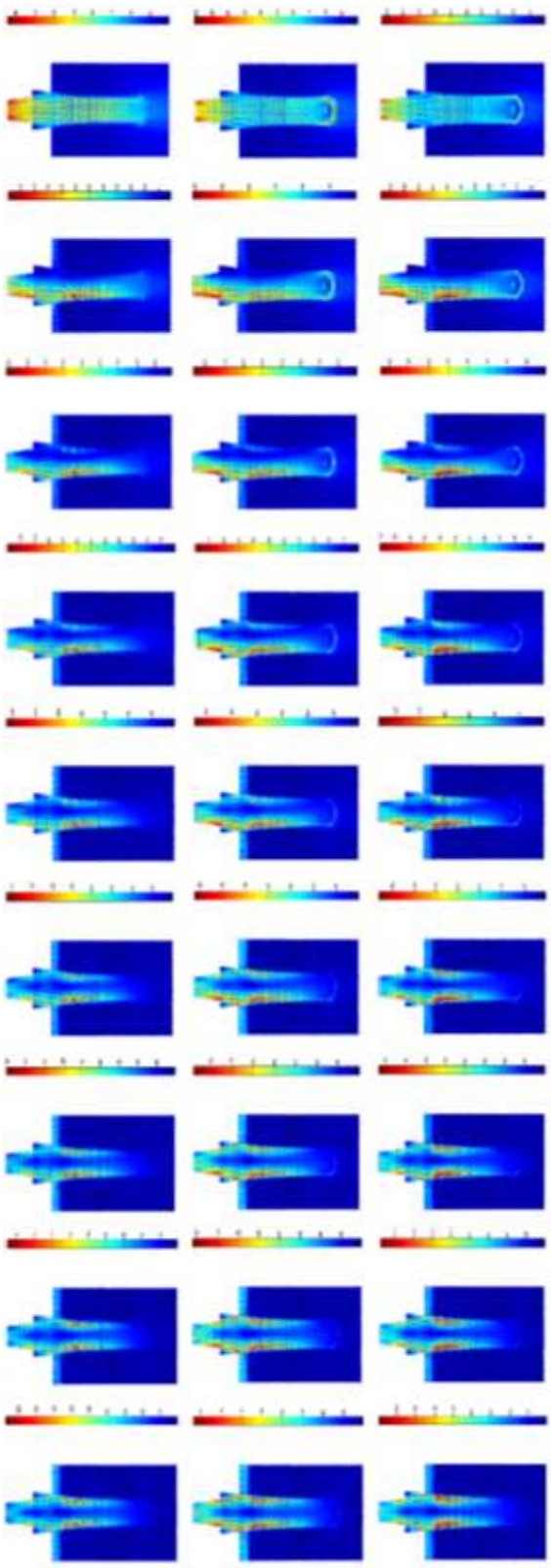

Figure A.4 Stress Map from 'Model 1' and bone type 4

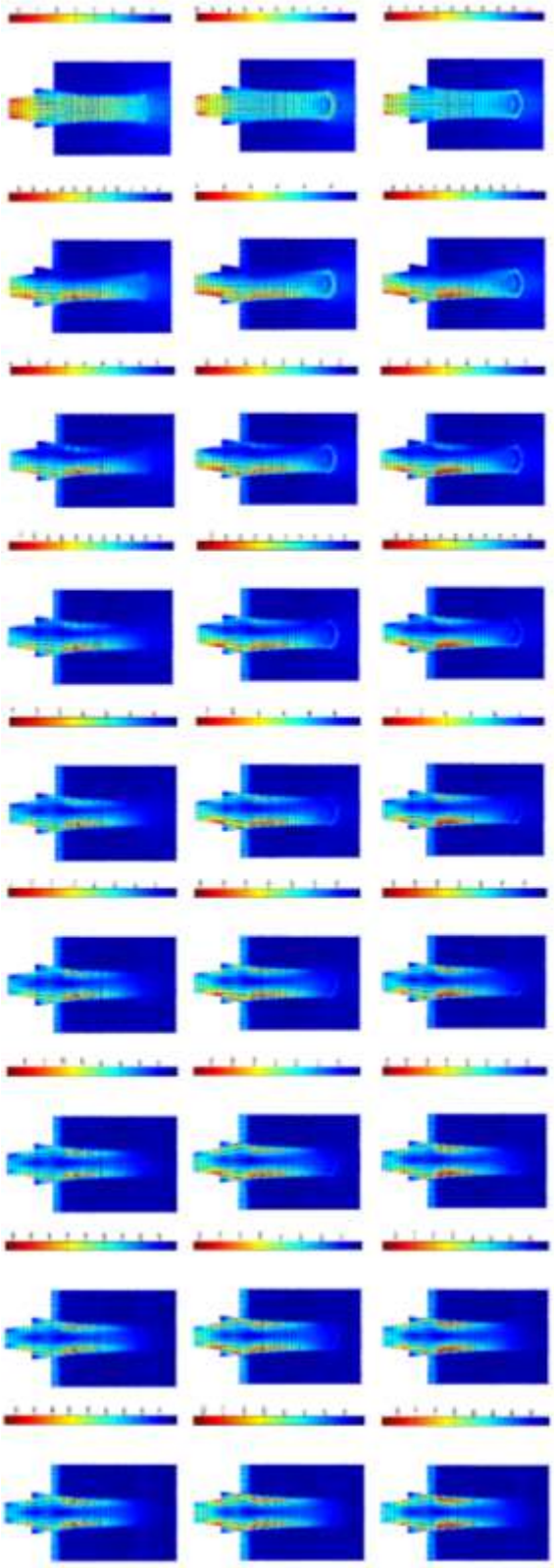

Figure A.5 Stress Map from 'Model 1' and bone type 5

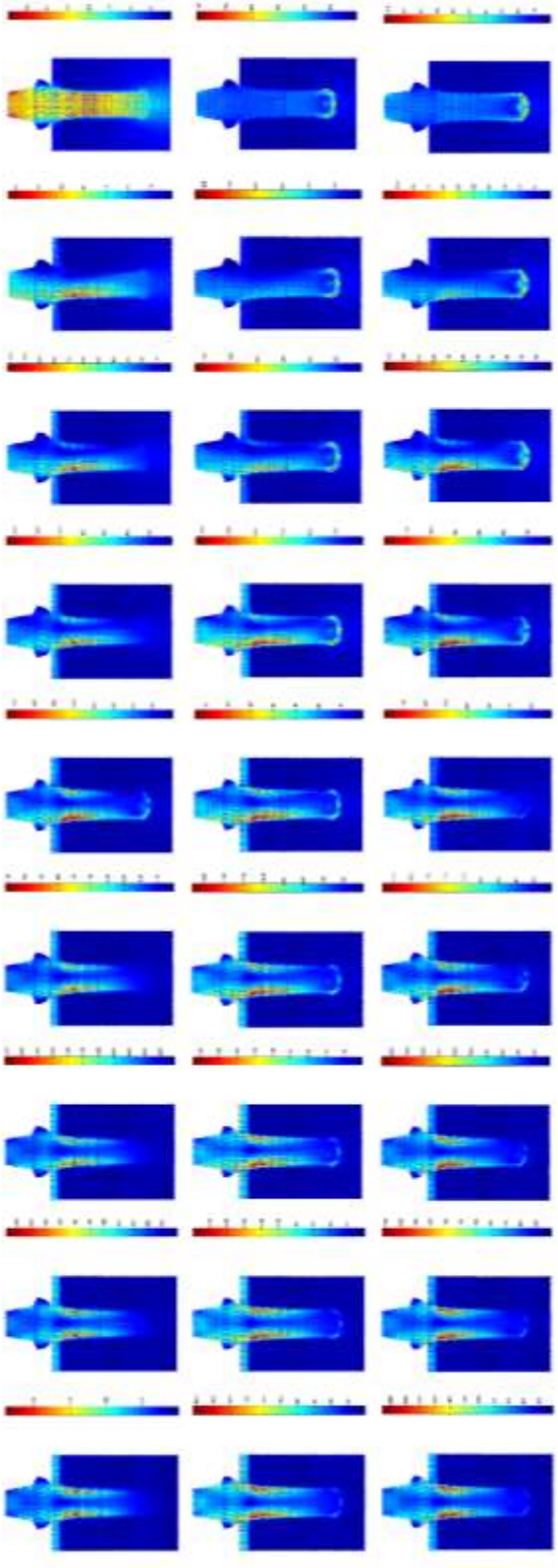

Figure A.6 Stress Map from 'Model 2' and bone type 1

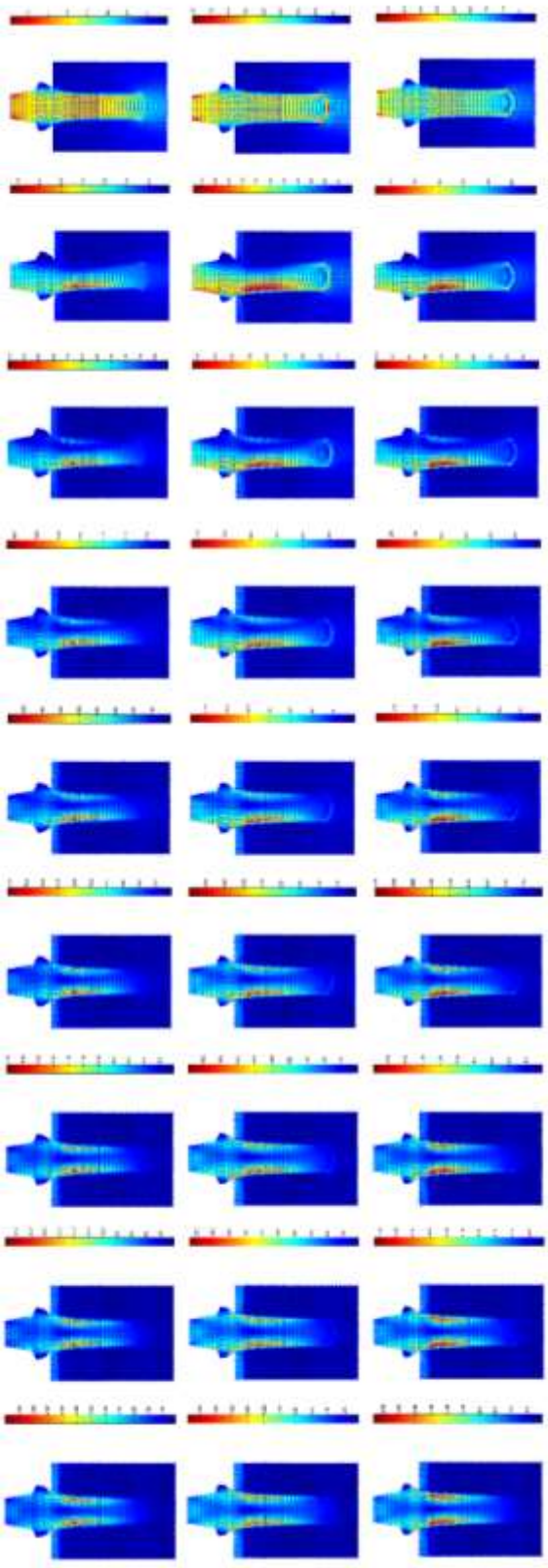

Figure A.7 Stress Map from 'Model 2' and bone type 2

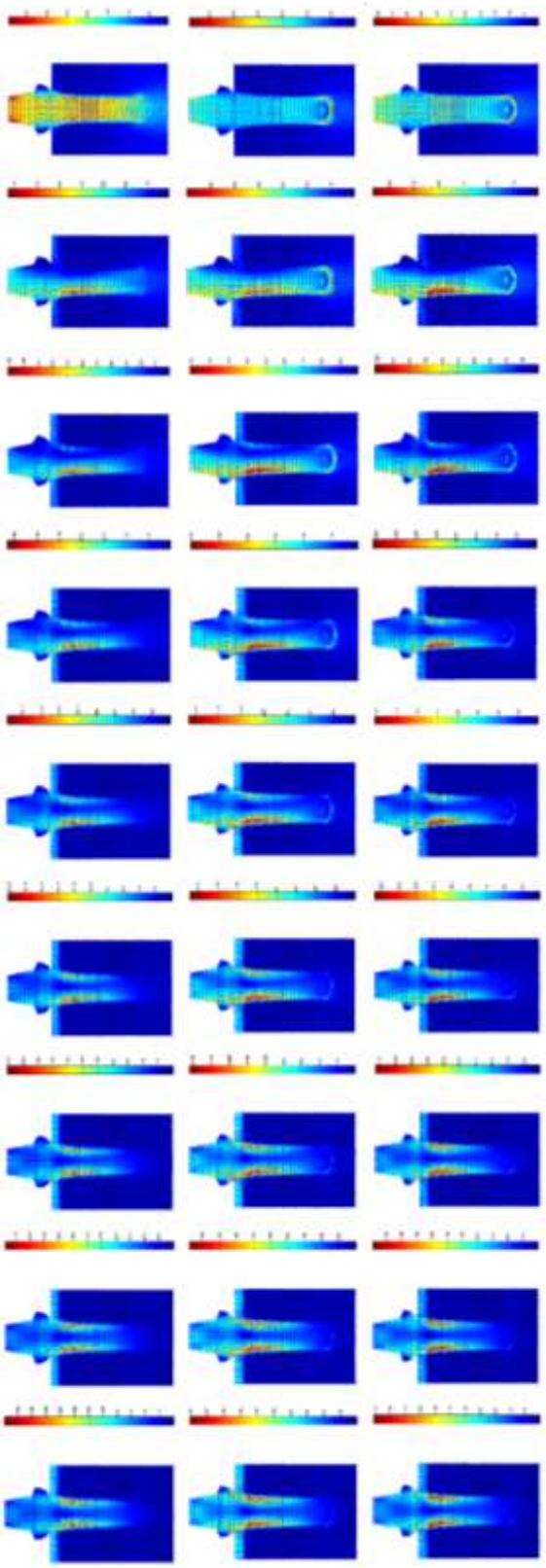

Figure A.8 Stress Map from 'Model 2' and bone type 3

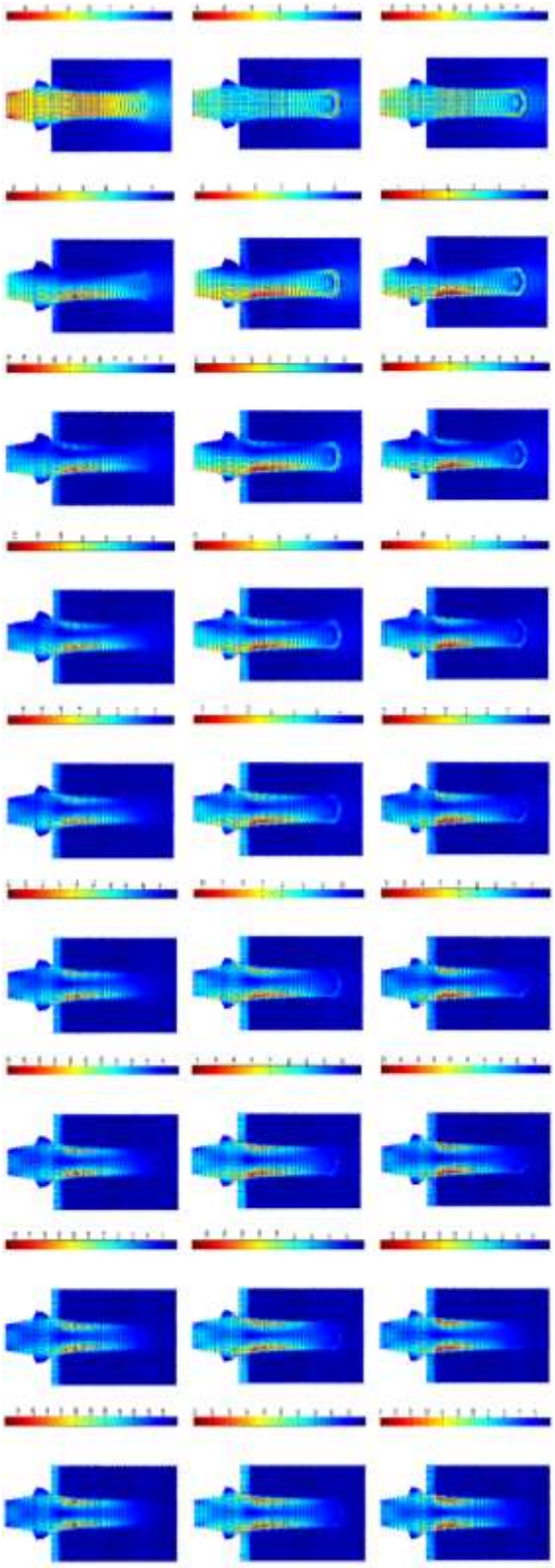

Figure A.9 Stress Map from 'Model 2' and bone type 4

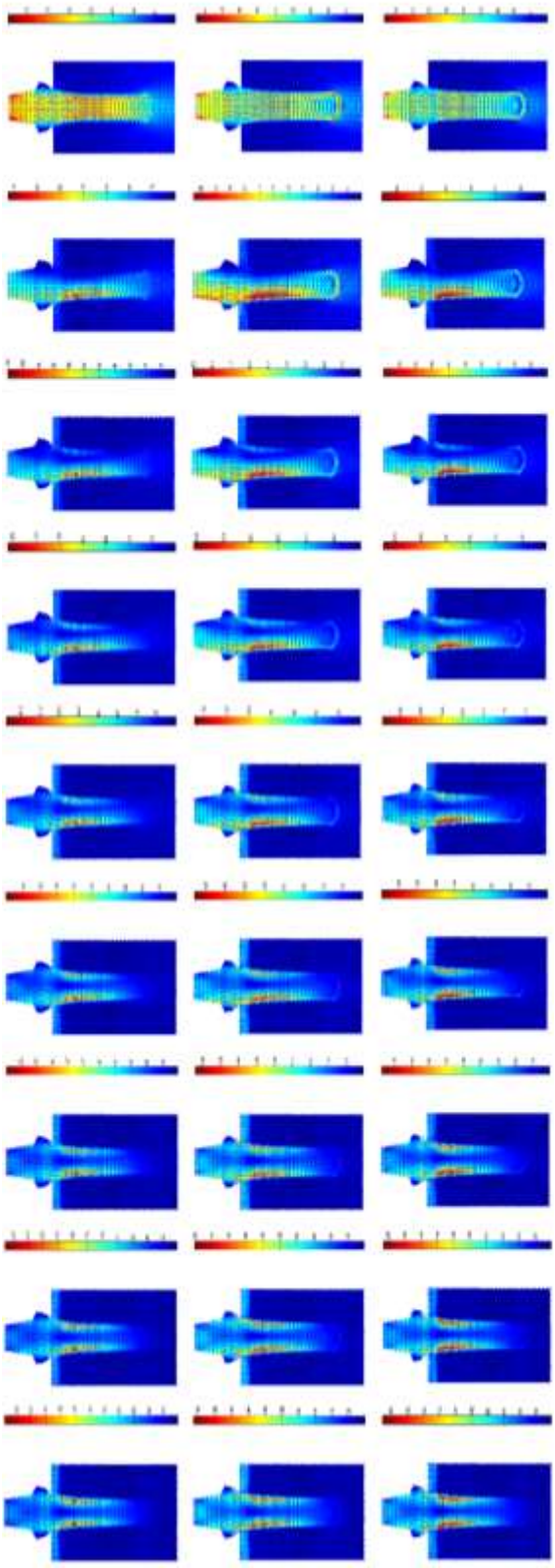

Figure A.10 Stress Map from 'Model 2' and bone type 5

Appendix 2

In this appendix, it is presented all the results, in this case graphics, relative to the analysis of the stress near the interface between implant and bone, for all the studied angles and for all the types of bones.

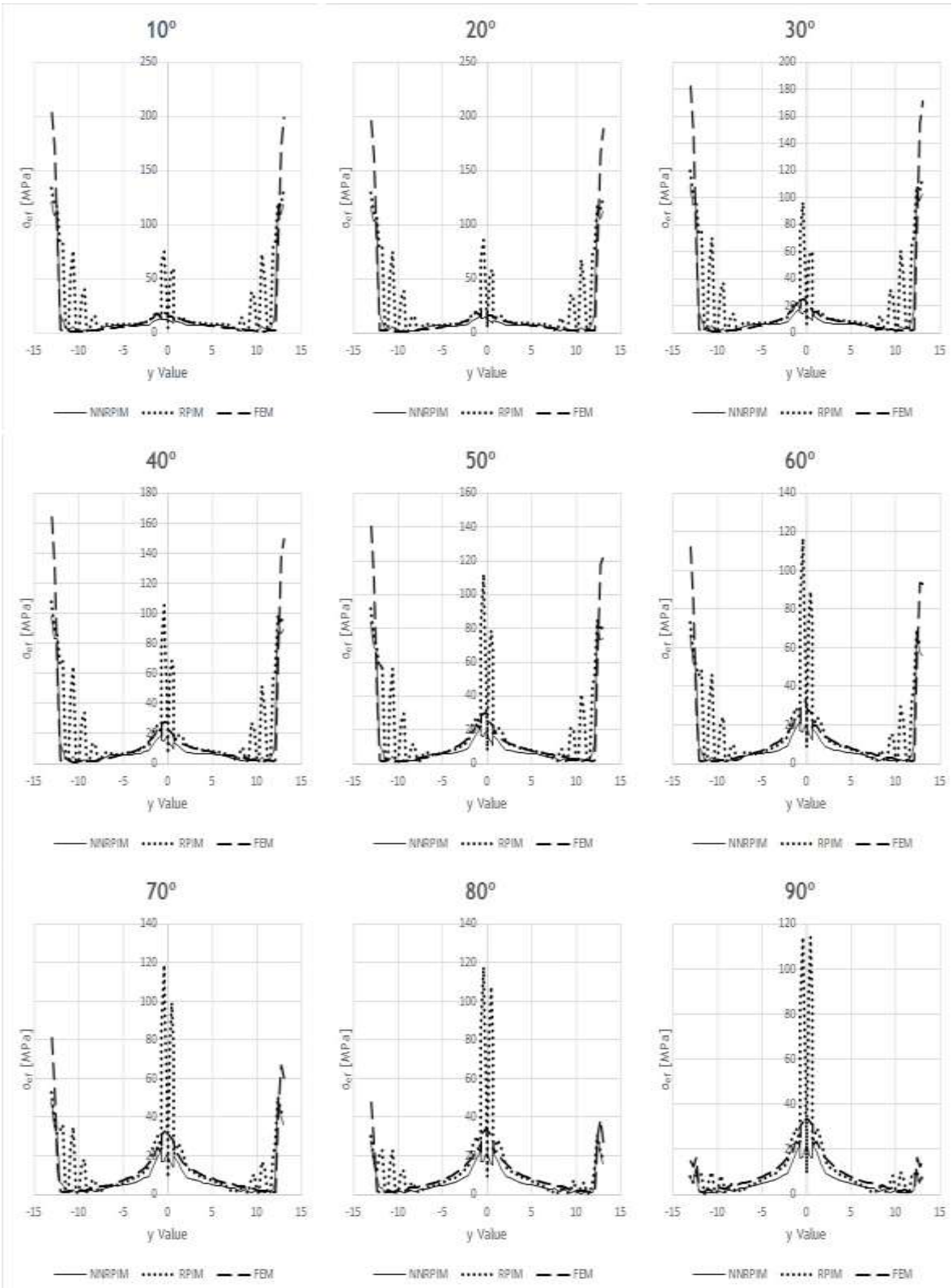

Figure A.11 Stress distribution from bone side, from 'Model 1', from bone type 1

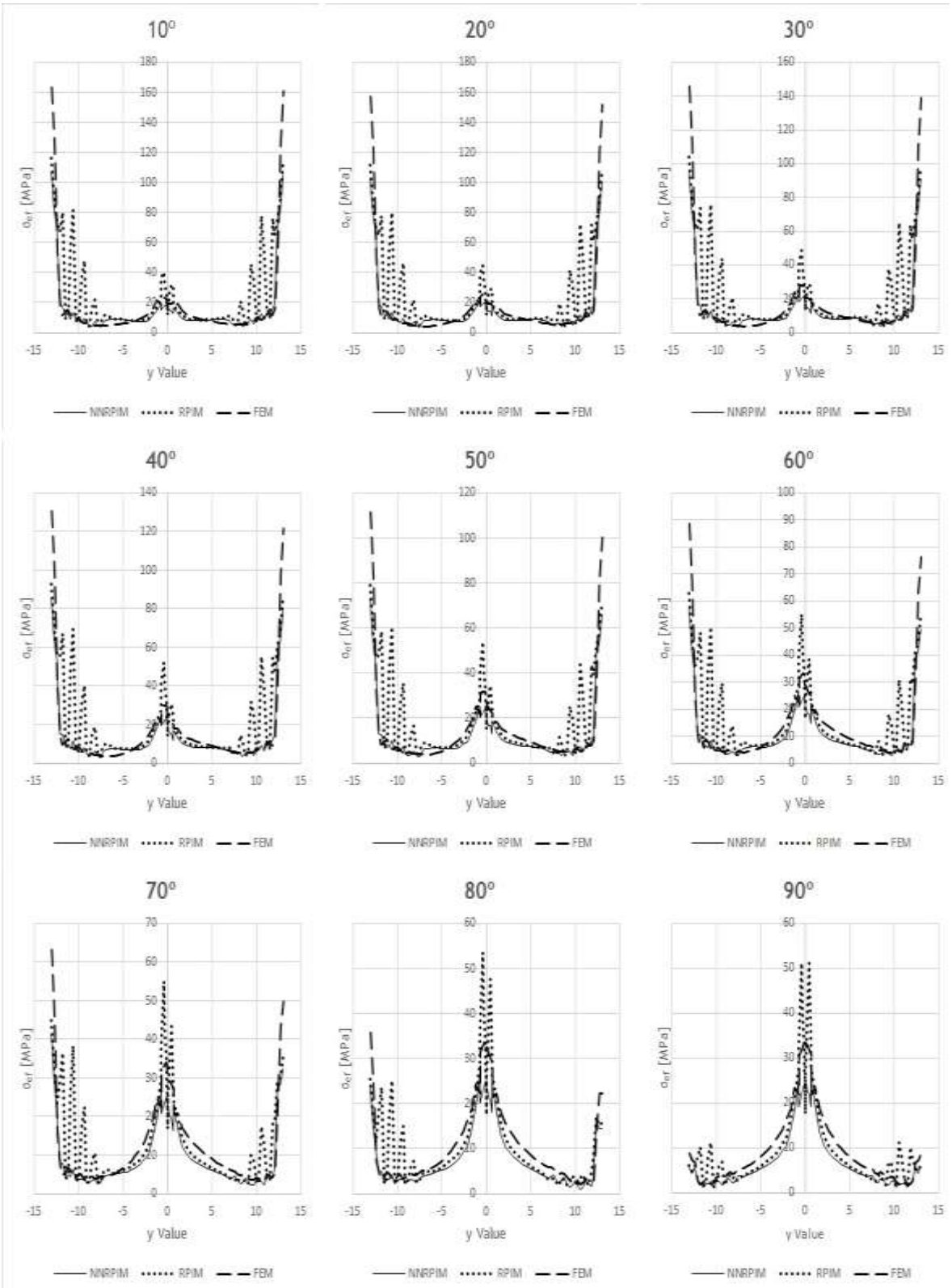

Figure A.12 Stress distribution from bone side, from 'Model 1', from bone type 2

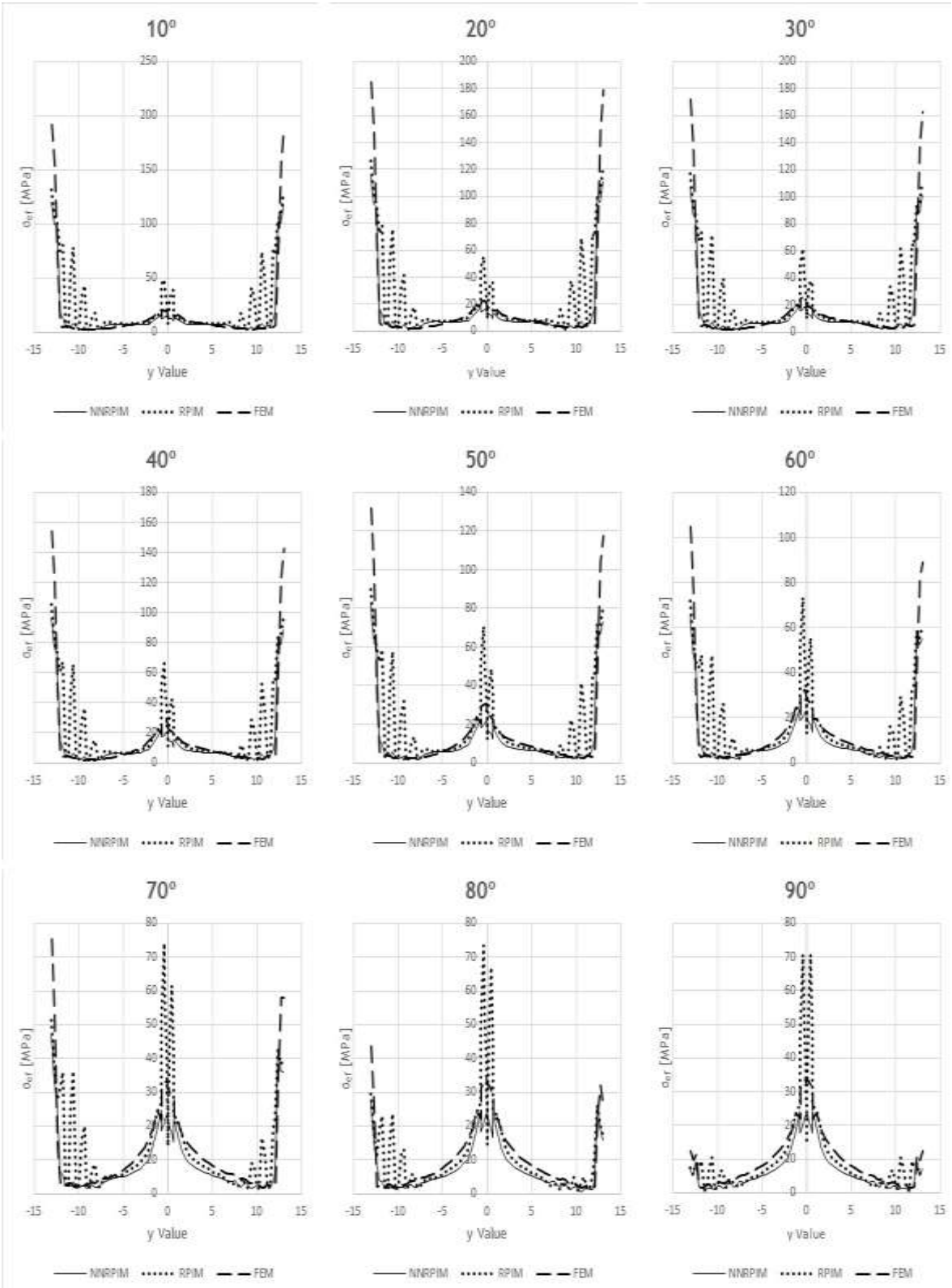

Figure A.13 Stress distribution from bone side, from 'Model 1', from bone type 3

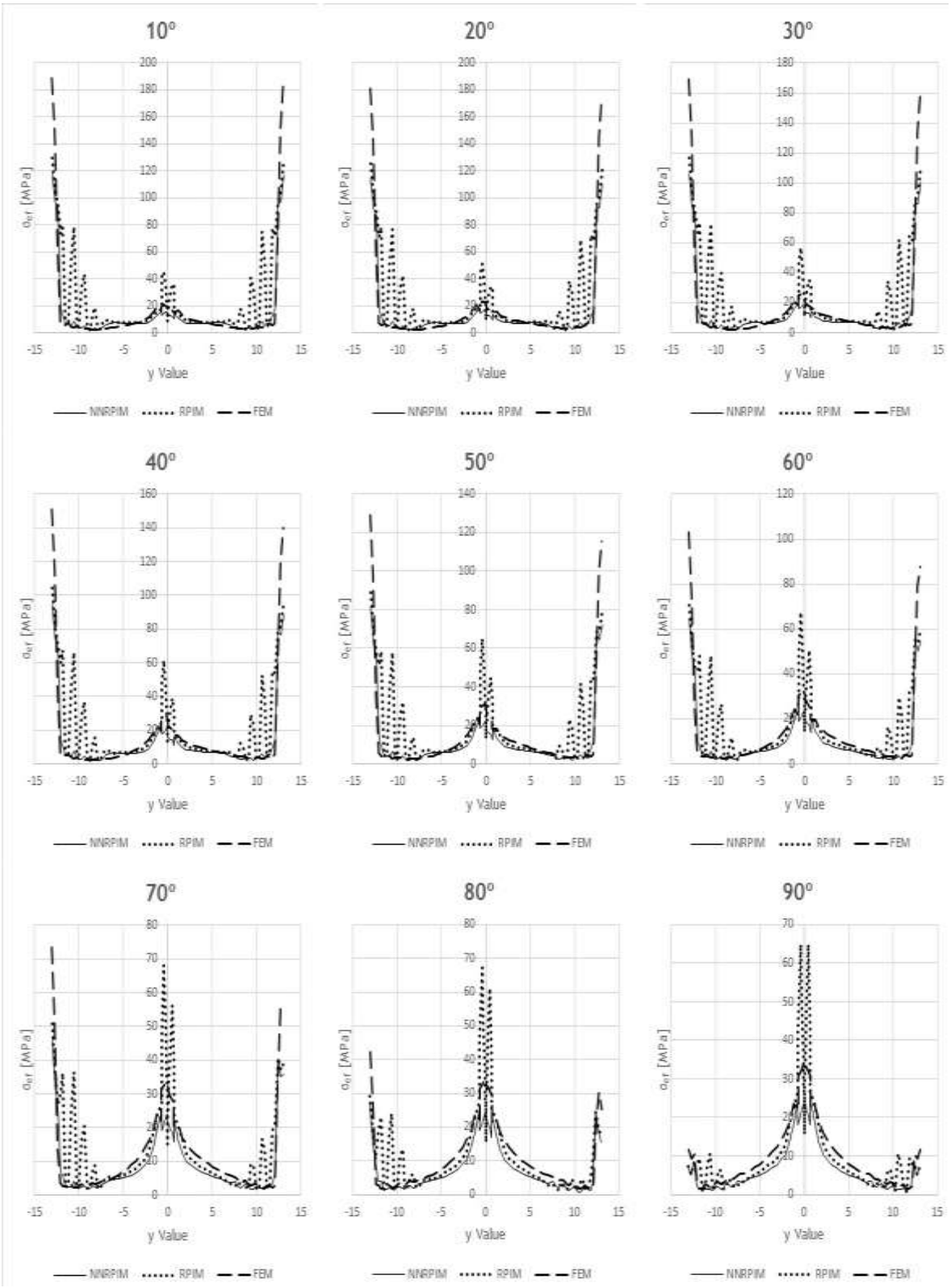

Figure A.14 Stress distribution from bone side, from 'Model 1', from bone type 4

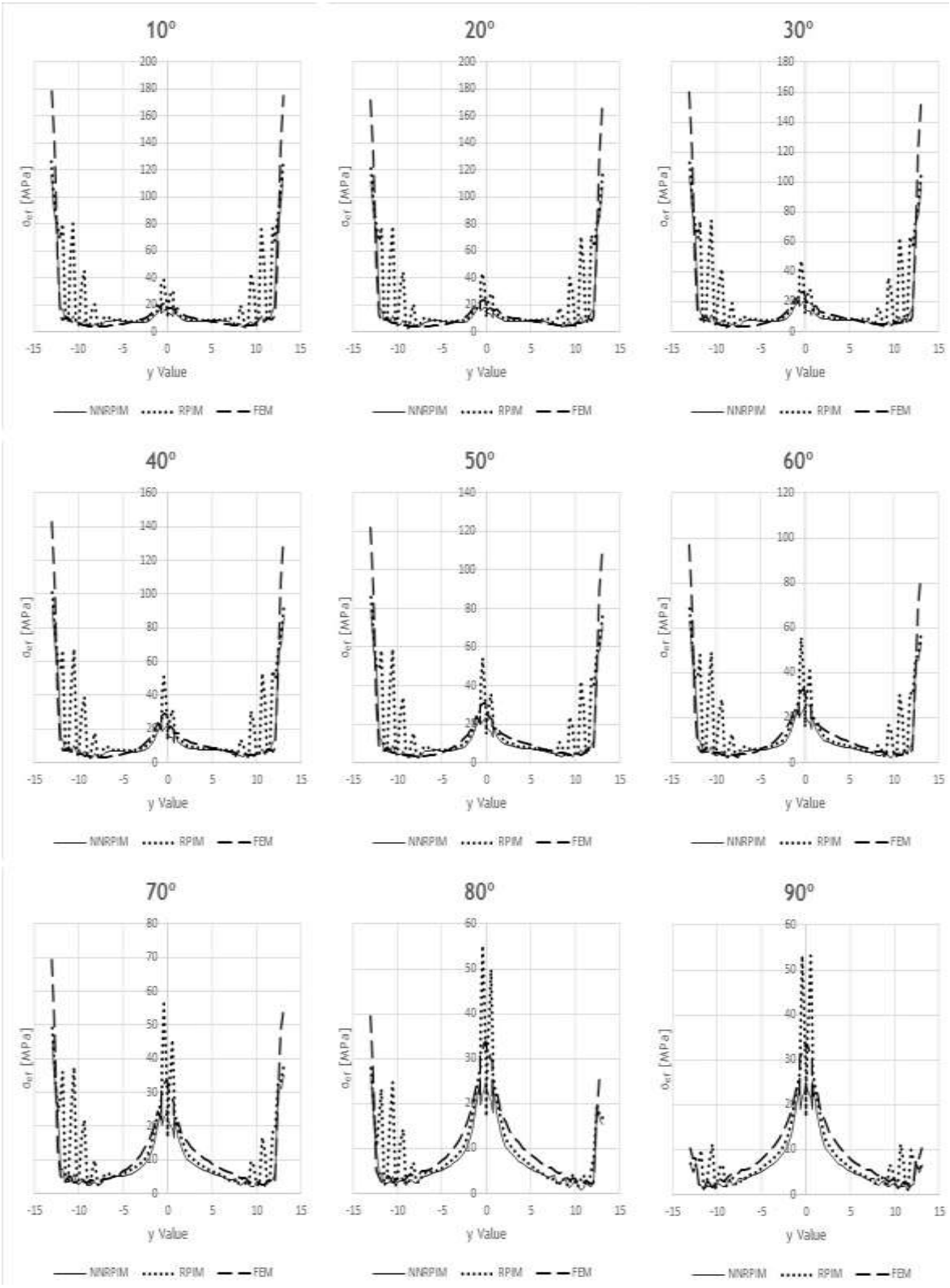

Figure A.15 Stress distribution from bone side, from 'Model 1', from bone type 5

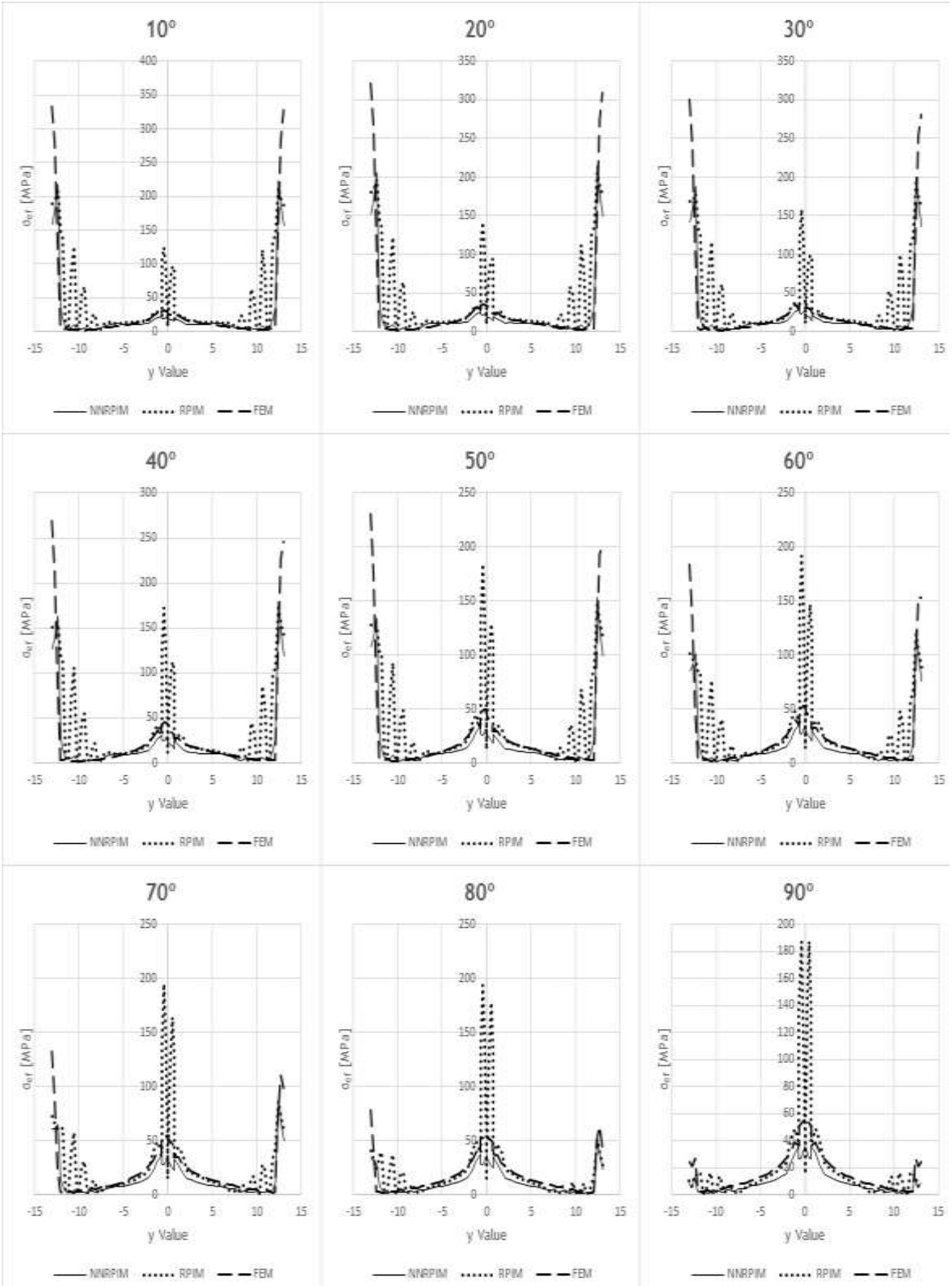

Figure A.16 Stress distribution from bone side, from 'Model 2', from bone type 1

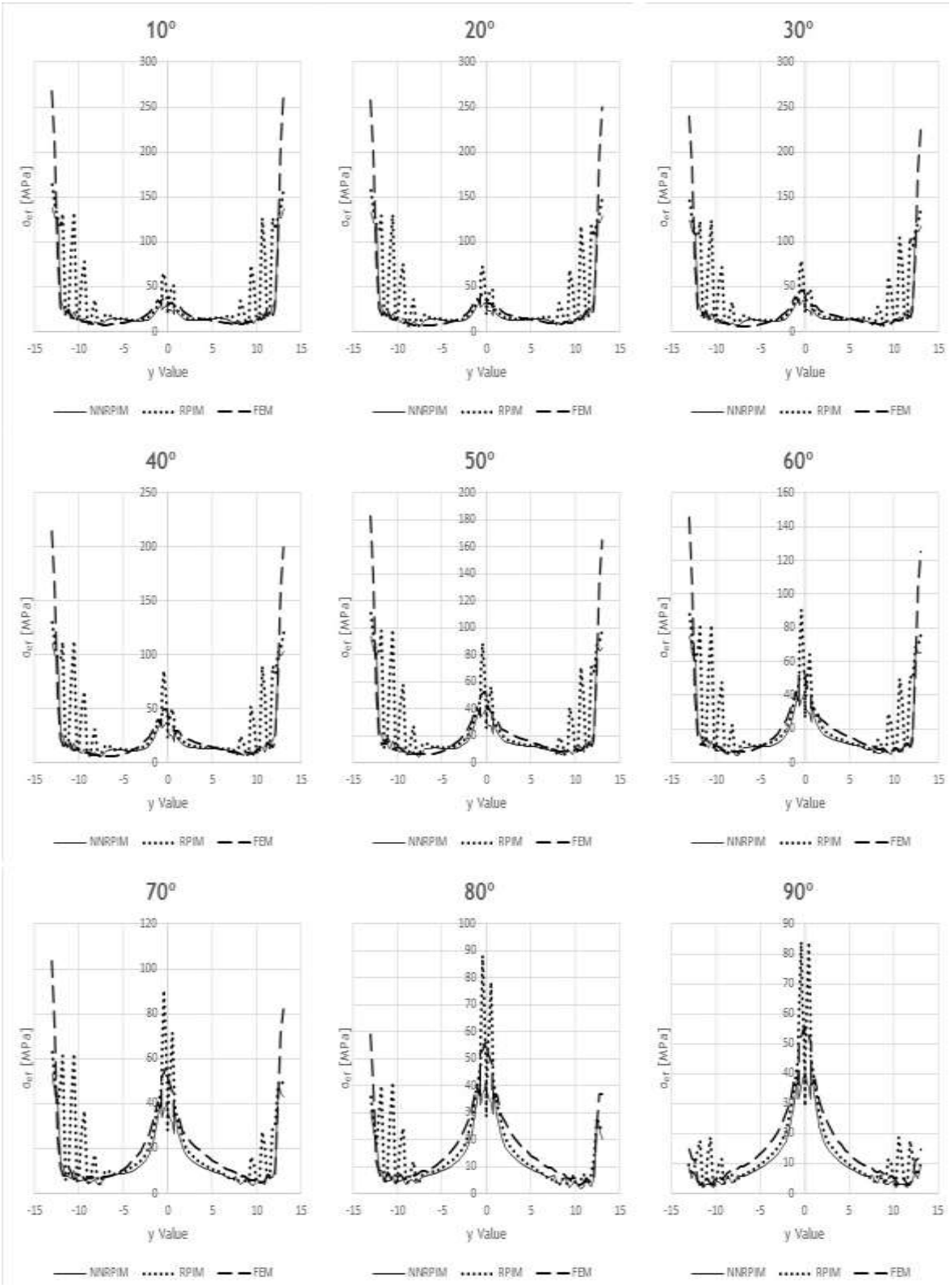

Figure A.17 Stress distribution from bone side, from 'Model 2', from bone type 2

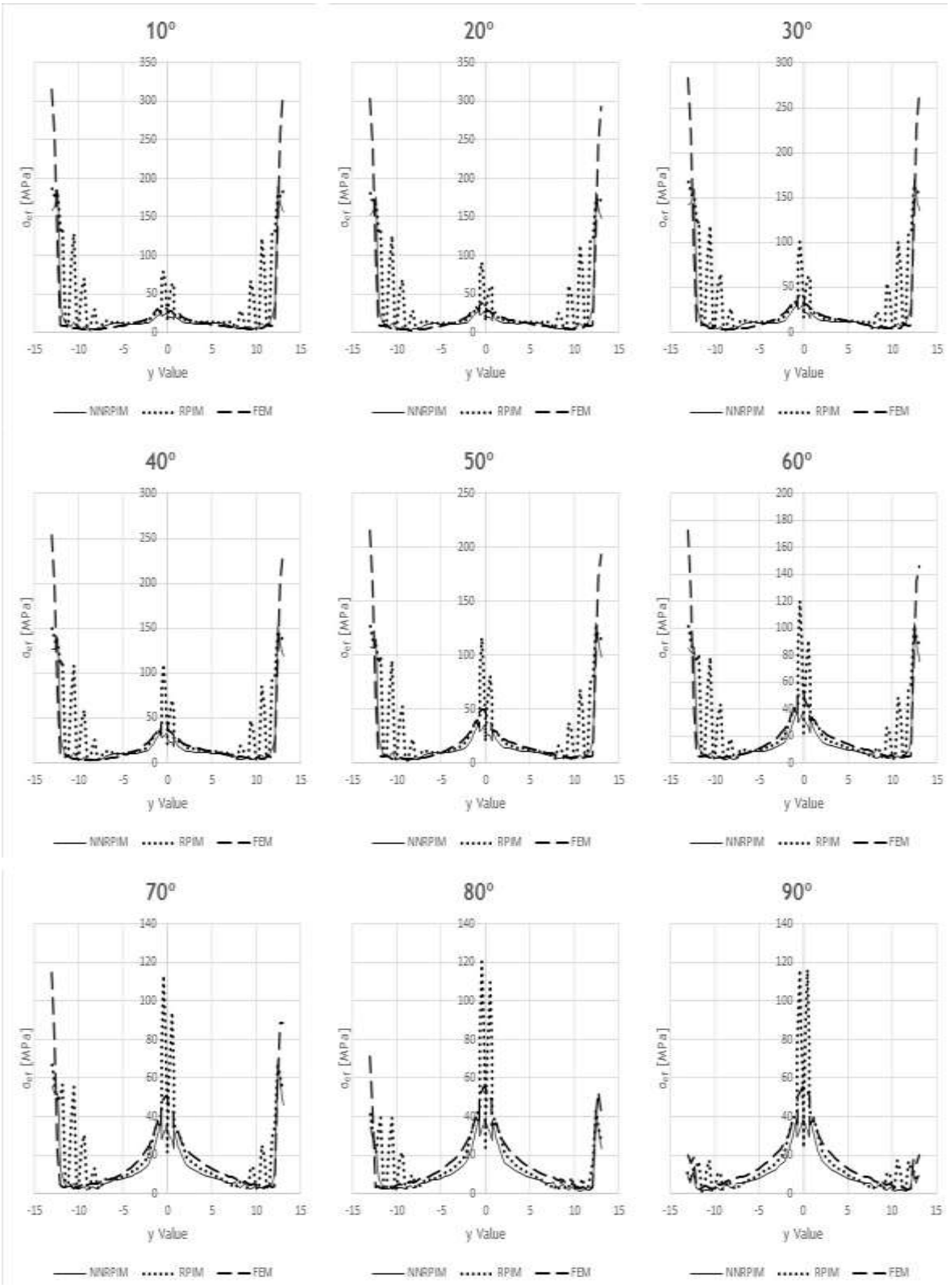

Figure A.18 Stress distribution from bone side, from 'Model 2', from bone type 3

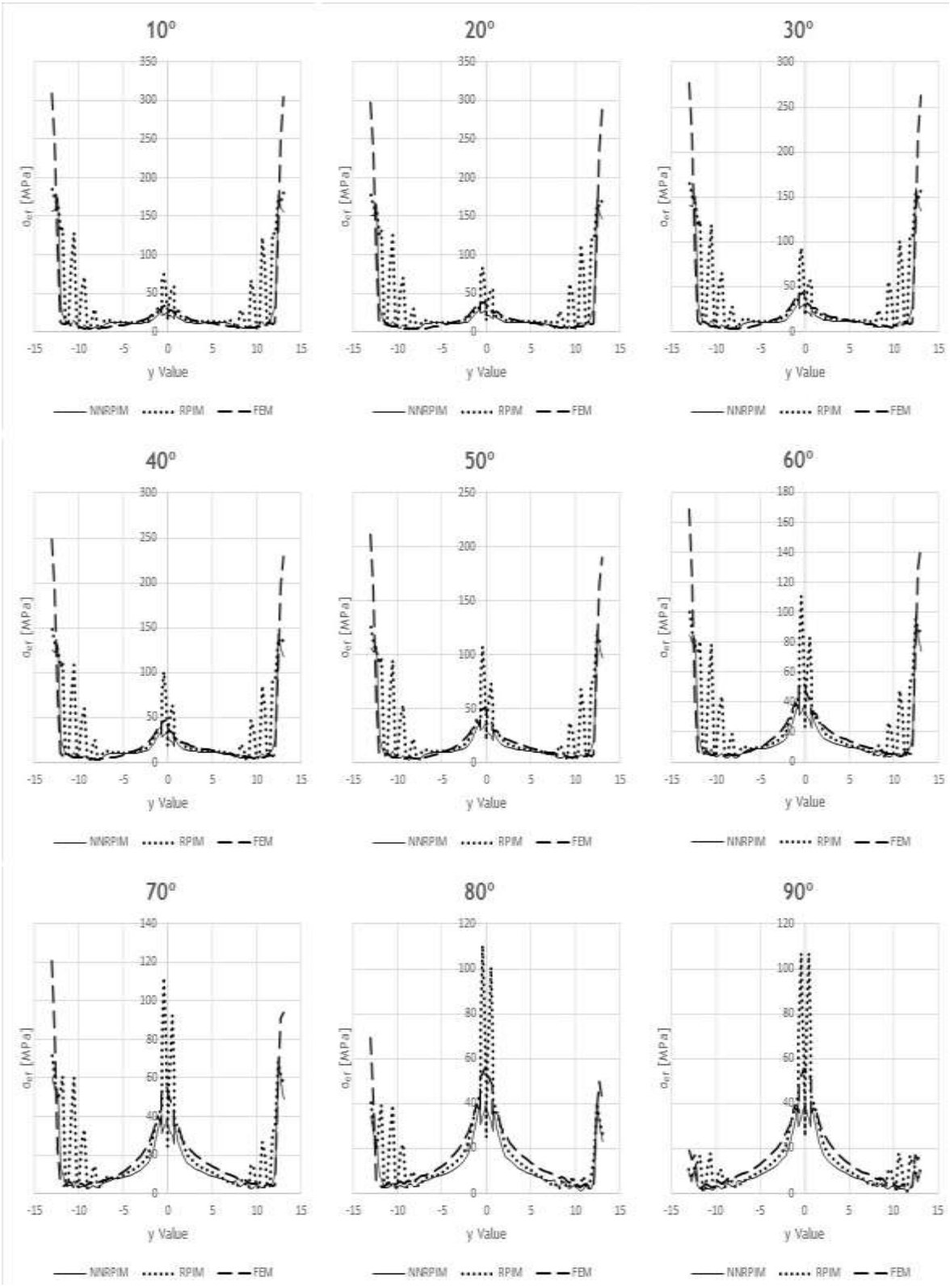

Figure A.19 Stress distribution from bone side, from 'Model 2', from bone type 4

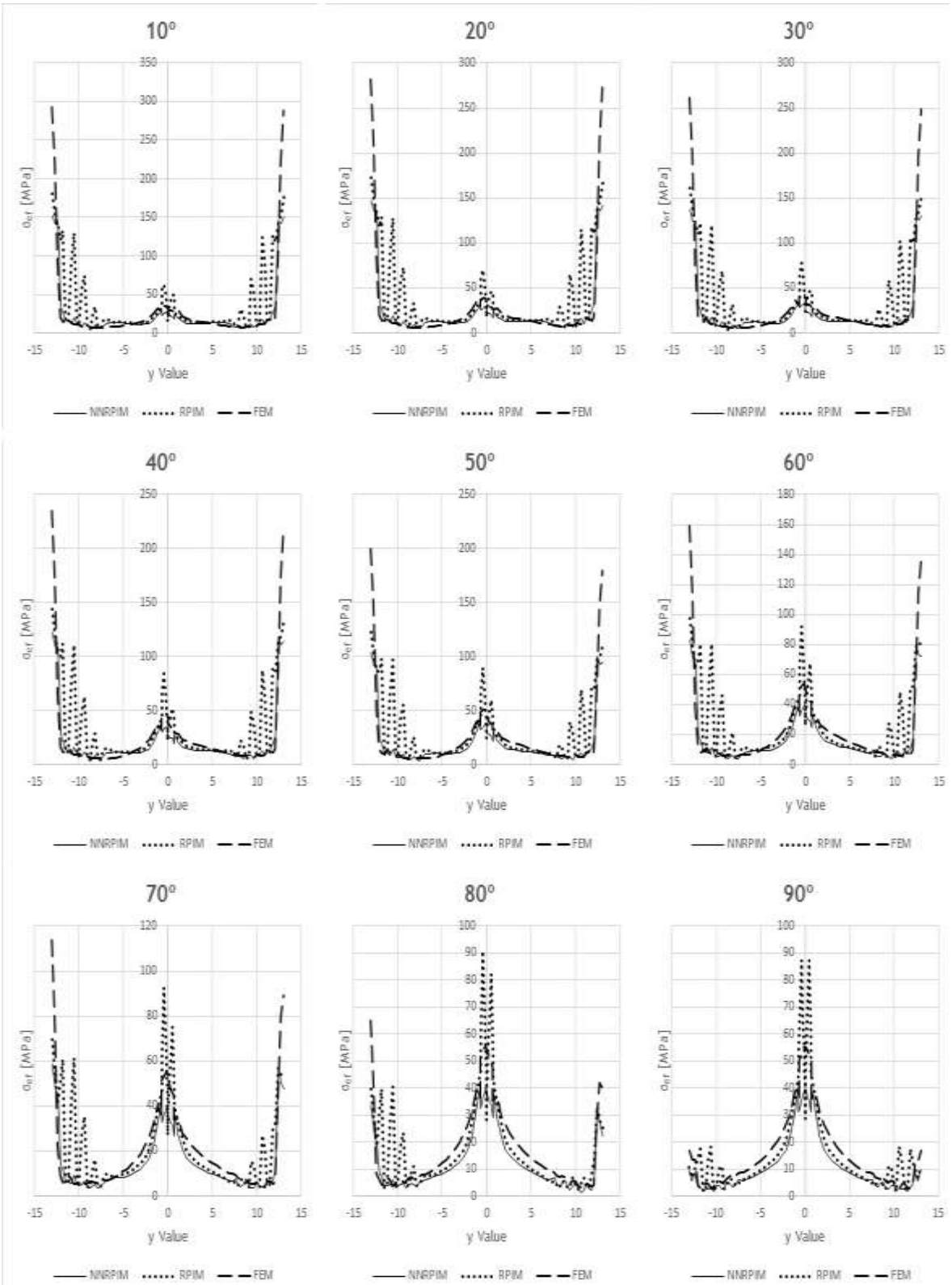

Figure A.20 Stress distribution from bone side, from 'Model 2', from bone type 5

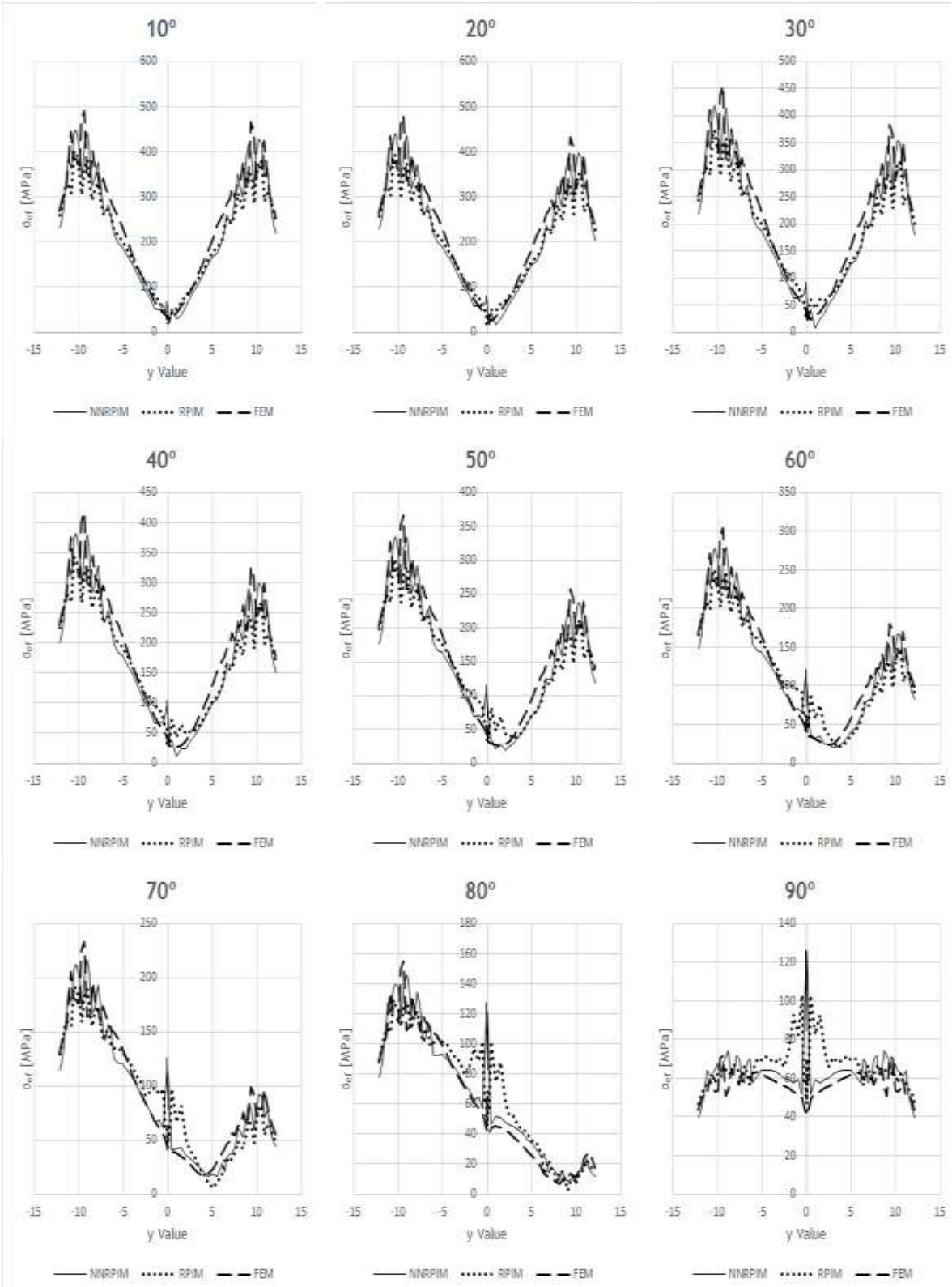

Figure A.21 Stress distribution from implant side, from 'Model 1', from bone type 1

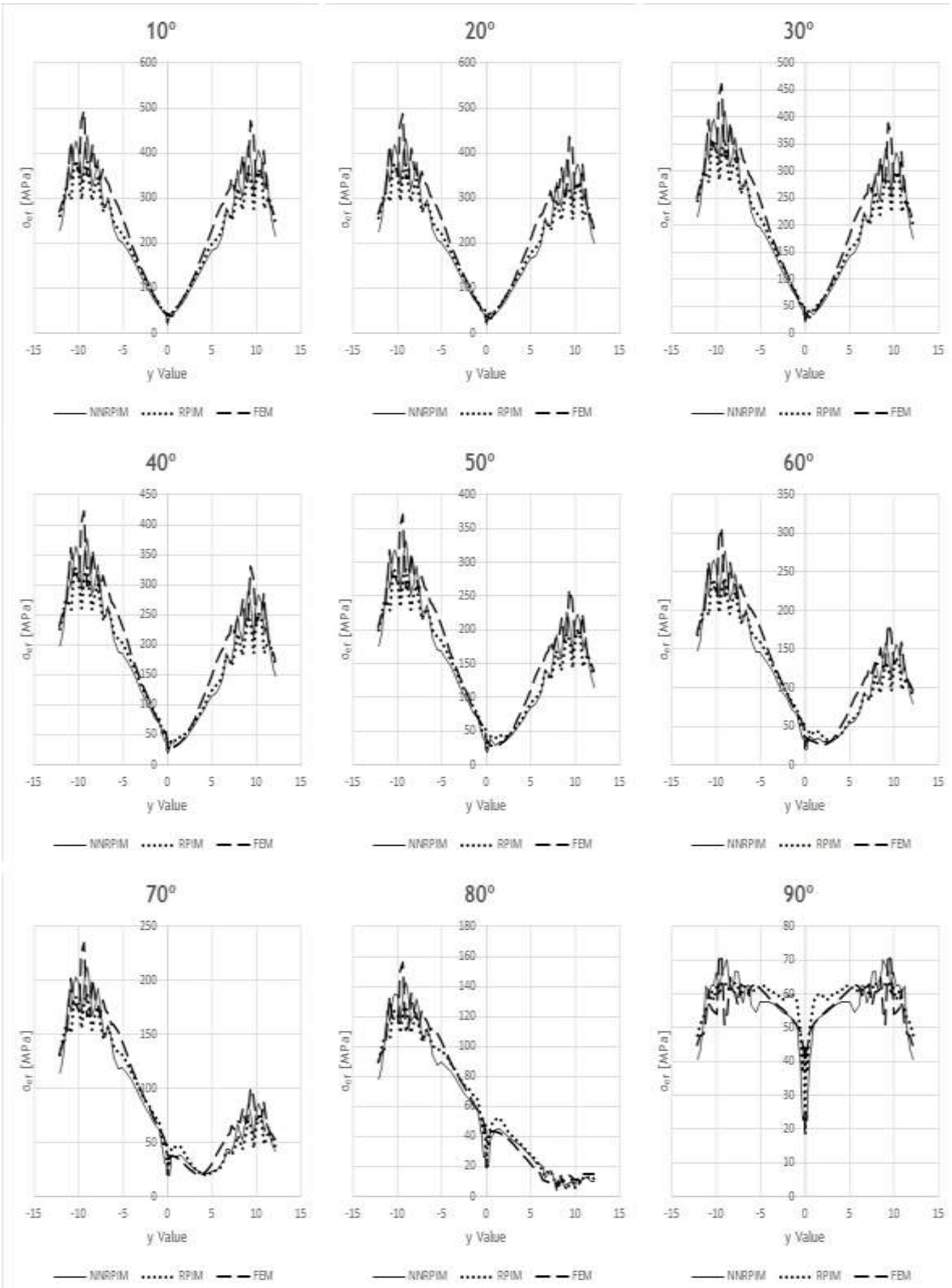

Figure A.22 Stress distribution from implant side, from 'Model 1', from bone type 2

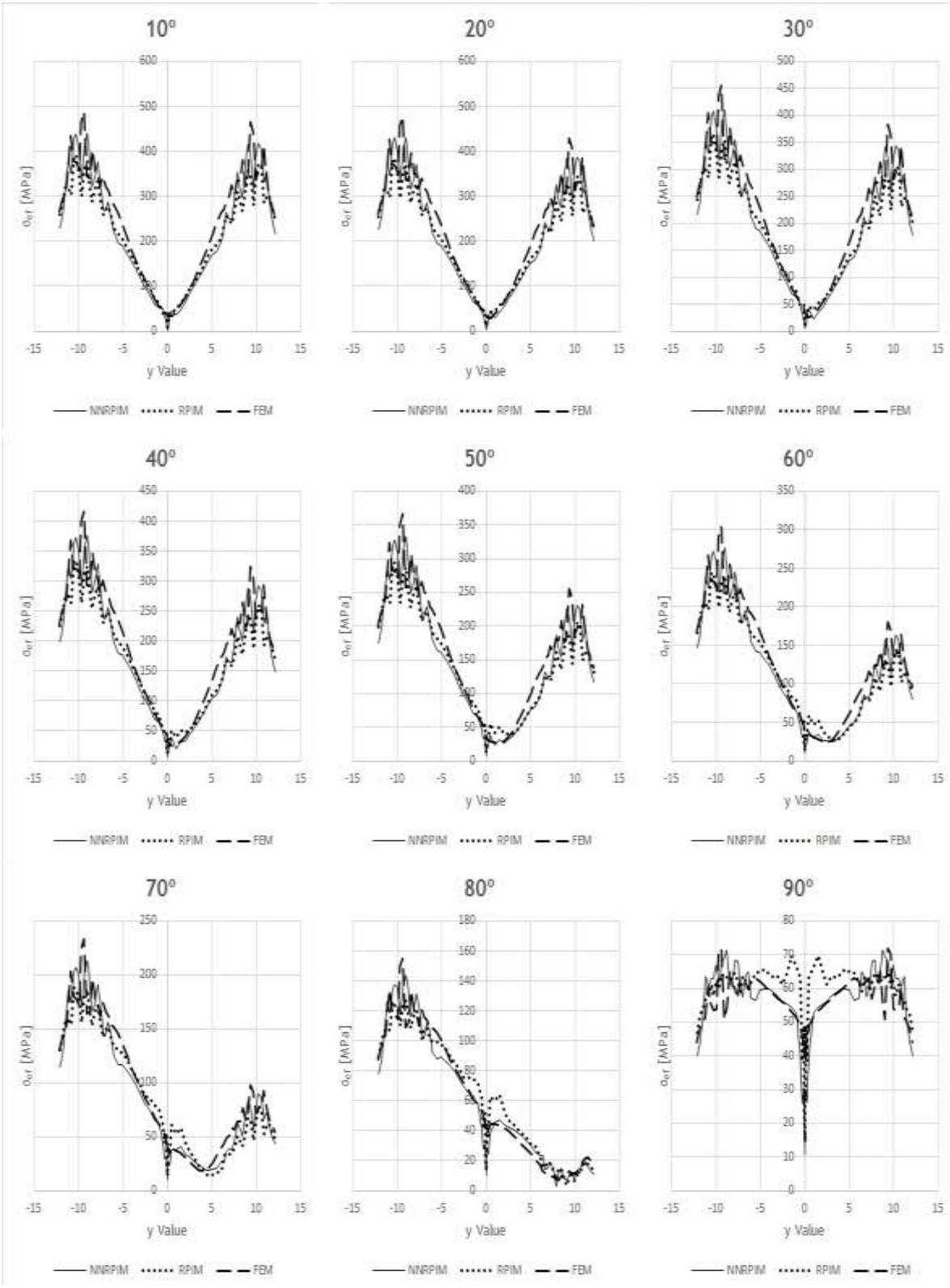

Figure A.23 Stress distribution from implant side, from 'Model 1', from bone type 3

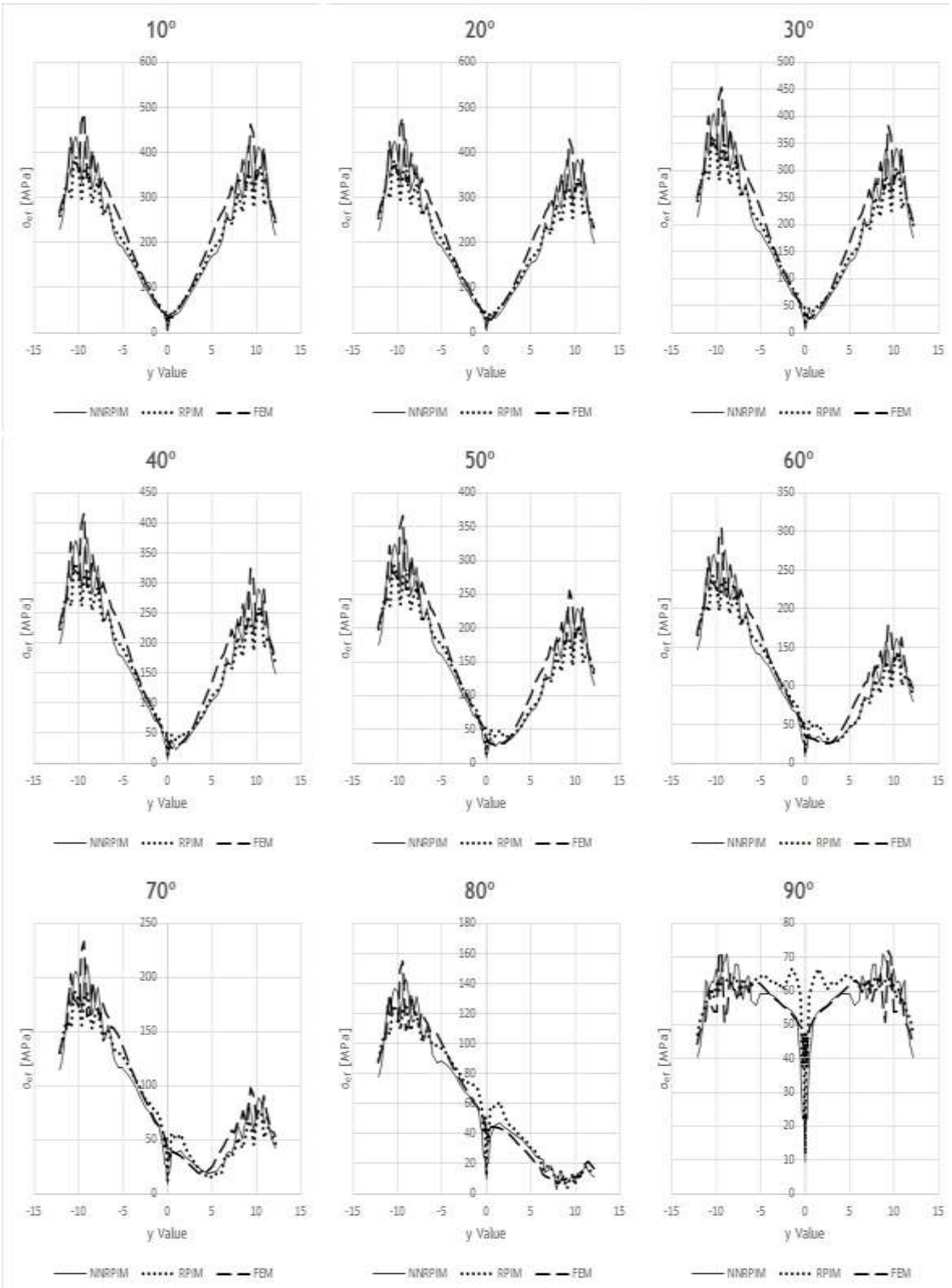

Figure A.24 Stress distribution from implant side, from 'Model 1', from bone type 4

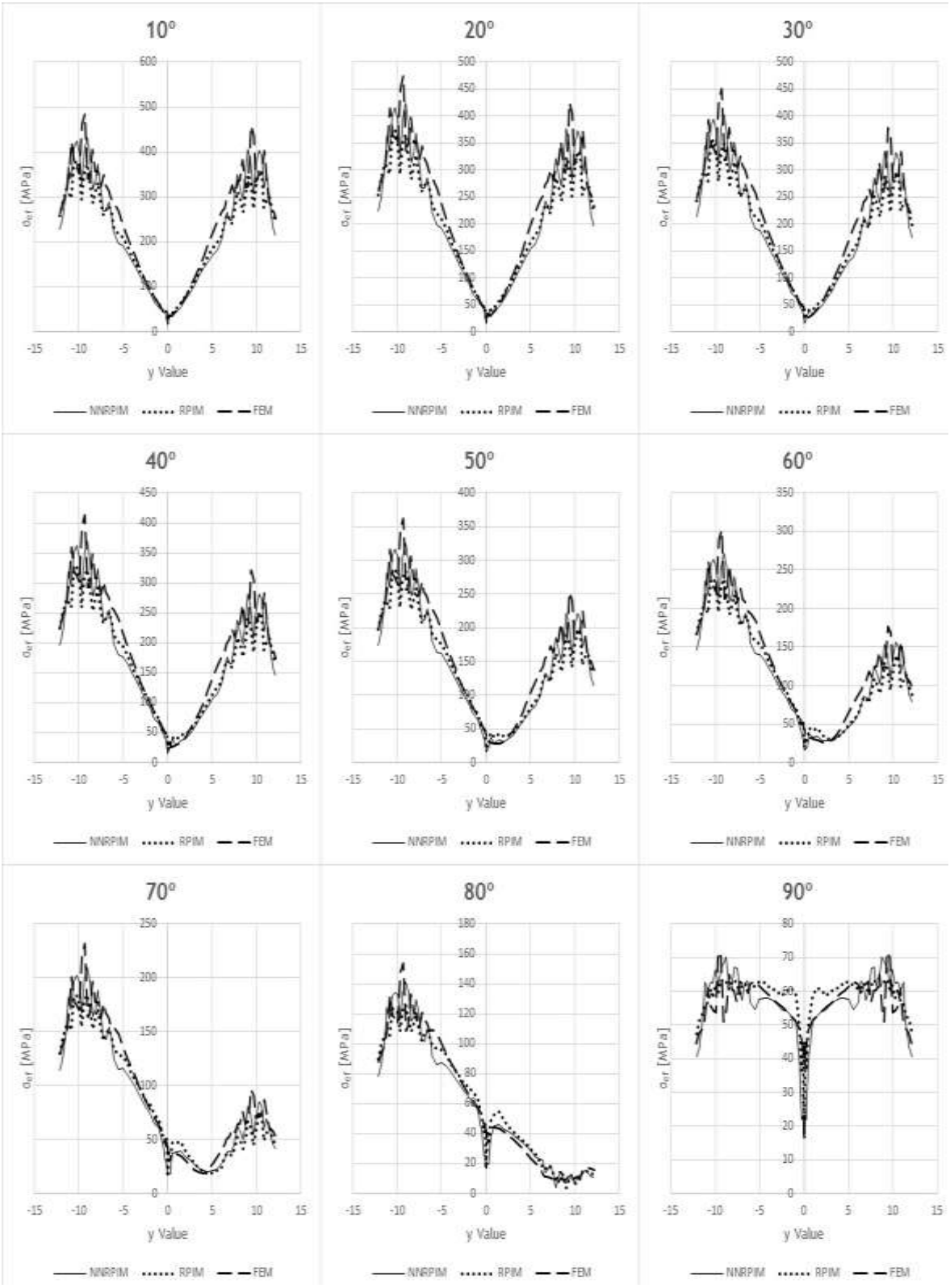

Figure A.25 Stress distribution from implant side, from 'Model 1', from bone type 5

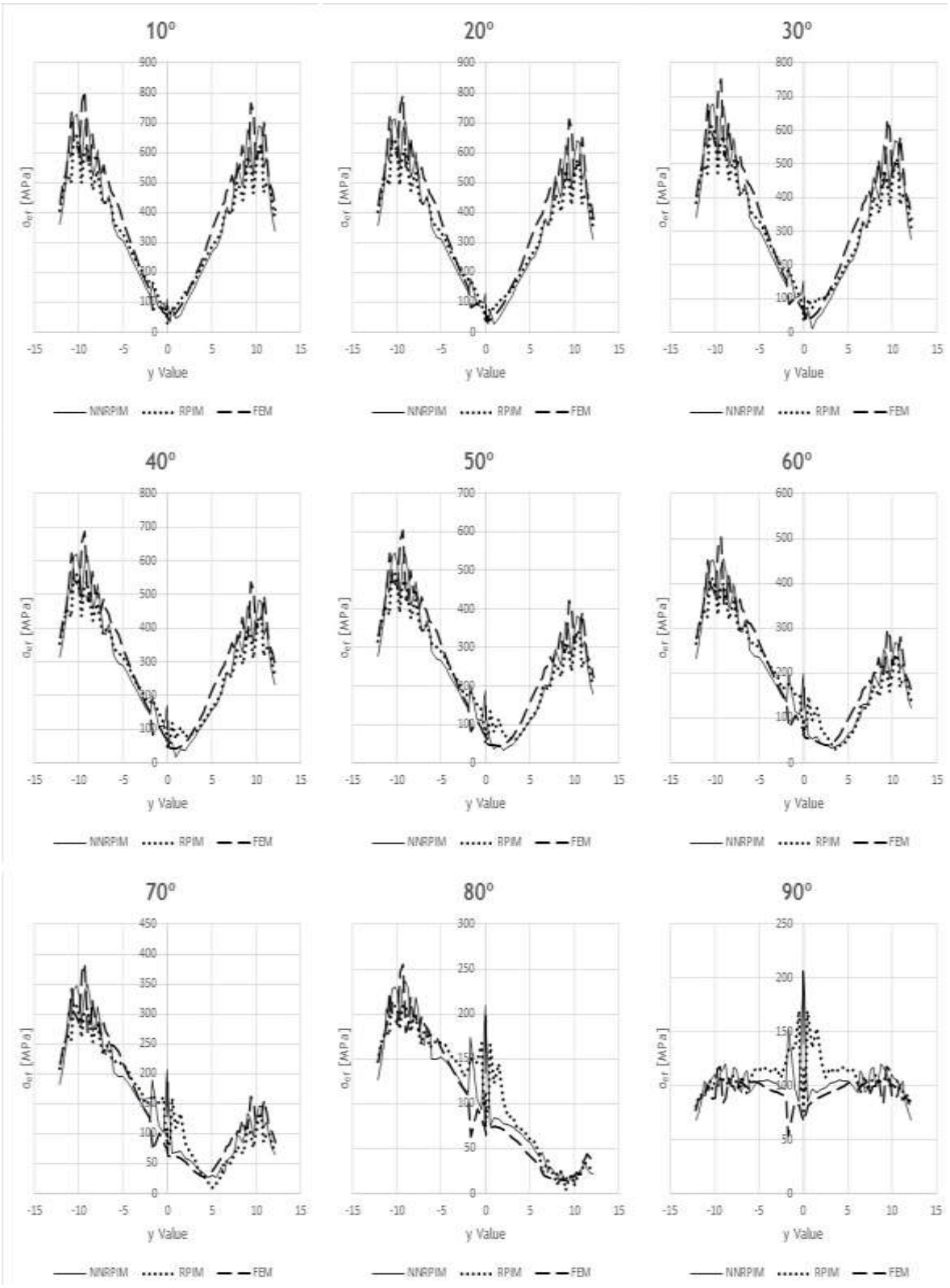

Figure A.26 Stress distribution from implant side, from 'Model 2', from bone type 1

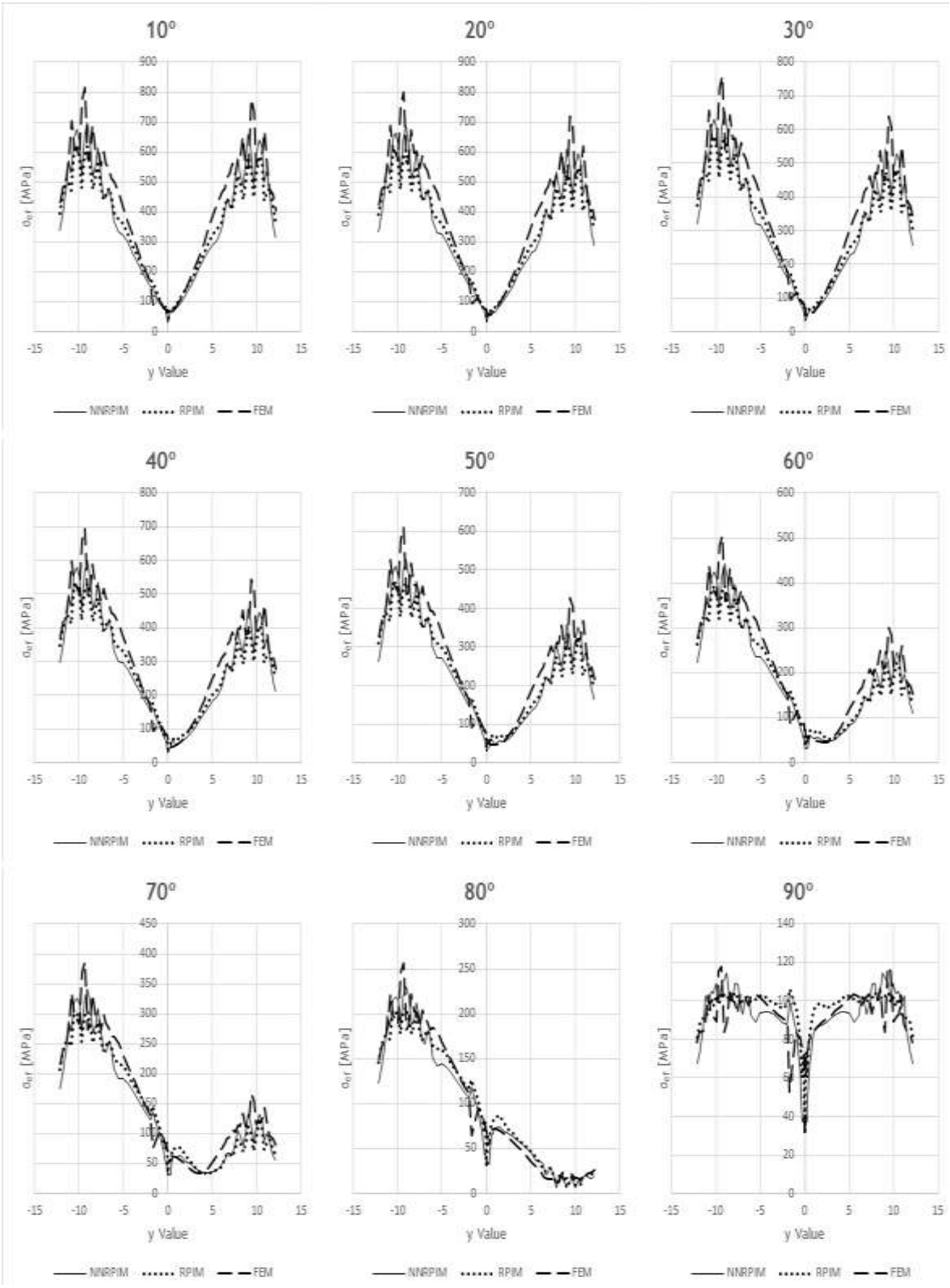

Figure A.27 Stress distribution from implant side, from 'Model 2', from bone type 2

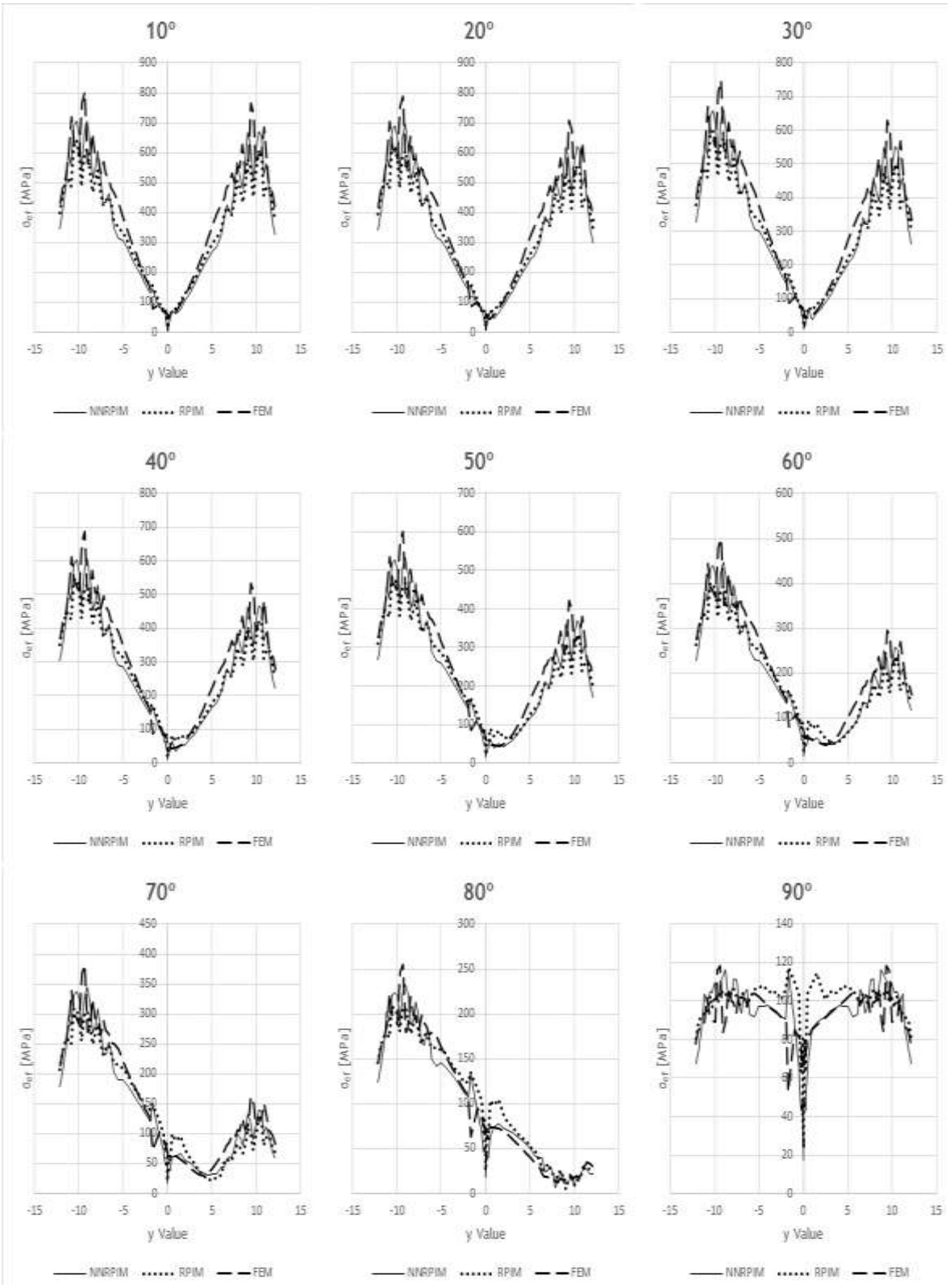

Figure A.28 Stress distribution from implant side, from 'Model 2', from bone type 3

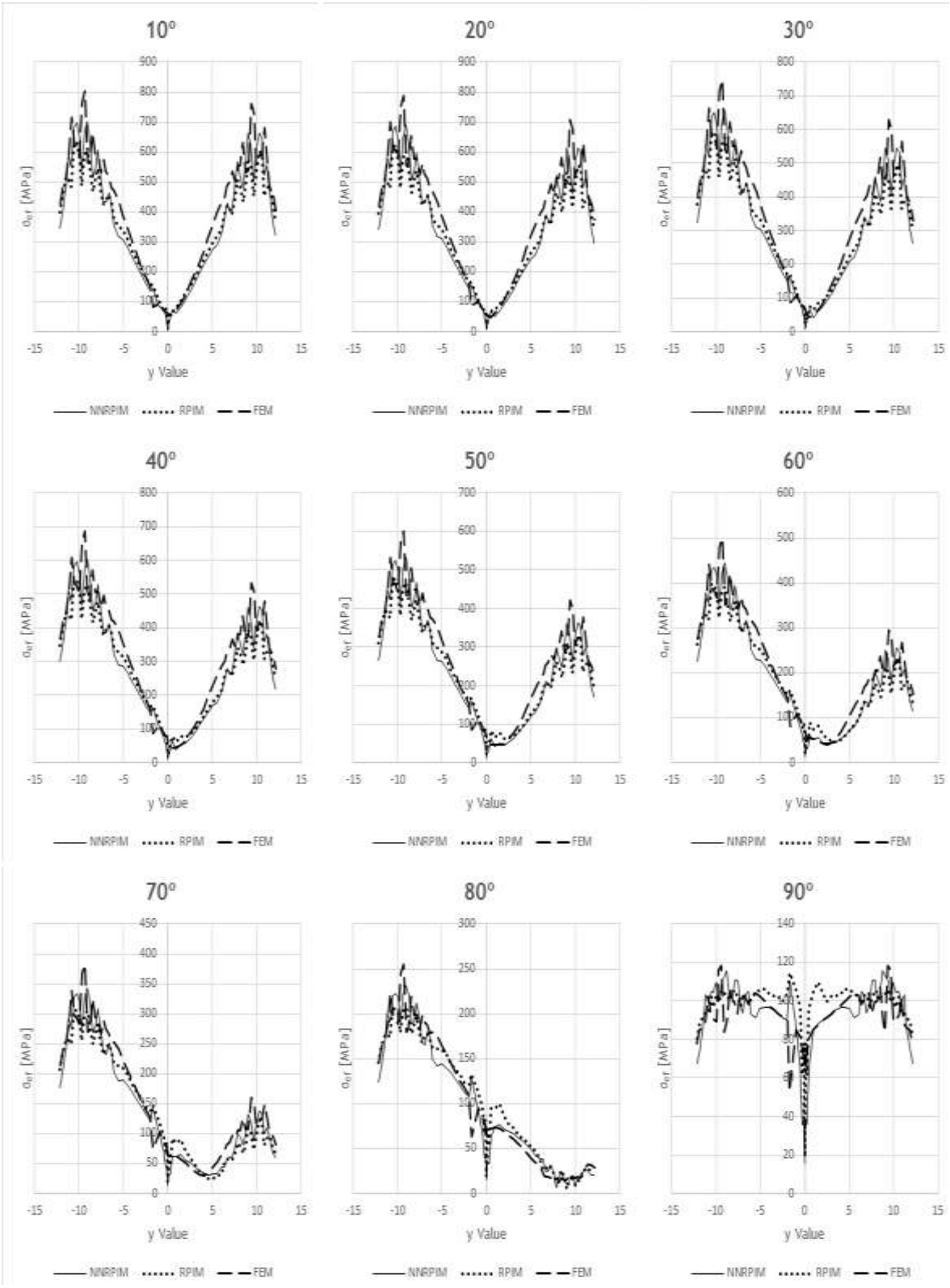

Figure A.29 Stress distribution from implant side, from 'Model 2', from bone type 4

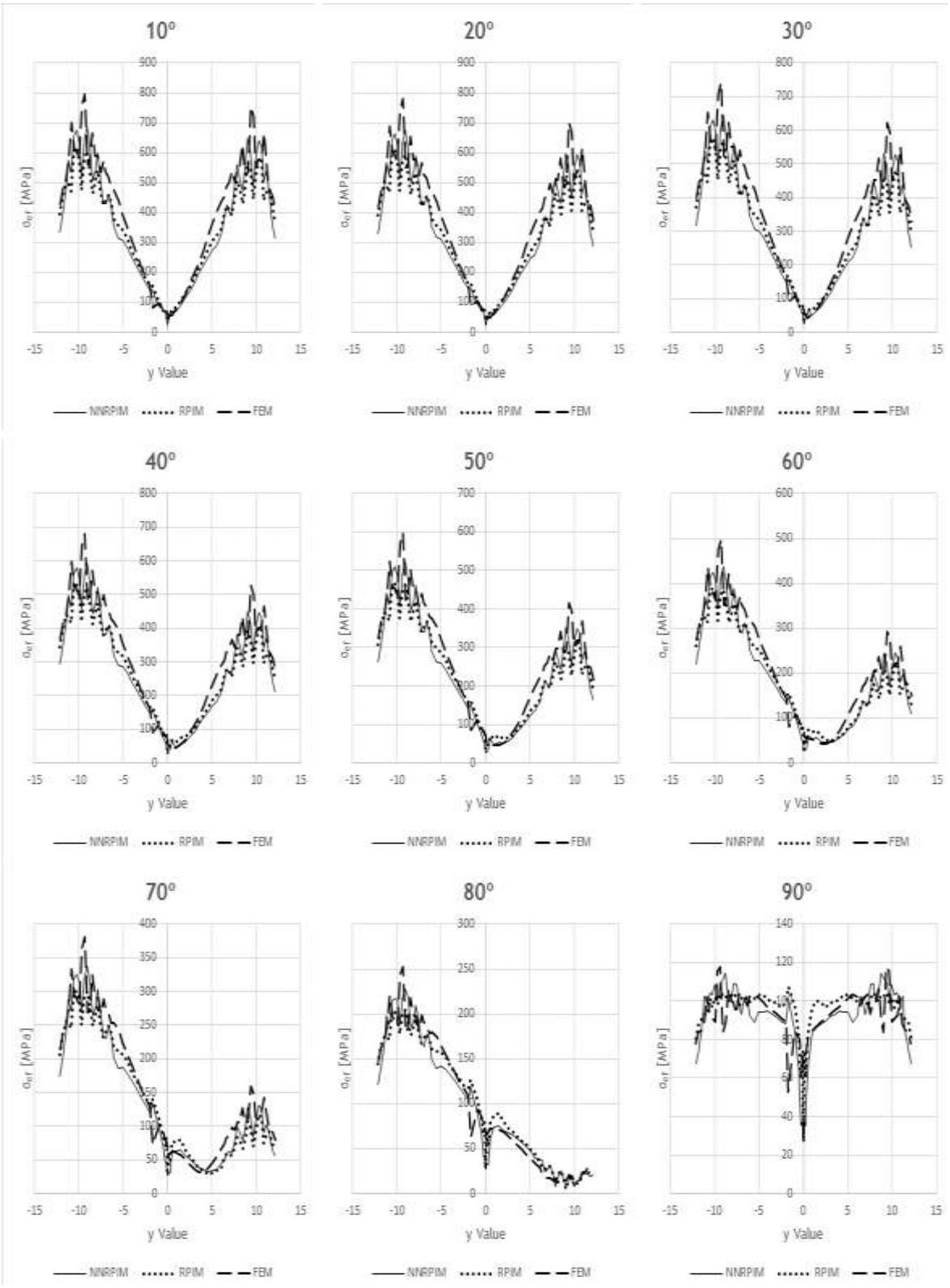

Figure A.30 Stress distribution from implant side, from 'Model 2', from bone type 5

Appendix 3

In this appendix are presented all the tables with the specified values of the points acquired and that are identified in section 6.1 of this work. The dotted line in each table helps to separate the points that correspond to the bone side (first 9) and the ones that corresponds to the implant side.

Table A.1 Stress Values for specific points, for type of bone 1 at 10º

Points	FEM		RPIM		NNRPIM	
	M1	M2	M1	M2	M1	M2
1	203.346	334.016	133.980	188.487	121.317	158.992
2	170.691	280.490	117.591	193.656	108.414	182.463
3	2.693	4.437	82.621	146.296	18.064	34.127
4	17.632	29.009	17.206	28.195	12.322	20.007
5	14.844	24.424	4.602	7.547	9.692	15.765
6	15.173	24.964	13.790	22.620	10.251	16.664
7	2.655	4.377	81.242	143.283	18.116	33.937
8	173.147	284.589	118.263	194.699	109.418	183.528
9	199.446	327.669	131.671	185.920	119.145	157.105
10	269.316	434.560	260.001	407.439	232.401	360.455
11	296.538	496.288	289.178	465.666	259.673	412.683
12	368.712	612.971	325.452	526.610	386.687	615.872
13	40.559	66.731	42.666	69.892	61.324	99.643
14	31.226	51.376	23.037	37.840	60.504	98.355
15	29.730	48.914	42.067	69.094	51.283	83.243
16	352.282	584.571	307.181	496.168	365.782	581.529
17	281.364	469.186	271.964	435.813	245.042	387.577
18	255.297	409.954	244.708	381.302	219.186	338.150

Table A.2 Stress Values for specific points, for type of bone 1 at 20º

Points	FEM		RPIM		NNRPIM	
	M1	M2	M1	M2	M1	M2
1	196.037	321.980	129.023	181.170	116.873	152.683
2	161.656	265.611	111.873	184.263	102.947	173.571
3	2.620	4.315	79.569	141.168	17.221	32.672
4	19.285	31.730	19.978	32.755	13.857	22.517
5	17.333	28.519	5.204	8.543	11.495	18.730
6	14.842	24.419	14.146	23.246	10.206	16.629
7	2.546	4.197	76.852	135.235	17.323	32.298
8	166.493	273.684	113.198	186.318	104.924	175.669
9	188.355	309.477	124.475	176.113	112.593	148.966
10	264.148	427.253	255.902	402.153	228.498	355.338
11	290.742	487.460	284.721	459.583	255.244	406.594
12	360.221	599.394	319.901	518.062	379.659	605.198
13	45.651	75.108	51.264	84.029	64.909	105.540
14	32.150	52.897	30.348	49.887	66.803	108.721
15	25.556	42.047	50.325	82.778	45.690	74.167
16	327.857	543.451	283.915	458.104	338.482	537.552
17	260.859	434.083	250.814	400.783	226.425	357.141
18	236.535	378.793	225.779	350.675	202.467	311.404

Table A.3 Stress Values for specific points, for type of bone 1 at 30º

Points	FEM		RPIM		NNRPIM	
	M1	M2	M1	M2	M1	M2
1	182.778	300.173	120.145	168.346	108.877	141.736
2	147.725	242.686	102.759	169.267	94.353	159.400
3	2.489	4.097	74.117	131.776	15.861	30.230
4	20.914	34.410	22.810	37.421	15.406	25.057
5	20.570	33.845	6.012	9.876	13.808	22.528
6	15.267	25.119	15.879	26.130	10.908	17.814
7	2.383	3.929	70.149	123.106	16.010	29.684
8	154.793	254.485	104.696	172.271	97.242	162.467
9	171.550	281.899	113.497	160.954	102.621	136.303
10	250.973	407.011	244.042	384.693	217.660	339.448
11	276.153	463.889	271.628	439.567	243.069	388.170
12	340.802	567.623	304.665	493.820	361.120	576.165
13	49.918	82.130	62.030	101.764	67.180	109.314
14	33.516	55.143	38.973	64.092	75.439	122.916
15	23.749	39.074	60.984	100.374	40.612	65.979
16	293.500	485.856	252.081	406.204	300.942	477.300
17	232.489	385.901	222.072	353.636	200.947	315.893
18	210.619	336.199	200.019	309.475	179.613	275.242

Table A.4 Stress Values for specific points, for type of bone 1 at40º

Points	FEM		RPIM		NNRPIM	
	M1	M2	M1	M2	M1	M2
1	163.989	269.284	107.624	150.420	97.583	126.497
2	129.338	212.442	90.533	149.136	82.901	140.394
3	2.308	3.798	66.443	118.420	14.029	26.882
4	22.348	36.769	25.395	41.685	16.804	27.355
5	23.951	39.407	6.874	11.299	16.200	26.453
6	16.343	26.890	18.439	30.360	12.156	19.880
7	2.177	3.589	61.349	107.287	14.221	26.181
8	138.420	227.601	93.022	152.997	86.614	144.337
9	149.560	245.801	99.079	140.918	89.541	119.515
10	230.212	374.486	224.803	355.624	200.233	313.296
11	253.239	426.336	250.318	406.263	223.537	358.001
12	311.073	518.670	280.233	454.666	331.664	529.702
13	53.100	87.365	73.023	119.887	68.007	110.745
14	35.119	57.781	47.460	78.064	84.842	138.355
15	25.047	41.211	72.015	118.546	36.991	60.219
16	250.295	413.601	212.696	342.124	254.351	402.678
17	197.167	326.190	186.650	295.872	169.414	265.139
18	178.370	283.537	168.245	259.024	151.345	230.814

Table A.5 Stress Values for specific points, for type of bone 1 at 50º

Points	FEM		RPIM		NNRPIM	
	M1	M2	M1	M2	M1	M2
1	140.261	230.285	91.852	127.950	83.342	107.445
2	107.082	175.841	75.580	124.497	68.950	117.144
3	2.089	3.436	56.796	101.530	11.788	22.735
4	23.463	38.604	27.530	45.212	17.933	29.220
5	27.088	44.567	7.685	12.637	18.406	30.070
6	17.838	29.348	21.283	35.045	13.675	22.376
7	1.944	3.205	50.742	88.293	12.015	21.901
8	117.891	193.884	78.545	129.098	73.373	121.841
9	123.081	202.324	81.672	116.633	73.764	99.129
10	202.521	330.709	198.790	315.869	176.766	277.708
11	222.732	376.000	221.463	360.721	197.262	317.039
12	271.970	454.073	247.382	401.838	292.219	467.274
13	55.024	90.530	83.079	136.472	67.342	109.752
14	36.747	60.460	55.068	90.589	93.814	153.077
15	28.903	47.554	82.194	135.296	35.754	58.372
16	199.623	328.982	167.054	267.958	200.214	316.085
17	156.059	256.931	145.688	229.370	132.832	206.512
18	140.830	222.536	131.481	200.995	118.566	179.561

Table A.6 Stress Values for specific points, for type of bone 1 at 60º

Points	FEM		RPIM		NNRPIM	
	M1	M2	M1	M2	M1	M2
1	112.305	184.346	73.294	101.604	66.577	85.146
2	81.644	134.016	58.348	96.078	52.917	90.335
3	1.851	3.043	45.482	81.633	9.212	17.920
4	24.177	39.779	29.082	47.782	18.719	30.523
5	29.737	48.926	8.377	13.778	20.263	33.113
6	19.499	32.082	24.033	39.567	15.233	24.923
7	1.706	2.812	38.680	66.740	9.466	16.983
8	93.831	154.358	61.695	101.276	57.911	95.643
9	92.918	152.794	61.796	88.821	55.761	75.758
10	168.733	277.008	166.783	266.634	147.956	233.750
11	185.564	314.418	185.926	304.307	165.027	266.505
12	224.665	375.759	207.108	336.932	243.971	390.746
13	55.597	91.473	91.483	150.344	65.223	106.389
14	38.215	62.876	61.368	100.959	101.530	165.731
15	34.105	56.114	90.778	149.407	37.285	61.011
16	143.076	234.639	116.696	186.189	140.285	220.299
17	110.566	180.515	100.514	156.340	92.364	141.908
18	99.216	155.257	90.926	137.404	82.315	123.176

Table A.7 Stress Values for specific points, for type of bone 1 at 70º

Points	FEM		RPIM		NNRPIM	
	M1	M2	M1	M2	M1	M2
1	81.030	132.962	52.538	72.217	47.823	60.322
2	53.929	88.450	39.400	64.773	35.323	60.811
3	1.620	2.661	32.917	59.427	6.412	12.617
4	24.442	40.213	29.964	49.251	19.111	31.186
5	31.734	52.211	8.901	14.642	21.660	35.401
6	21.113	34.737	26.435	43.510	16.655	27.241
7	1.497	2.465	25.664	43.492	6.681	11.615
8	67.048	110.351	43.019	70.406	40.726	66.564
9	60.108	98.913	40.091	58.383	36.124	50.174
10	129.943	215.145	129.811	209.529	114.723	182.841
11	142.975	243.641	144.847	238.839	127.861	208.019
12	170.682	286.232	160.733	262.065	188.479	302.576
13	54.791	90.148	97.756	160.709	61.774	100.856
14	39.373	64.779	66.062	108.685	107.413	175.376
15	39.639	65.217	97.267	160.059	41.115	67.334
16	82.846	134.146	64.080	100.744	77.157	119.374
17	62.912	100.857	53.124	80.339	49.670	74.180
18	55.318	85.007	48.389	71.756	44.077	64.327

Table A.8 Stress Values for specific points, for type of bone 1 at 80º

Points	FEM		RPIM		NNRPIM	
	M1	M2	M1	M2	M1	M2
1	47.574	78.005	30.273	40.786	27.718	33.860
2	25.444	41.629	19.483	31.639	16.855	29.564
3	1.433	2.354	19.731	35.908	3.603	7.111
4	24.237	39.877	30.129	49.540	19.087	31.166
5	32.971	54.247	9.227	15.179	22.524	36.817
6	22.511	37.038	28.318	46.593	17.820	29.133
7	1.360	2.237	12.779	20.419	3.854	6.136
8	38.623	63.633	23.200	37.497	22.420	35.550
9	26.315	43.416	17.412	26.503	15.680	23.453
10	87.495	147.318	89.124	146.557	78.167	126.703
11	96.542	166.271	99.604	166.526	86.999	143.527
12	111.875	188.501	109.906	179.849	127.645	205.732
13	52.642	86.612	101.581	167.047	57.215	93.502
14	40.109	65.990	68.952	113.441	111.081	181.389
15	44.834	73.764	101.331	166.714	46.290	75.785
16	25.878	39.016	22.812	34.793	23.718	34.697
17	23.485	38.462	16.167	28.619	13.579	22.545
18	17.345	30.388	14.986	29.385	11.921	21.701

Table A.9 Stress Values for specific points, for type of bone 1 at 90º

Points	FEM		RPIM		NNRPIM	
	M1	M2	M1	M2	M1	M2
1	14.979	24.536	7.970	9.845	7.726	8.623
2	12.487	20.577	5.255	5.735	5.052	5.404
3	1.336	2.195	8.359	14.426	1.967	2.895
4	23.579	38.795	29.571	48.640	18.648	30.469
5	33.390	54.937	9.338	15.362	22.817	37.296
6	23.579	38.795	29.571	48.640	18.648	30.469
7	1.336	2.195	8.359	14.426	1.967	2.895
8	12.487	20.577	5.255	5.735	5.052	5.404
9	14.979	24.536	7.970	9.845	7.726	8.623
10	43.561	77.155	46.590	80.847	39.874	67.900
11	49.141	86.893	52.226	90.610	44.236	75.849
12	51.325	87.276	57.362	94.456	64.460	104.681
13	49.263	81.052	102.792	169.081	51.890	84.884
14	40.362	66.407	69.928	115.048	112.328	183.433
15	49.263	81.052	102.792	169.081	51.890	84.884
16	51.325	87.276	57.362	94.456	64.460	104.681
17	49.141	86.893	52.226	90.610	44.236	75.849
18	43.561	77.155	46.590	80.847	39.874	67.900

Table A.10 Stress Values for specific points, for type of bone 2 at 10º

Points	FEM		RPIM		NNRPIM	
	M1	M2	M1	M2	M1	M2
1	163.310	268.243	115.947	163.355	106.762	138.473
2	126.659	207.886	89.213	139.595	81.922	126.919
3	16.867	27.725	67.221	116.979	19.207	35.455
4	21.368	35.158	16.920	27.579	14.923	24.017
5	18.502	30.443	11.545	18.851	15.975	25.784
6	19.000	31.262	14.069	22.965	12.595	20.314
7	16.475	27.087	65.234	113.253	18.958	34.970
8	126.257	207.287	88.813	139.371	81.713	126.978
9	160.854	264.260	114.208	161.062	105.114	136.534
10	268.985	431.163	259.922	396.758	228.824	337.818
11	291.467	485.256	288.901	458.021	253.885	392.071
12	345.175	572.971	313.182	497.598	370.751	573.473
13	48.851	80.378	47.165	76.939	49.143	79.175
14	38.520	63.380	30.554	49.797	18.875	30.360
15	38.216	62.881	44.425	72.521	47.020	75.781
16	327.651	542.852	294.271	466.096	349.514	538.505
17	275.739	457.311	271.569	427.951	239.275	366.922
18	254.179	405.391	243.936	369.867	215.115	315.199

Table A.11 Stress Values for specific points, for type of bone 2 at 20º

Points	FEM		RPIM		NNRPIM	
	M1	M2	M1	M2	M1	M2
1	157.087	257.996	111.524	157.053	102.715	133.133
2	121.081	198.702	85.343	133.329	78.287	121.086
3	16.310	26.807	65.172	113.546	18.467	34.096
4	22.599	37.183	18.626	30.381	16.287	26.241
5	20.262	33.339	12.214	19.971	17.034	27.563
6	18.194	29.936	13.447	22.013	12.034	19.494
7	15.539	25.551	61.258	106.206	17.978	33.141
8	120.290	197.520	84.553	132.888	77.875	121.201
9	152.249	250.150	108.100	152.535	99.469	129.314
10	264.222	424.580	256.165	392.314	225.328	333.881
11	286.139	477.281	284.496	452.359	249.697	386.920
12	338.286	562.051	308.471	490.849	364.579	565.004
13	53.226	87.576	48.526	79.193	49.299	79.477
14	38.655	63.602	29.694	48.411	18.918	30.473
15	33.052	54.384	43.393	70.924	45.241	72.994
16	303.764	502.718	271.220	428.794	322.746	496.120
17	255.157	422.234	250.353	393.126	220.917	337.380
18	235.058	373.818	224.676	339.348	198.323	289.327

Table A.12 Stress Values for specific points, for type of bone 2 at 30º

Points	FEM		RPIM		NNRPIM	
	M1	M2	M1	M2	M1	M2
1	146.089	239.907	103.710	145.980	95.546	123.755
2	111.833	183.493	78.884	123.014	72.277	111.575
3	15.269	25.094	61.153	106.679	17.176	31.712
4	23.672	38.948	20.226	33.025	17.556	28.333
5	22.695	37.341	13.173	21.573	18.540	30.084
6	17.840	29.353	13.612	22.360	12.079	19.673
7	14.145	23.261	55.434	95.955	16.462	30.319
8	110.676	181.766	77.730	122.370	71.676	111.743
9	139.016	228.438	98.705	139.377	90.801	118.172
10	251.441	405.125	244.631	375.976	214.987	319.812
11	272.124	454.817	271.447	432.957	237.921	370.015
12	321.112	534.040	294.389	469.189	347.327	539.362
13	56.527	93.006	49.667	81.121	48.814	78.782
14	38.860	63.939	28.325	46.204	18.982	30.643
15	29.158	47.976	42.792	70.058	43.196	69.820
16	270.647	447.304	239.940	378.482	286.175	438.667
17	226.839	374.359	221.541	346.377	195.852	297.601
18	208.817	330.940	198.605	298.572	175.514	254.695

Table A.13 Stress Values for specific points, for type of bone 2 at 40º

Points	FEM		RPIM		NNRPIM	
	M1	M2	M1	M2	M1	M2
1	130.663	214.546	92.751	130.487	85.481	110.633
2	99.206	162.743	70.040	108.977	64.083	98.684
3	13.779	22.643	55.294	96.599	15.377	28.383
4	24.487	40.289	21.571	35.263	18.611	30.094
5	25.363	41.730	14.261	23.390	20.235	32.915
6	18.008	29.631	14.519	23.912	12.720	20.805
7	12.340	20.296	47.951	82.828	14.461	26.596
8	97.720	160.524	68.557	108.149	63.310	98.900
9	121.571	199.804	86.317	122.001	79.381	103.459
10	231.052	373.424	225.688	348.270	198.132	296.064
11	249.869	418.582	250.172	400.435	218.934	341.896
12	294.200	489.828	271.388	433.308	319.542	497.363
13	58.564	96.358	50.472	82.524	47.731	77.155
14	39.111	64.350	26.549	43.345	19.061	30.852
15	27.624	45.451	42.715	70.060	41.115	66.622
16	229.335	378.337	201.412	316.734	240.944	367.942
17	191.677	315.194	186.033	289.171	164.866	248.832
18	176.285	278.120	166.544	248.834	147.405	212.399

Table A.14 Stress Values for specific points, for type of bone 2 at 50º

Points	FEM		RPIM		NNRPIM	
	M1	M2	M1	M2	M1	M2
1	111.289	182.704	78.988	111.059	72.833	94.183
2	83.602	137.107	59.091	91.658	53.964	82.818
3	11.892	19.540	47.783	83.630	13.130	24.219
4	24.974	41.090	22.556	36.917	19.367	31.380
5	27.922	45.940	15.334	25.179	21.894	35.680
6	18.665	30.711	15.946	26.291	13.803	22.626
7	10.190	16.764	39.052	67.252	12.044	22.097
8	81.832	134.466	57.326	90.672	53.043	83.074
9	100.459	165.144	71.323	100.952	65.567	85.642
10	203.696	330.475	199.931	310.072	175.291	263.384
11	220.073	369.714	221.335	355.814	193.329	303.442
12	258.388	430.791	240.186	384.330	282.093	440.320
13	59.230	97.453	50.861	83.262	46.145	74.738
14	39.375	64.786	24.521	40.081	19.145	31.072
15	29.008	47.727	43.174	70.927	39.263	63.808
16	181.123	297.975	156.859	245.509	188.477	286.170
17	150.790	246.627	144.953	223.328	128.937	192.618
18	138.505	217.071	129.515	191.758	114.886	163.800

Table A.15 Stress Values for specific points, for type of bone 2 at 60º

Points	FEM		RPIM		NNRPIM	
	M1	M2	M1	M2	M1	M2
1	88.541	145.324	62.827	88.276	57.977	74.899
2	65.493	107.367	46.368	71.576	42.225	64.449
3	9.676	15.895	38.854	68.169	10.512	19.356
4	25.095	41.288	23.115	37.878	19.773	32.102
5	30.130	49.574	16.278	26.752	23.347	38.097
6	19.689	32.395	17.621	29.052	15.122	24.795
7	7.782	12.808	29.032	49.740	9.299	16.977
8	63.498	104.388	44.377	70.463	41.186	64.738
9	76.308	125.489	54.167	76.865	49.770	65.262
10	170.189	277.570	168.125	262.525	147.141	222.746
11	183.621	309.666	185.790	300.414	161.863	255.791
12	214.733	358.667	201.707	323.703	236.084	369.915
13	58.490	96.235	50.797	83.264	44.204	71.760
14	39.623	65.193	22.447	36.748	19.224	31.278
15	32.802	53.970	44.098	72.529	37.909	61.788
16	127.464	208.623	107.665	167.016	130.368	195.845
17	105.457	170.818	99.571	150.911	89.168	130.707
18	96.677	149.799	88.687	129.254	78.969	110.480

Table A.16 Stress Values for specific points, for type of bone 2 at 70º

Points	FEM		RPIM		NNRPIM	
	M1	M2	M1	M2	M1	M2
1	63.140	103.592	44.777	62.871	41.383	53.415
2	45.493	74.528	32.296	49.390	29.259	44.172
3	7.227	11.870	28.814	50.747	7.636	13.985
4	24.840	40.869	23.212	38.081	19.801	32.212
5	31.818	52.351	17.010	27.969	24.468	39.961
6	20.913	34.408	19.305	31.808	16.481	27.001
7	5.263	8.668	18.314	31.023	6.362	11.465
8	43.342	71.319	30.148	48.187	28.139	44.485
9	49.899	82.125	35.397	50.539	32.500	43.020
10	131.605	216.414	131.277	207.157	114.568	175.444
11	141.674	240.347	144.655	235.980	125.524	200.442
12	164.599	275.703	157.166	253.335	182.956	288.350
13	56.383	92.767	50.286	82.531	42.111	68.533
14	39.824	65.524	20.603	33.790	19.288	31.445
15	37.927	62.401	45.353	74.633	37.278	60.896
16	70.201	113.297	55.742	84.322	68.701	100.256
17	57.453	90.834	51.614	74.876	47.032	65.536
18	52.529	79.413	45.740	64.508	41.052	54.903

Table A.17 Stress Values for specific points, for type of bone 2 at 80º

Points	FEM		RPIM		NNRPIM	
	M1	M2	M1	M2	M1	M2
1	35.936	58.911	25.427	35.747	23.607	30.546
2	24.450	39.994	17.446	25.953	15.603	22.738
3	4.718	7.748	18.087	32.069	4.700	8.425
4	24.228	39.863	22.840	37.514	19.449	31.701
5	32.872	54.085	17.470	28.735	25.172	41.130
6	22.168	36.473	20.816	34.265	17.725	28.996
7	3.035	5.004	7.994	13.057	3.550	6.071
8	22.275	36.749	15.264	24.721	14.465	23.060
9	22.253	36.737	15.700	23.105	14.427	19.994
10	89.235	149.088	90.587	145.824	78.623	123.030
11	95.613	164.035	99.245	164.577	85.474	139.160
12	109.573	184.494	107.993	175.470	124.390	198.197
13	53.017	87.230	49.376	81.129	40.113	65.435
14	39.954	65.737	19.304	31.710	19.329	31.553
15	43.415	71.431	46.765	76.951	37.482	61.285
16	14.677	20.759	13.236	20.772	13.314	19.964
17	14.848	23.808	11.637	21.086	10.037	16.662
18	14.734	25.833	12.297	25.487	9.779	19.128

Table A.18 Stress Values for specific points, for type of bone 2 at 90º

Points	FEM		RPIM		NNRPIM	
	M1	M2	M1	M2	M1	M2
1	8.910	14.618	6.008	9.541	5.920	9.022
2	7.188	11.845	4.815	6.243	4.349	4.935
3	2.707	4.450	7.816	13.913	2.495	3.985
4	23.311	38.354	22.024	36.214	18.741	30.604
5	33.231	54.675	17.628	28.997	25.413	41.529
6	23.311	38.354	22.024	36.214	18.741	30.604
7	2.707	4.450	7.816	13.913	2.495	3.985
8	7.188	11.845	4.815	6.243	4.349	4.935
9	8.910	14.618	6.008	9.541	5.920	9.022
10	45.000	78.729	47.698	81.184	40.715	67.652
11	47.433	83.955	51.300	88.916	43.248	74.249
12	51.719	88.304	56.101	93.045	62.555	102.729
13	48.596	79.955	48.160	79.203	38.486	62.890
14	40.000	65.812	18.832	30.956	19.344	31.591
15	48.596	79.955	48.160	79.203	38.486	62.890
16	51.719	88.304	56.101	93.045	62.555	102.729
17	47.433	83.955	51.300	88.916	43.248	74.249
18	45.000	78.729	47.698	81.184	40.715	67.652

Table A.19 Stress Values for specific points, for type of bone 3 at 10º

Points	FEM		RPIM		NNRPIM	
	M1	M2	M1	M2	M1	M2
1	192.236	315.622	131.282	187.167	119.508	158.629
2	155.527	255.351	107.873	175.316	99.694	164.797
3	6.358	10.469	75.374	132.795	18.041	34.128
4	18.655	30.694	15.182	24.835	12.953	20.969
5	15.857	26.091	8.006	13.115	12.663	20.548
6	16.226	26.698	12.304	20.157	10.691	17.337
7	6.226	10.255	73.758	129.527	18.000	33.851
8	156.656	257.285	108.128	175.937	100.217	165.522
9	188.997	310.374	129.078	184.481	117.477	156.552
10	266.977	429.841	259.340	400.601	229.960	347.271
11	292.778	489.239	288.478	461.171	255.853	401.183
12	359.088	596.726	318.888	512.925	378.803	597.653
13	42.861	70.519	40.702	66.609	48.876	79.191
14	33.259	54.721	9.916	16.195	5.500	8.964
15	32.086	52.792	40.626	66.596	45.886	74.347
16	342.159	567.529	300.359	482.065	357.818	563.137
17	277.444	461.896	271.234	431.299	241.261	376.162
18	252.737	404.934	243.798	374.332	216.575	325.022

Table A.20 Stress Values for specific points, for type of bone 3 at 20º

Points	FEM		RPIM		NNRPIM	
	M1	M2	M1	M2	M1	M2
1	185.093	303.859	126.395	179.973	115.074	152.436
2	147.857	242.715	102.816	166.982	94.873	156.888
3	6.157	10.135	72.767	128.409	17.246	32.720
4	20.186	33.211	17.276	28.276	14.483	23.466
5	18.126	29.823	8.812	14.451	14.159	23.021
6	15.754	25.920	12.238	20.096	10.449	17.003
7	5.898	9.716	69.586	121.974	17.167	32.174
8	150.080	246.526	103.317	168.205	95.902	158.316
9	178.712	293.521	122.054	174.681	111.073	148.343
10	262.027	422.899	255.393	395.686	226.253	342.726
11	287.216	480.821	284.062	455.291	251.577	395.572
12	351.277	584.276	313.750	505.190	372.159	587.880
13	47.747	78.559	43.243	70.784	49.544	80.314
14	33.947	55.853	10.810	17.685	7.324	11.939
15	27.601	45.413	43.108	70.762	43.840	71.080
16	317.929	526.762	277.254	444.405	330.823	519.891
17	257.015	426.968	250.094	396.453	222.832	346.287
18	233.979	373.845	224.779	343.947	199.887	298.905

Table A.21 Stress Values for specific points, for type of bone 3 at 30º

Points	FEM		RPIM		NNRPIM	
	M1	M2	M1	M2	M1	M2
1	172.327	282.866	117.666	167.311	107.143	141.615
2	135.706	222.726	94.639	153.574	87.173	144.209
3	5.784	9.521	67.965	120.141	15.936	30.325
4	21.657	35.633	19.367	31.723	15.983	25.927
5	21.135	34.773	9.921	16.286	16.185	26.363
6	15.951	26.245	13.220	21.754	10.952	17.884
7	5.409	8.912	63.316	110.739	15.819	29.528
8	138.955	228.294	95.372	155.361	88.677	146.298
9	163.000	267.756	111.320	159.576	101.294	135.633
10	249.135	403.152	243.697	378.789	215.677	327.791
11	272.953	457.839	271.025	435.602	239.663	377.958
12	332.799	554.078	299.100	482.135	354.220	560.262
13	51.744	85.134	46.845	76.736	49.564	80.411
14	34.973	57.542	12.052	19.751	9.459	15.420
15	25.144	41.370	46.678	76.708	41.700	67.693
16	284.056	470.008	245.764	393.300	293.804	460.887
17	228.819	379.142	221.379	349.610	197.650	305.926
18	208.144	331.470	198.954	303.186	177.141	263.749

Table A.22 Stress Values for specific points, for type of bone 3 at 40º

Points	FEM		RPIM		NNRPIM	
	M1	M2	M1	M2	M1	M2
1	154.343	253.307	105.369	149.580	95.964	126.508
2	119.460	196.014	83.599	135.512	76.835	127.158
3	5.257	8.650	61.120	108.258	14.152	27.023
4	22.921	37.712	21.240	34.819	17.302	28.104
5	24.322	40.018	11.132	18.288	18.368	29.959
6	16.774	27.599	14.945	24.619	12.053	19.726
7	4.781	7.878	55.152	96.183	14.003	25.999
8	123.635	203.169	84.542	137.809	78.769	129.842
9	142.355	233.887	97.212	139.638	88.446	118.822
10	228.711	371.234	224.628	350.456	198.571	302.945
11	250.446	421.031	249.784	402.735	220.493	348.906
12	304.243	507.091	275.409	444.500	325.559	515.679
13	54.609	89.848	50.904	83.459	48.938	79.477
14	36.194	59.550	13.419	22.022	11.551	18.832
15	25.620	42.154	50.729	83.429	39.734	64.612
16	241.604	399.047	206.889	330.371	247.927	387.984
17	193.756	319.946	185.994	292.256	166.507	256.354
18	176.052	279.166	167.141	253.355	149.052	220.674

Table A.23 Stress Values for specific points, for type of bone 3 at 50º

Points	FEM		RPIM		NNRPIM	
	M1	M2	M1	M2	M1	M2
1	131.702	216.107	89.888	127.335	81.888	107.591
2	99.634	163.430	70.046	113.361	64.186	106.266
3	4.597	7.562	52.455	93.138	11.956	22.920
4	23.868	39.269	22.748	37.317	18.336	29.819
5	27.307	44.929	12.289	20.201	20.435	33.360
6	18.046	29.691	17.019	28.041	13.495	22.102
7	4.044	6.665	45.362	78.779	11.780	21.704
8	104.603	171.946	71.168	116.097	66.488	109.463
9	117.426	192.979	80.171	115.494	72.933	98.437
10	201.402	328.159	198.786	311.584	175.472	268.974
11	220.410	371.563	221.008	357.727	194.669	309.329
12	266.503	444.786	243.424	393.472	287.077	455.533
13	56.187	92.445	54.882	90.058	47.717	77.592
14	37.448	61.614	14.735	24.204	13.423	21.885
15	28.832	47.438	54.719	90.030	38.222	62.278
16	191.918	316.121	161.891	257.652	194.659	303.508
17	152.966	251.312	145.073	226.243	130.397	199.165
18	138.738	218.648	130.361	196.097	116.518	171.080

Table A.24 Stress Values for specific points, for type of bone 3 at 60º

Points	FEM		RPIM		NNRPIM	
	M1	M2	M1	M2	M1	M2
1	105.080	172.375	71.680	101.237	65.331	85.429
2	76.838	125.974	54.388	87.779	49.607	82.150
3	3.838	6.311	42.242	75.252	9.423	18.149
4	24.425	40.187	23.792	39.057	19.014	30.959
5	29.843	49.100	13.286	21.847	22.204	36.269
6	19.545	32.157	19.124	31.501	15.035	24.619
7	3.245	5.349	34.267	59.094	9.225	16.783
8	82.442	135.577	55.654	90.869	52.205	85.763
9	88.961	146.263	60.702	87.865	55.217	75.098
10	168.029	275.229	166.942	263.349	147.067	226.895
11	183.751	310.931	185.554	301.921	162.959	260.409
12	220.703	369.010	204.107	330.578	239.920	381.613
13	56.402	92.798	58.367	95.848	46.010	74.919
14	38.591	63.493	15.873	26.091	14.971	24.409
15	33.705	55.454	58.232	95.825	37.406	61.068
16	136.536	223.772	112.243	177.518	135.685	210.124
17	107.794	175.528	99.924	153.735	90.458	136.202
18	97.415	151.960	89.800	133.391	80.566	116.612

Table A. 25 Stress Values for specific points, for type of bone 3 at 70º

Points	FEM		RPIM		NNRPIM	
	M1	M2	M1	M2	M1	M2
1	75.330	123.515	51.319	72.121	46.819	60.744
2	51.863	84.946	37.146	59.588	33.580	55.577
3	3.034	4.987	30.846	55.220	6.661	12.891
4	24.554	40.398	24.312	39.936	19.296	31.453
5	31.761	52.256	14.046	23.103	23.549	38.478
6	21.062	34.654	21.033	34.630	16.485	26.977
7	2.468	4.067	22.328	37.920	6.452	11.435
8	57.898	95.289	38.513	62.933	36.387	59.490
9	57.907	95.292	39.435	57.659	35.876	49.589
10	129.671	214.177	130.115	207.321	114.258	178.064
11	141.668	241.114	144.553	237.104	126.372	203.705
12	168.298	282.159	158.727	257.843	185.594	296.268
13	55.243	90.891	61.052	100.321	43.978	71.717
14	39.498	64.986	16.744	27.534	16.124	26.289
15	39.164	64.436	60.957	100.305	37.435	61.199
16	77.509	125.352	60.206	93.603	73.392	111.615
17	60.279	96.166	52.457	78.120	48.303	70.237
18	53.875	82.387	47.223	68.658	42.656	59.912

Table A.26 Stress Values for specific points, for type of bone 3 at 80º

Points	FEM		RPIM		NNRPIM	
	M1	M2	M1	M2	M1	M2
1	43.491	71.240	29.480	40.995	26.978	34.444
2	25.920	42.344	19.034	29.813	16.770	27.469
3	2.286	3.754	18.792	33.895	3.879	7.443
4	24.244	39.888	24.278	39.905	19.162	31.269
5	32.952	54.216	14.520	23.886	24.386	39.853
6	22.428	36.901	22.591	37.174	17.712	28.959
7	1.888	3.108	10.593	17.081	3.686	6.046
8	32.004	52.770	20.428	33.268	19.638	31.529
9	25.624	42.310	17.184	26.119	15.699	23.057
10	87.651	147.153	89.532	145.439	78.124	124.125
11	95.647	164.563	99.359	165.431	86.112	141.093
12	111.023	187.058	108.834	177.717	125.900	202.303
13	52.763	86.811	62.730	103.131	41.837	68.322
14	40.078	65.941	17.288	28.435	16.833	27.445
15	44.457	73.145	62.681	103.123	38.302	62.643
16	21.320	31.592	19.254	29.627	19.812	29.335
17	20.121	32.778	14.844	26.604	12.687	21.385
18	16.795	29.371	14.006	28.199	11.246	21.207

Table A.27 Stress Values for specific points, for type of bone 3 at 90º

Points	FEM		RPIM		NNRPIM	
	M1	M2	M1	M2	M1	M2
1	12.229	20.015	7.570	10.572	7.241	9.490
2	9.687	15.974	5.312	6.369	4.869	5.247
3	1.807	2.969	7.862	13.842	2.088	3.224
4	23.518	38.694	23.694	38.968	18.624	30.422
5	33.356	54.880	14.682	24.152	24.670	40.320
6	23.518	38.694	23.694	38.968	18.624	30.422
7	1.807	2.969	7.862	13.842	2.088	3.224
8	9.687	15.974	5.312	6.369	4.869	5.247
9	12.229	20.015	7.570	10.572	7.241	9.490
10	44.079	77.637	46.971	80.657	40.184	67.491
11	48.176	85.265	51.904	89.971	43.893	75.227
12	51.482	87.732	56.802	93.841	63.468	103.687
13	49.098	80.781	63.286	104.088	39.853	65.152
14	40.279	66.270	17.473	28.742	17.073	27.836
15	49.098	80.781	63.286	104.088	39.853	65.152
16	51.482	87.732	56.802	93.841	63.468	103.687
17	48.176	85.265	51.904	89.971	43.893	75.227
18	44.079	77.637	46.971	80.657	40.184	67.491

Table A.28 Stress Values for specific points, for type of bone 4 at 10º

Points	FEM		RPIM		NNRPIM	
	M1	M2	M1	M2	M1	M2
1	188.651	309.731	129.939	185.263	118.488	157.017
2	150.715	247.401	104.881	169.523	96.814	158.696
3	7.728	12.720	73.694	129.679	18.120	34.287
4	18.993	31.249	15.214	24.875	13.192	21.335
5	16.193	26.643	8.703	14.251	13.235	21.459
6	16.585	27.288	12.385	20.279	10.921	17.696
7	7.558	12.444	72.011	126.330	18.048	33.979
8	151.518	248.802	105.007	169.993	97.194	159.305
9	185.565	304.735	127.803	182.613	116.518	154.939
10	266.609	428.968	258.987	398.948	229.260	344.361
11	291.940	487.587	288.201	459.929	255.037	398.610
12	356.158	591.762	317.268	509.272	376.667	592.318
13	43.597	71.731	41.251	67.478	47.671	77.168
14	33.923	55.815	14.808	24.184	2.611	4.198
15	32.855	54.058	40.666	66.620	45.246	73.256
16	339.107	562.374	298.668	478.294	355.645	557.732
17	276.550	460.157	270.950	430.042	240.452	373.589
18	252.294	403.953	243.375	372.605	215.826	322.082

Table A.29 Stress Values for specific points, for type of bone 4 at 20º

Points	FEM		RPIM		NNRPIM	
	M1	M2	M1	M2	M1	M2
1	181.592	298.107	125.079	178.138	114.069	150.898
2	143.428	235.399	100.026	161.532	92.198	151.126
3	7.482	12.314	71.197	125.475	17.338	32.888
4	20.478	33.693	17.214	28.159	14.701	23.797
5	18.391	30.260	9.516	15.599	14.662	23.822
6	16.072	26.444	12.227	20.071	10.639	17.302
7	7.148	11.770	67.883	118.881	17.198	32.281
8	145.012	238.159	100.274	162.457	92.946	152.326
9	175.514	288.265	120.871	172.918	110.188	146.805
10	261.714	422.120	255.090	394.144	225.609	339.964
11	286.440	479.280	283.798	454.110	250.792	393.114
12	348.539	579.632	312.235	501.757	370.135	582.818
13	48.413	79.654	43.330	70.897	48.125	77.943
14	34.536	56.823	14.563	23.793	3.749	6.071
15	28.284	46.537	42.278	69.355	43.504	70.491
16	314.951	521.740	275.598	440.737	328.726	514.692
17	256.127	425.254	249.818	395.240	222.062	343.828
18	233.518	372.851	224.339	342.260	199.147	296.082

Table A.30 Stress Values for specific points, for type of bone 4 at 30º

Points	FEM		RPIM		NNRPIM	
	M1	M2	M1	M2	M1	M2
1	169.017	277.427	116.417	165.601	106.183	140.199
2	131.796	216.264	92.137	148.633	84.784	138.962
3	7.024	11.558	66.551	117.479	16.038	30.498
4	21.894	36.023	19.196	31.427	16.174	26.215
5	21.324	35.085	10.642	17.465	16.612	27.044
6	16.198	26.652	13.065	21.496	11.085	18.098
7	6.538	10.769	61.709	107.843	15.833	29.612
8	134.110	220.298	92.500	149.986	85.877	140.716
9	160.132	263.041	110.265	157.971	100.511	134.217
10	248.884	402.488	243.453	377.403	215.109	325.259
11	272.260	456.449	270.781	434.514	238.933	375.687
12	330.334	549.890	297.732	479.021	352.366	555.623
13	52.317	86.077	46.153	75.570	48.003	77.810
14	35.453	58.332	14.178	23.179	5.015	8.144
15	25.633	42.175	44.820	73.616	41.638	67.557
16	281.239	465.267	244.189	389.840	291.842	456.046
17	227.960	377.497	221.116	348.475	196.941	303.652
18	207.678	330.493	198.510	301.586	176.431	261.129

Table A.31 Stress Values for specific points, for type of bone 4 at 40º

Points	FEM		RPIM		NNRPIM	
	M1	M2	M1	M2	M1	M2
1	151.322	248.344	104.224	148.048	95.079	125.257
2	116.186	190.602	81.461	131.231	74.806	122.585
3	6.372	10.483	59.905	105.946	14.262	27.196
4	23.099	38.005	20.960	34.344	17.462	28.343
5	24.446	40.221	11.878	19.511	18.729	30.536
6	16.936	27.866	14.642	24.121	12.132	19.857
7	5.754	9.479	53.689	93.571	13.999	26.058
8	119.159	195.785	81.928	132.970	76.211	124.840
9	139.902	229.854	96.317	138.241	87.788	117.570
10	228.531	370.704	224.450	349.264	198.095	300.719
11	249.853	419.828	249.566	401.769	219.839	346.889
12	302.123	503.482	274.225	441.793	323.928	511.600
13	55.075	90.616	49.287	80.775	47.316	76.784
14	36.547	60.131	13.692	22.404	6.226	10.122
15	25.847	42.526	47.867	78.696	39.875	64.814
16	239.029	394.725	205.435	327.214	246.154	383.640
17	192.944	318.408	185.749	291.225	165.878	254.331
18	175.594	278.232	166.704	251.887	148.394	218.334

Table A.32 Stress Values for specific points, for type of bone 4 at 50º

Points	FEM		RPIM		NNRPIM	
	M1	M2	M1	M2	M1	M2
1	129.060	211.766	88.882	126.027	81.103	106.544
2	97.093	159.228	68.337	109.871	62.579	102.507
3	5.553	9.133	51.474	91.245	12.070	23.089
4	23.988	39.466	22.366	36.677	18.464	30.010
5	27.378	45.046	13.065	21.474	20.745	33.857
6	18.129	29.829	16.592	27.341	13.534	22.172
7	4.832	7.961	44.084	76.530	11.759	21.738
8	100.633	165.397	68.892	111.943	64.251	105.193
9	115.459	189.746	79.462	114.347	72.419	97.390
10	201.297	327.776	198.677	310.622	175.102	267.120
11	219.928	370.575	220.820	356.908	194.108	307.624
12	264.788	441.860	242.456	391.246	285.713	452.130
13	56.539	93.024	52.331	85.842	46.126	74.956
14	37.676	61.989	13.155	21.549	7.296	11.870
15	28.835	47.442	50.995	83.888	38.455	62.638
16	189.657	312.336	160.590	254.874	193.117	299.778
17	152.215	249.907	144.848	225.337	129.864	197.445
18	138.301	217.782	129.943	194.801	115.930	169.087

Table A.33 Stress Values for specific points, for type of bone 4 at 60º

Points	FEM		RPIM		NNRPIM	
	M1	M2	M1	M2	M1	M2
1	102.894	168.784	70.842	100.194	64.671	84.618
2	75.104	123.104	53.160	85.189	48.470	79.320
3	4.604	7.570	41.522	73.833	9.539	18.311
4	24.492	40.296	23.322	38.275	19.111	31.103
5	29.874	49.152	14.091	23.169	22.476	36.707
6	19.567	32.195	18.604	30.649	15.051	24.652
7	3.822	6.299	33.212	57.272	9.190	16.793
8	79.095	130.060	53.787	87.529	50.358	82.355
9	87.536	143.920	60.201	87.005	54.862	74.288
10	168.000	275.002	166.904	262.641	146.813	225.467
11	183.387	310.173	185.399	301.268	162.506	259.063
12	219.439	366.847	203.375	328.890	238.858	378.980
13	56.637	93.184	54.964	90.236	44.541	72.494
14	38.708	63.686	12.629	20.714	8.176	13.306
15	33.582	55.252	53.849	88.606	37.594	61.359
16	134.641	220.617	111.108	175.166	134.398	207.092
17	107.103	174.256	99.713	152.954	90.029	134.822
18	97.010	151.180	89.408	132.294	80.062	115.023

Table A.34 Stress Values for specific points, for type of bone 4 at 70º

Points	FEM		RPIM		NNRPIM	
	M1	M2	M1	M2	M1	M2
1	73.660	120.773	50.675	71.376	46.302	60.197
2	50.978	83.479	36.438	57.982	32.951	53.766
3	3.586	5.894	30.401	54.309	6.777	13.044
4	24.576	40.435	23.773	39.042	19.364	31.554
5	31.765	52.262	14.875	24.465	23.794	38.876
6	21.046	34.627	20.453	33.678	16.492	26.994
7	2.824	4.654	21.525	36.580	6.409	11.428
8	55.277	90.972	37.114	60.514	34.989	57.052
9	57.054	93.890	39.153	57.115	35.689	49.044
10	129.717	214.107	130.146	206.881	114.127	177.100
11	141.418	240.585	144.429	236.625	126.037	202.750
12	167.513	280.808	158.239	256.722	184.852	294.469
13	55.362	91.087	56.944	93.555	42.722	69.648
14	39.529	65.037	12.184	20.007	8.829	14.371
15	39.002	64.170	56.147	92.391	37.439	61.193
16	75.996	122.856	59.190	91.628	72.327	109.282
17	59.598	94.934	52.224	77.399	47.963	69.184
18	53.509	81.699	46.855	67.764	42.246	58.766

Table A.35 Stress Values for specific points, for type of bone 4 at 80º

Points	FEM		RPIM		NNRPIM	
	M1	M2	M1	M2	M1	M2
1	42.371	69.402	29.045	40.578	26.617	34.183
2	25.858	42.238	18.864	29.255	16.667	26.739
3	2.614	4.293	18.617	33.500	3.991	7.588
4	24.232	39.869	23.690	38.934	19.205	31.334
5	32.939	54.195	15.364	25.274	24.616	40.228
6	22.395	36.846	21.980	36.171	17.722	28.979
7	2.057	3.387	10.069	16.280	3.653	6.045
8	30.193	49.793	19.552	31.865	18.748	30.145
9	25.310	41.794	17.118	25.918	15.670	22.812
10	87.765	147.228	89.624	145.265	78.113	123.644
11	95.485	164.224	99.257	165.117	85.894	140.539
12	110.712	186.521	108.573	177.152	125.471	201.353
13	52.776	86.833	58.104	95.519	40.870	66.732
14	40.055	65.903	11.884	19.531	9.230	15.025
15	44.318	72.917	57.691	94.915	38.015	62.166
16	20.056	29.533	18.209	28.090	18.668	27.718
17	19.186	31.197	14.360	25.787	12.298	20.731
18	16.577	28.990	13.781	27.869	11.060	20.985

Table A.36 Stress Values for specific points, for type of bone 4 at 90º

Points	FEM		RPIM		NNRPIM	
	M1	M2	M1	M2	M1	M2
1	11.583	18.960	7.341	10.545	7.033	9.552
2	9.115	15.031	5.263	6.435	4.790	5.204
3	1.958	3.217	7.806	13.796	2.149	3.347
4	23.487	38.643	23.082	37.959	18.647	30.458
5	33.338	54.850	15.531	25.549	24.895	40.688
6	23.487	38.643	23.082	37.959	18.647	30.458
7	1.958	3.217	7.806	13.796	2.149	3.347
8	9.115	15.031	5.263	6.435	4.790	5.204
9	11.583	18.960	7.341	10.545	7.033	9.552
10	44.229	77.795	47.093	80.696	40.275	67.465
11	47.978	84.924	51.781	89.748	43.763	75.023
12	51.524	87.843	56.655	93.674	63.251	103.462
13	49.022	80.656	58.361	95.985	39.224	64.116
14	40.237	66.202	11.779	19.364	9.365	15.245
15	49.022	80.656	58.361	95.985	39.224	64.116
16	51.524	87.843	56.655	93.674	63.251	103.462
17	47.978	84.924	51.781	89.748	43.763	75.023
18	44.229	77.795	47.093	80.696	40.275	67.465

Table A.37 Stress Values for specific points, for type of bone 5 at 10º

Points	FEM		RPIM		NNRPIM	
	M1	M2	M1	M2	M1	M2
1	178.395	292.883	126.030	179.904	115.710	152.746
2	137.225	225.126	96.765	153.567	89.105	141.616
3	12.433	20.452	69.244	121.344	18.633	34.963
4	19.694	32.403	15.592	25.457	13.730	22.151
5	16.919	27.838	10.339	16.908	14.511	23.476
6	17.473	28.750	12.943	21.169	11.566	18.706
7	12.104	19.915	67.372	117.752	18.435	34.517
8	137.240	225.231	96.524	153.582	89.085	141.887
9	175.603	288.368	124.029	177.284	113.844	150.590
10	265.553	426.355	258.090	394.256	227.184	335.741
11	289.355	482.438	287.052	455.701	252.175	390.356
12	346.735	575.812	312.296	498.442	369.543	575.642
13	44.881	73.844	43.202	70.587	45.680	73.771
14	35.277	58.044	26.259	42.865	15.322	24.698
15	34.378	56.565	41.133	67.267	43.783	70.736
16	329.429	546.035	293.535	467.197	348.450	540.924
17	273.814	454.786	269.793	425.811	237.620	365.376
18	251.039	401.051	242.307	367.747	213.639	313.423

Table A.38 Stress Values for specific points, for type of bone 5 at 20º

Points	FEM		RPIM		NNRPIM	
	M1	M2	M1	M2	M1	M2
1	171.654	281.782	121.279	173.011	111.365	146.863
2	130.955	214.799	92.469	146.541	85.047	135.002
3	12.049	19.819	67.045	117.643	17.895	33.606
4	21.022	34.588	17.373	28.382	15.151	24.466
5	18.963	31.202	11.141	18.242	15.785	25.597
6	16.934	27.863	12.640	20.729	11.252	18.276
7	11.403	18.764	63.358	110.570	17.504	32.727
8	130.984	215.006	91.994	146.570	85.007	135.536
9	166.154	272.887	117.339	167.849	107.689	142.617
10	260.805	419.767	254.318	389.744	223.683	331.756
11	284.038	474.459	282.700	450.066	248.042	385.209
12	339.668	564.597	307.559	491.538	363.362	566.959
13	49.493	81.433	44.760	73.158	45.992	74.317
14	35.730	58.789	25.534	41.692	15.454	24.946
15	29.745	48.943	40.932	67.022	42.381	68.546
16	305.578	505.938	270.603	429.993	321.813	498.570
17	253.426	419.992	248.703	391.189	219.371	336.003
18	232.217	369.927	223.230	337.534	197.002	287.796

Table A.39 Stress Values for specific points, for type of bone 5 at 30º

Points	FEM		RPIM		NNRPIM	
	M1	M2	M1	M2	M1	M2
1	159.696	262.118	112.842	160.862	103.635	136.525
2	120.718	197.964	85.370	135.066	78.409	124.287
3	11.313	18.606	62.821	110.385	16.622	31.239
4	22.272	36.645	19.118	31.261	16.533	26.740
5	21.725	35.745	12.267	20.115	17.558	28.542
6	16.941	27.874	13.195	21.699	11.605	18.935
7	10.371	17.068	57.434	100.051	16.051	29.956
8	120.760	198.267	84.674	135.108	78.352	125.068
9	151.656	249.115	107.081	153.318	98.262	130.319
10	248.148	400.461	242.828	373.425	213.390	317.710
11	270.105	452.088	269.763	430.769	236.376	368.367
12	322.281	536.221	293.486	469.712	346.143	541.052
13	53.171	87.483	46.397	75.888	45.825	74.122
14	36.412	59.911	24.379	39.825	15.654	25.321
15	26.811	44.114	41.361	67.824	40.865	66.206
16	272.449	450.472	239.472	379.755	285.409	441.086
17	225.365	372.484	220.072	344.715	194.469	296.446
18	206.367	327.630	197.391	297.130	174.392	253.466

Table A.40 Stress Values for specific points, for type of bone 5 at 40º

Points	FEM		RPIM		NNRPIM	
	M1	M2	M1	M2	M1	M2
1	142.899	234.510	100.982	143.843	92.764	122.057
2	106.836	175.154	75.690	119.503	69.402	109.807
3	10.250	16.855	56.707	99.803	14.857	27.940
4	23.318	38.366	20.651	33.803	17.739	28.739
5	24.695	40.631	13.522	22.198	19.515	31.784
6	17.494	28.783	14.451	23.807	12.529	20.507
7	9.046	14.890	49.790	86.531	14.126	26.293
8	106.890	175.543	74.797	119.557	69.328	110.810
9	132.565	217.798	93.577	134.147	85.857	114.082
10	227.987	369.060	223.988	345.825	196.635	294.057
11	248.000	416.042	248.656	398.430	217.549	340.370
12	295.124	491.584	270.528	433.661	318.435	498.748
13	55.691	91.630	47.918	78.451	45.196	73.207
14	37.232	61.259	22.884	37.408	15.897	25.774
15	26.534	43.659	42.351	69.546	39.417	64.001
16	231.078	381.370	201.121	318.066	240.382	370.275
17	190.517	313.767	184.800	287.854	163.695	247.951
18	174.308	275.509	165.605	247.827	146.522	211.523

Table A.41 Stress Values for specific points, for type of bone 5 at 50º

Points	FEM		RPIM		NNRPIM	
	M1	M2	M1	M2	M1	M2
1	121.786	199.822	86.069	122.485	79.090	103.915
2	89.751	147.093	63.737	100.341	58.310	92.015
3	8.899	14.631	48.901	86.236	12.661	23.818
4	24.067	39.598	21.849	35.799	18.669	30.296
5	27.503	45.252	14.740	24.218	21.400	34.904
6	18.480	30.406	16.117	26.565	13.814	22.638
7	7.480	12.316	40.678	70.453	11.794	21.862
8	89.816	147.556	62.674	100.406	58.222	93.210
9	109.477	179.916	77.248	110.937	70.863	94.421
10	200.958	326.557	198.389	307.818	173.943	261.542
11	218.421	367.457	220.039	354.063	192.151	302.096
12	259.047	432.079	239.405	384.516	281.104	441.370
13	56.918	93.648	49.159	80.566	44.164	71.659
14	38.085	62.662	21.178	34.654	16.151	26.247
15	29.020	47.748	43.750	71.923	38.229	62.225
16	182.768	300.800	156.777	246.895	188.155	288.378
17	150.001	245.729	144.008	222.428	128.025	192.067
18	137.075	215.266	128.891	191.247	114.277	163.330

Table A.42 Stress Values for specific points, for type of bone 5 at 60º

Points	FEM		RPIM		NNRPIM	
	M1	M2	M1	M2	M1	M2
1	96.984	159.082	68.545	97.425	63.019	82.646
2	69.986	114.641	49.873	78.156	45.471	71.442
3	7.312	12.019	39.645	70.102	10.109	19.007
4	24.459	40.243	22.630	37.114	19.257	31.303
5	29.905	49.202	15.800	25.974	23.032	37.602
6	19.729	32.460	17.909	29.514	15.236	24.968
7	5.747	9.466	30.397	52.341	9.141	16.815
8	70.059	115.163	48.673	78.229	45.372	72.791
9	83.083	136.601	58.579	84.388	53.726	71.933
10	167.872	274.234	166.795	260.549	145.988	221.139
11	182.252	307.785	184.762	298.988	160.936	254.681
12	215.116	359.462	201.043	323.739	235.257	370.617
13	56.788	93.434	49.995	82.022	42.828	69.628
14	38.870	63.953	19.439	31.848	16.386	26.684
15	33.416	54.979	45.361	74.623	37.473	61.133
16	128.990	211.198	107.846	168.497	130.342	197.930
17	105.112	170.565	98.976	150.532	88.572	130.569
18	95.868	148.920	88.422	129.326	78.674	110.487

Table A.43 Stress Values for specific points, for type of bone 5 at 70º

Points	FEM		RPIM		NNRPIM	
	M1	M2	M1	M2	M1	M2
1	69.282	113.588	48.960	69.470	45.061	58.947
2	48.217	78.911	34.563	53.674	31.315	48.751
3	5.568	9.150	29.264	51.955	7.312	13.697
4	24.465	40.252	22.946	37.666	19.465	31.693
5	31.729	52.203	16.614	27.323	24.283	39.666
6	21.057	34.645	19.607	32.293	16.613	27.201
7	3.979	6.557	19.380	32.943	6.295	11.372
8	48.296	79.473	33.270	53.753	31.209	50.210
9	54.241	89.266	38.167	55.380	35.003	47.388
10	129.795	213.794	130.212	205.547	113.656	174.143
11	140.655	238.942	143.941	234.952	124.890	199.629
12	164.713	276.006	156.662	253.255	182.337	288.715
13	55.309	91.001	50.349	82.681	41.330	67.329
14	39.499	64.988	17.896	29.363	16.576	27.036
15	38.656	63.601	46.979	77.305	37.269	60.899
16	71.651	115.681	56.362	86.147	69.123	102.400
17	57.715	91.516	51.508	75.313	46.868	66.056
18	52.459	79.689	45.927	65.405	41.150	55.591

Table A.44 Stress Values for specific points, for type of bone 5 at 80º

Points	FEM		RPIM		NNRPIM	
	M1	M2	M1	M2	M1	M2
1	39.619	64.889	27.957	39.608	25.816	33.709
2	25.426	41.522	18.448	27.848	16.445	24.781
3	3.809	6.258	18.206	32.541	4.471	8.199
4	24.083	39.623	22.775	37.420	19.280	31.441
5	32.864	54.071	17.124	28.167	25.064	40.957
6	22.303	36.695	21.051	34.645	17.804	29.117
7	2.538	4.183	8.699	14.153	3.554	6.018
8	25.505	42.088	17.137	27.929	16.337	26.286
9	24.110	39.825	16.774	25.159	15.431	21.965
10	88.024	147.333	89.844	144.691	78.001	122.126
11	95.035	163.246	98.900	164.042	85.182	138.727
12	109.458	184.358	107.719	175.357	124.049	198.289
13	52.554	86.467	50.184	82.480	39.841	65.022
14	39.903	65.653	16.813	27.620	16.698	27.262
15	43.926	72.272	48.414	79.657	37.650	61.557
16	16.726	24.126	15.403	24.061	15.611	23.532
17	16.716	27.068	13.074	23.691	11.276	19.151
18	15.823	27.750	13.210	27.126	10.639	20.651

Table A.45 Stress Values for specific points, for type of bone 5 at 90º

Points	FEM		RPIM		NNRPIM	
	M1	M2	M1	M2	M1	M2
1	10.254	16.802	6.866	10.641	6.654	9.877
2	8.082	13.329	5.256	6.806	4.765	5.387
3	2.446	4.021	7.773	13.833	2.412	3.831
4	23.343	38.406	22.131	36.393	18.715	30.564
5	33.249	54.705	17.298	28.455	25.330	41.396
6	23.343	38.406	22.131	36.393	18.715	30.564
7	2.446	4.021	7.773	13.833	2.412	3.831
8	8.082	13.329	5.256	6.806	4.765	5.387
9	10.254	16.802	6.866	10.641	6.654	9.877
10	44.568	78.135	47.391	80.760	40.479	67.335
11	47.541	84.151	51.452	89.100	43.415	74.407
12	51.566	87.987	56.256	93.183	62.689	102.811
13	48.680	80.094	49.519	81.441	38.554	63.006
14	40.043	65.883	16.421	26.990	16.741	27.341
15	48.680	80.094	49.519	81.441	38.554	63.006
16	51.566	87.987	56.256	93.183	62.689	102.811
17	47.541	84.151	51.452	89.100	43.415	74.408
18	44.568	78.135	47.391	80.760	40.479	67.335

Appendix 4

In this appendix it is presented the graphs where it is possible to observe how stress varies in function of the value of the angles. The numbers of the title of each graphic correspond to the numbers from the points mentioned in section 6.1.

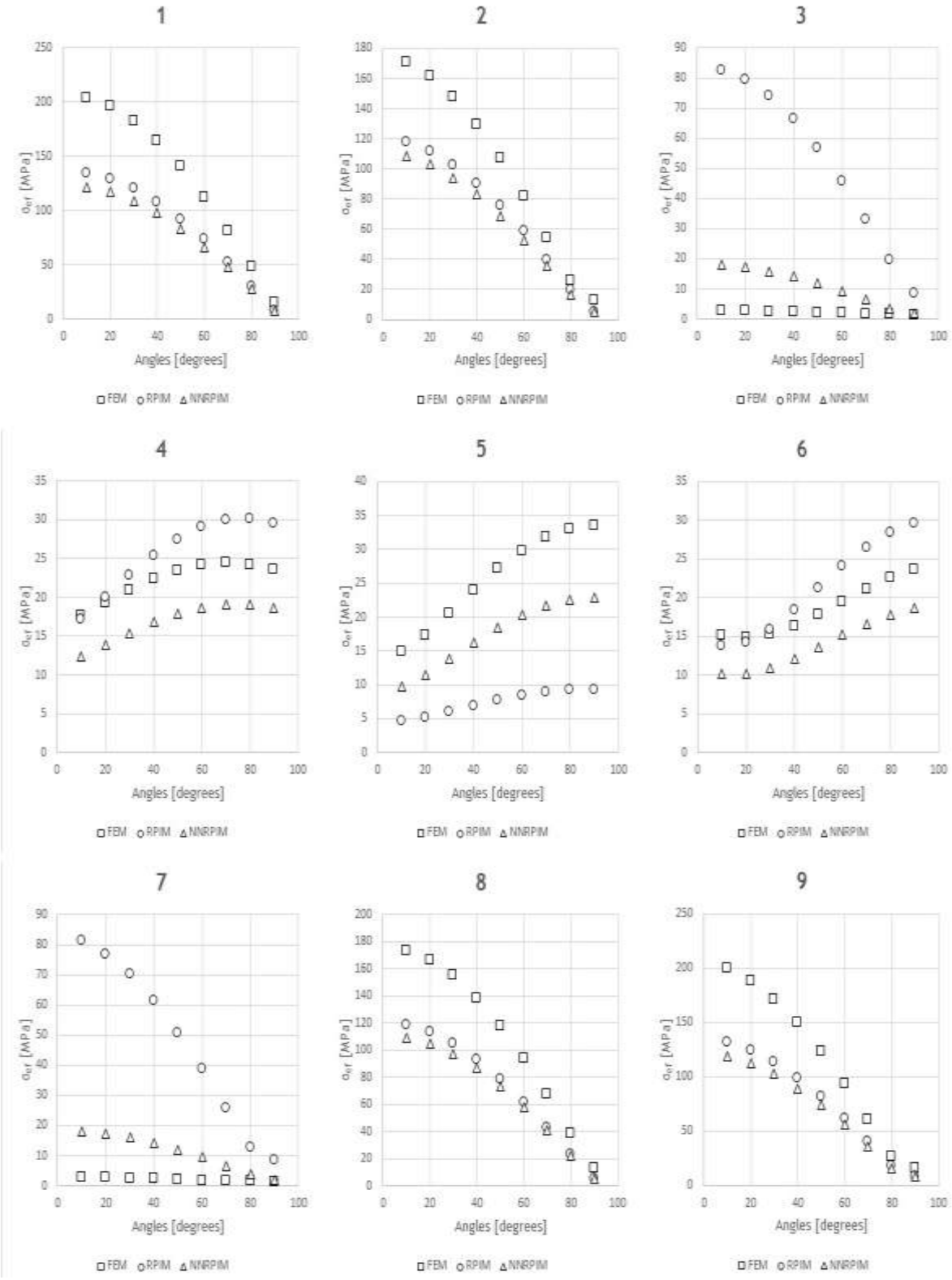

Figure A.31 Discrete stress values for type of bone 1, 'Model 1' and from bone side

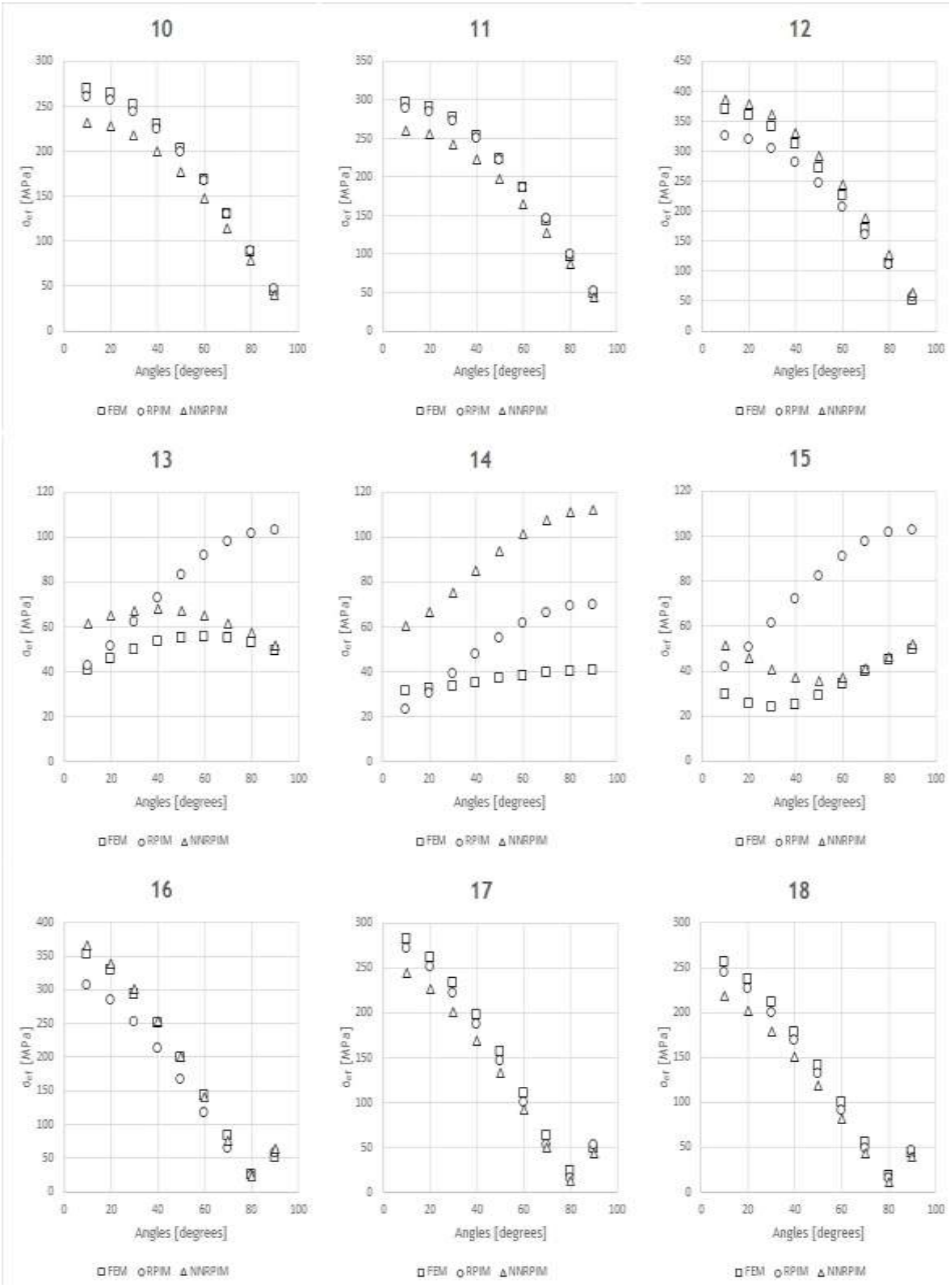

Figure A.32 Discrete stress values for type of bone 1, for 'Model 1' and from implant side

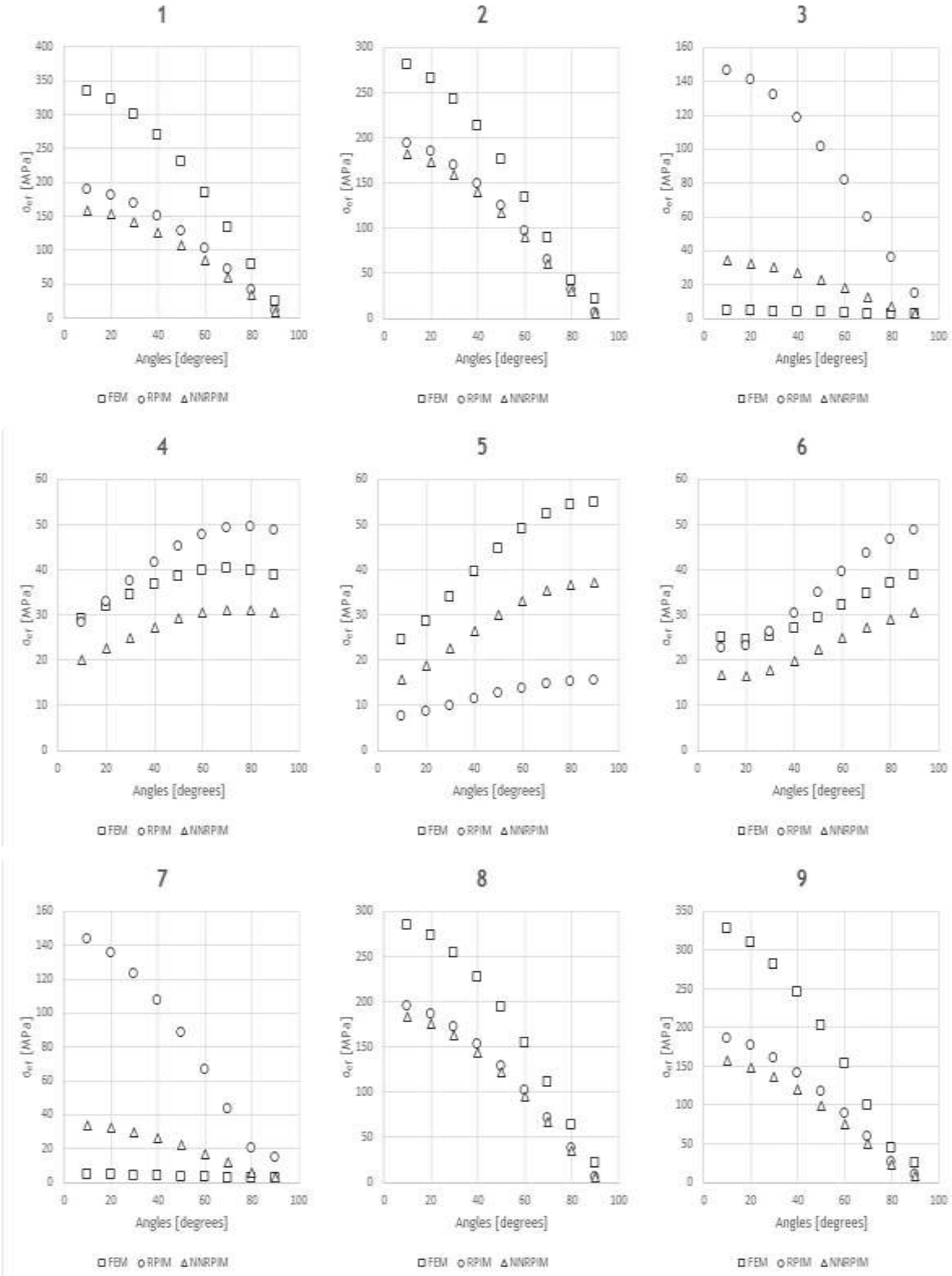

Figure A.33 Discrete stress values for type of bone 1, 'Model 2' and from bone side

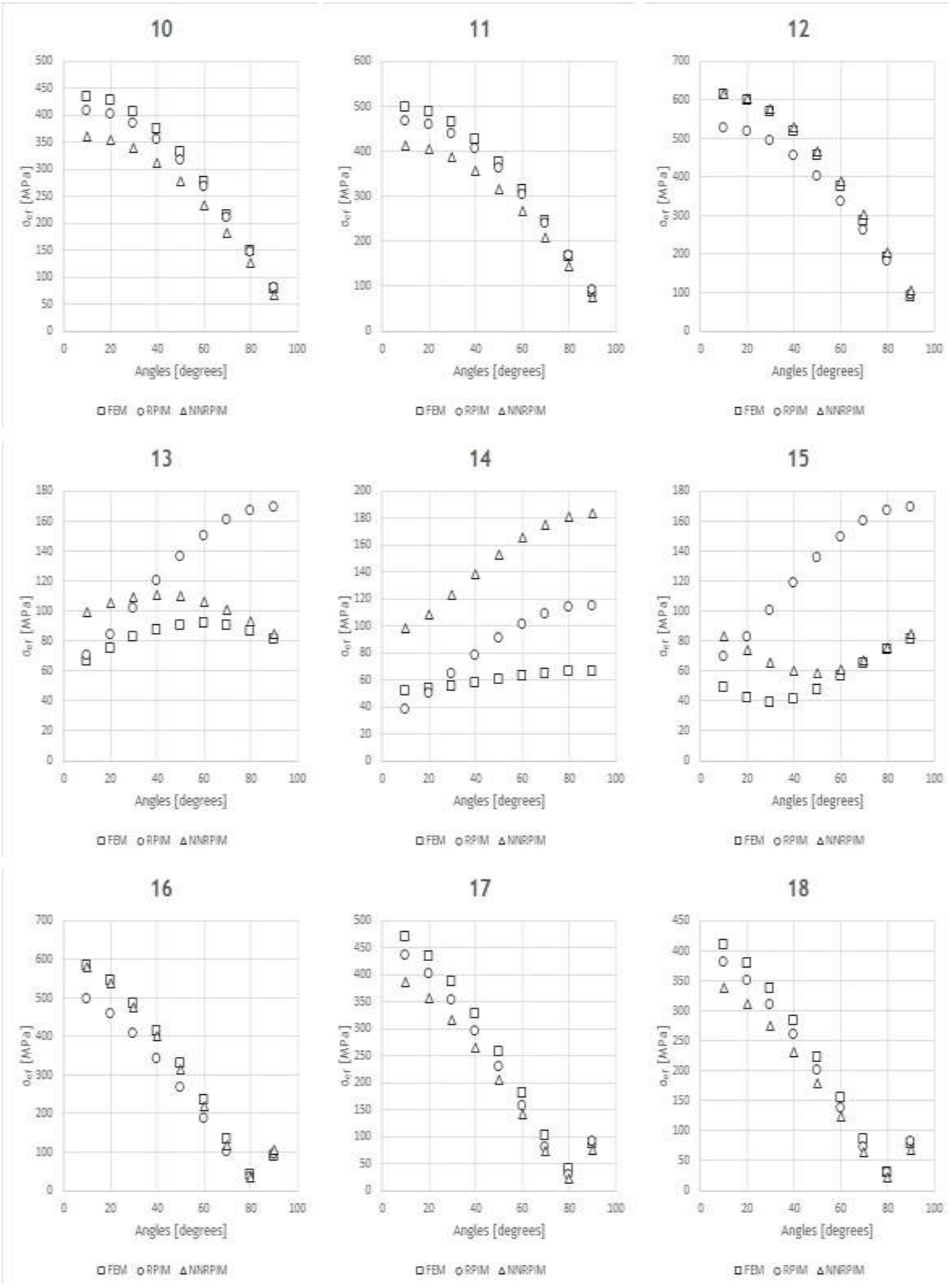

Figure A.34 Discrete stress values for type of bone 1, for 'Model 2' and from implant side

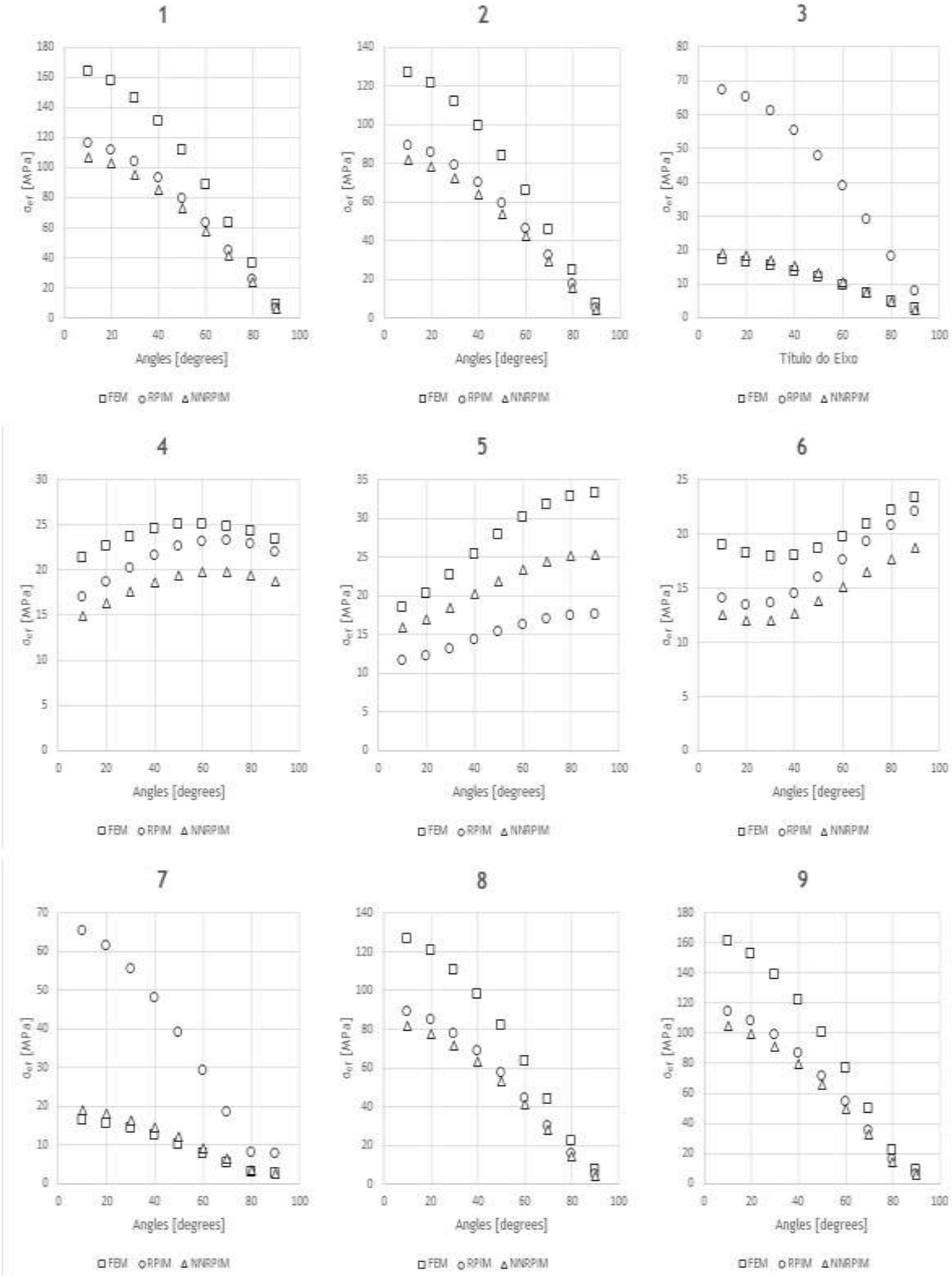

Figure A.35 Discrete stress values for type of bone 2, 'Model 1' and from bone side

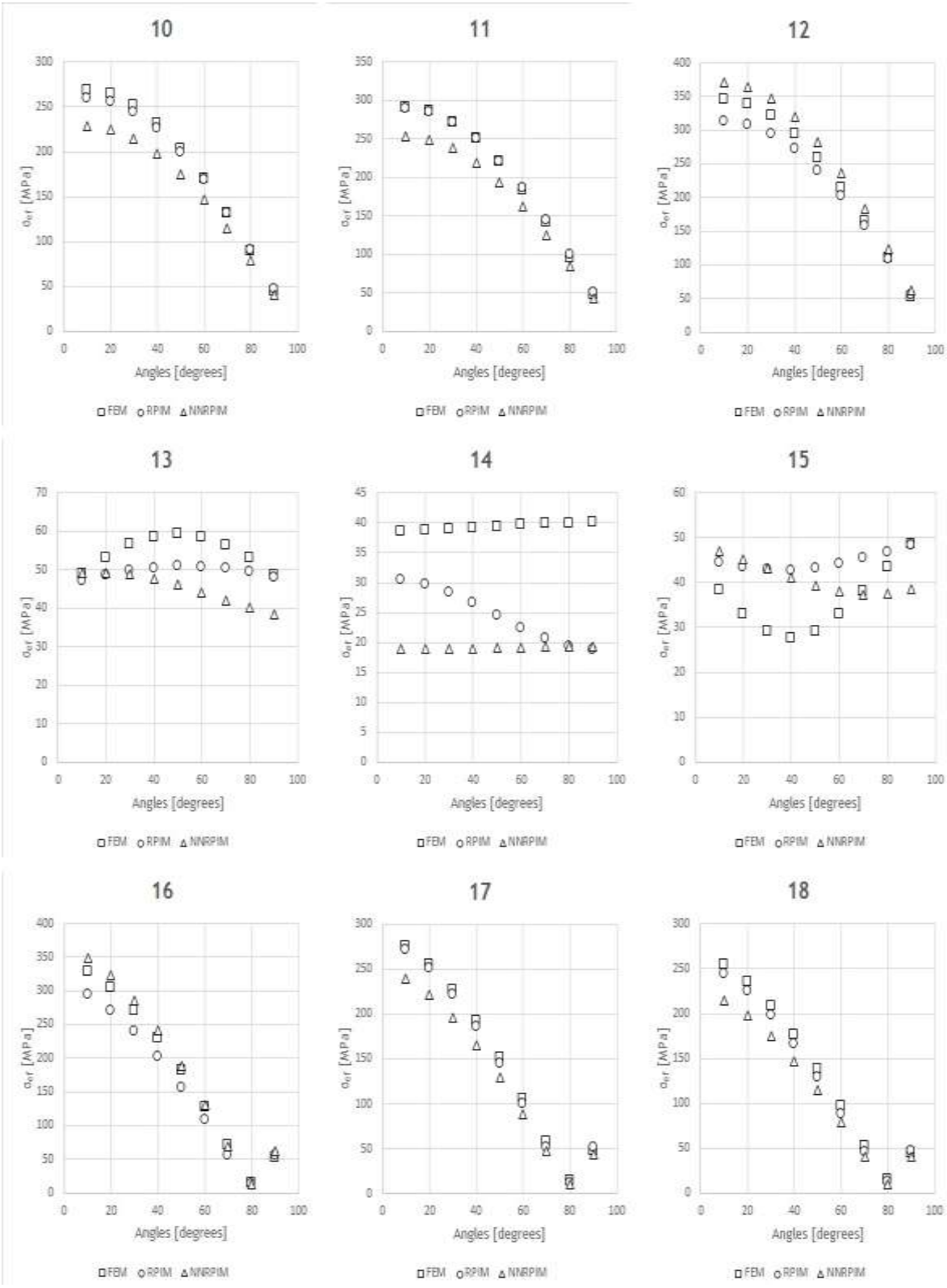

Figure A.36 Discrete stress values for type of bone 2, 'Model 1' and from implant side

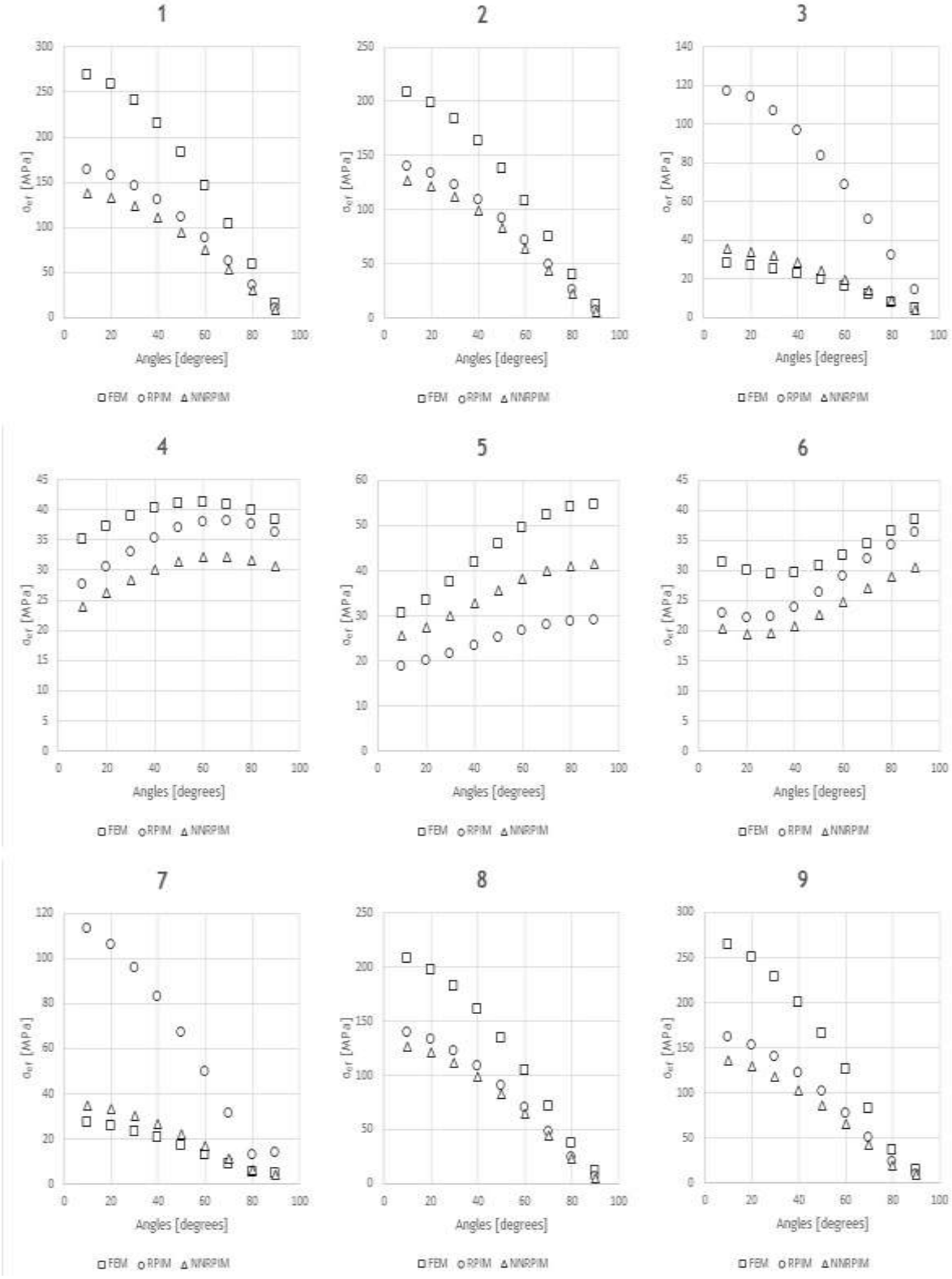

Figure A.37 Discrete stress values for type of bone 2, 'Model 2' and from bone side

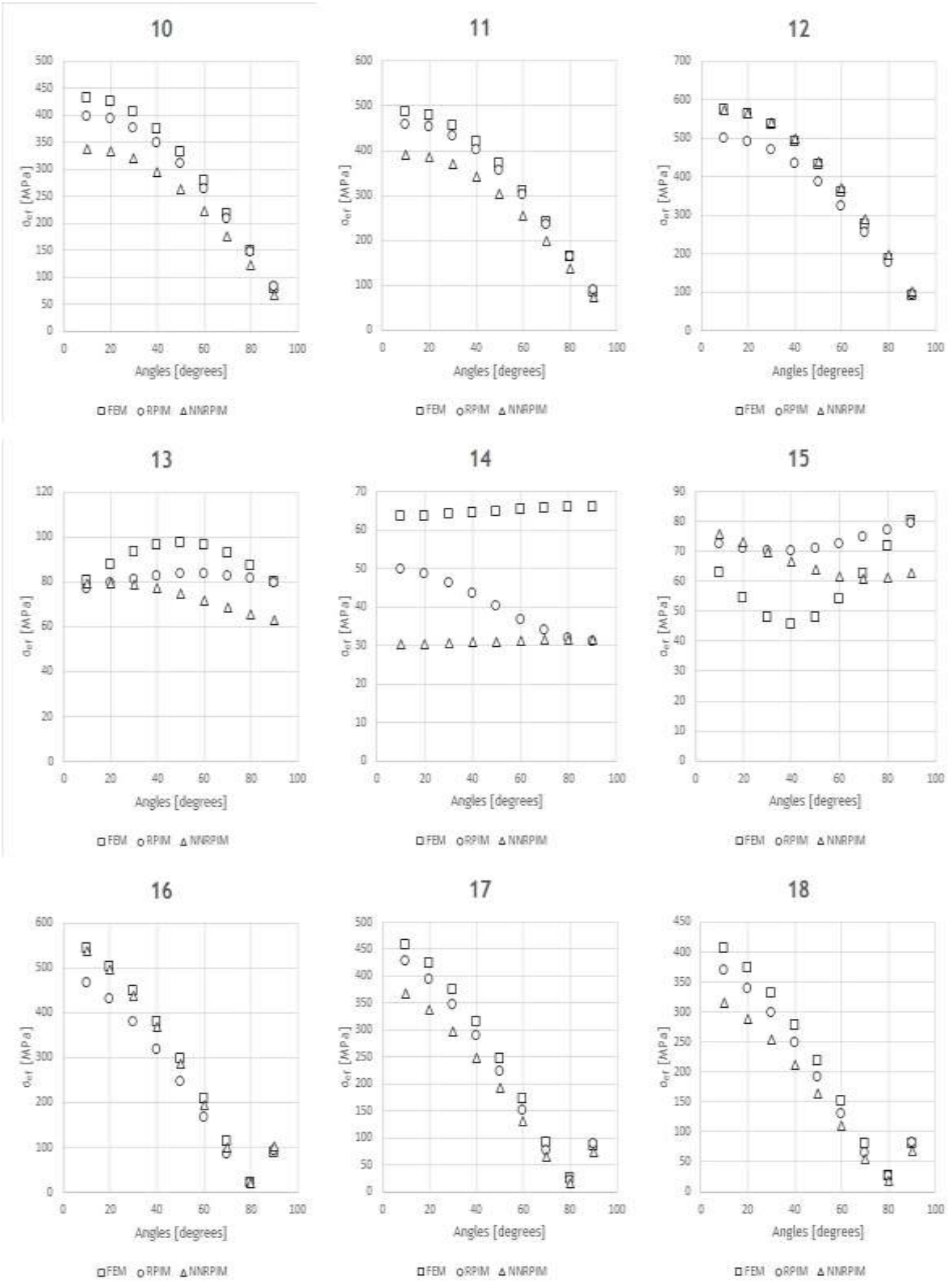

Figure A.38 Discrete stress values for type of bone 2, 'Model 2' and from implant side

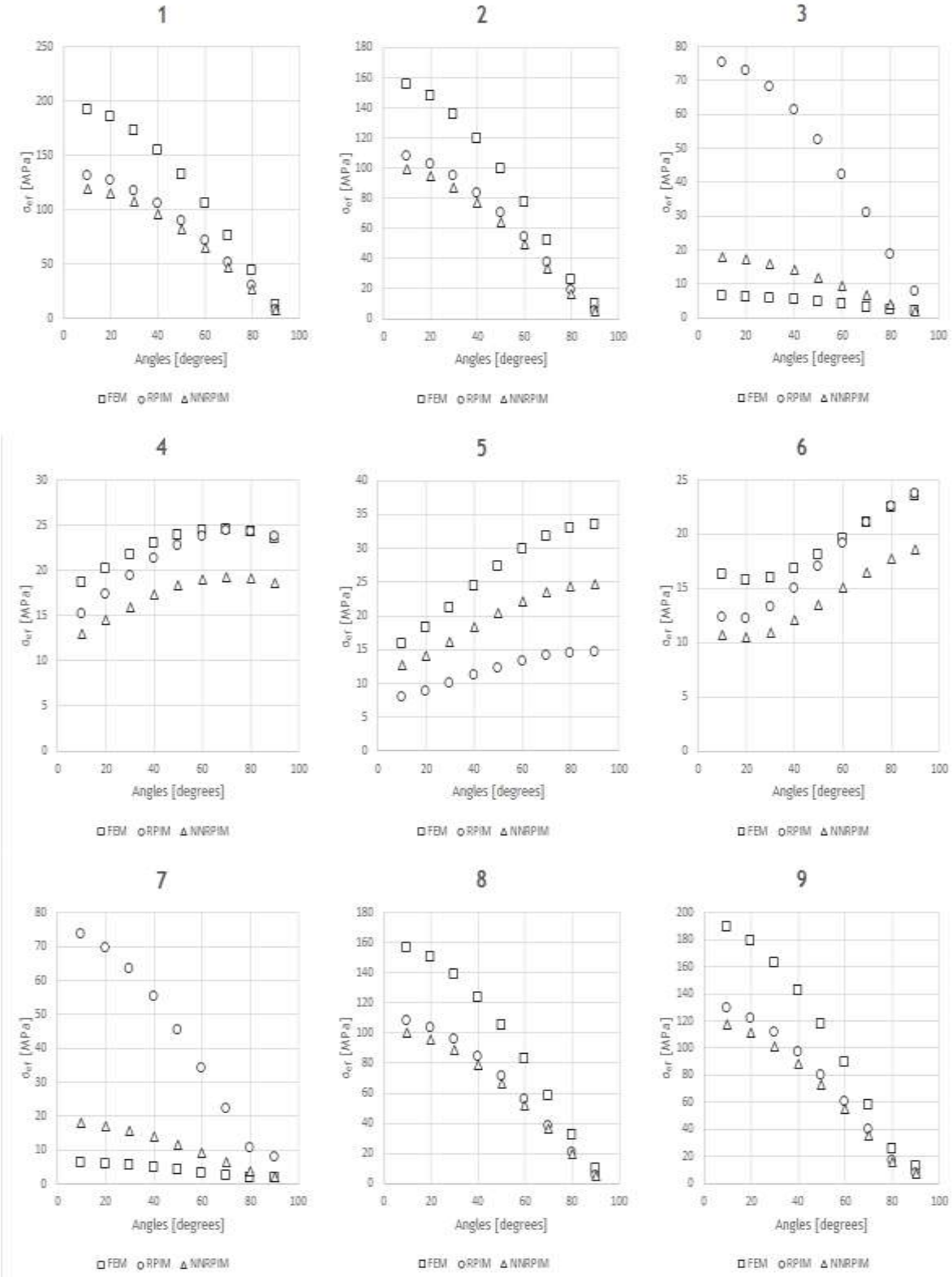

Figure A.39 Discrete stress values for type of bone 3, 'Model 1' and from bone side

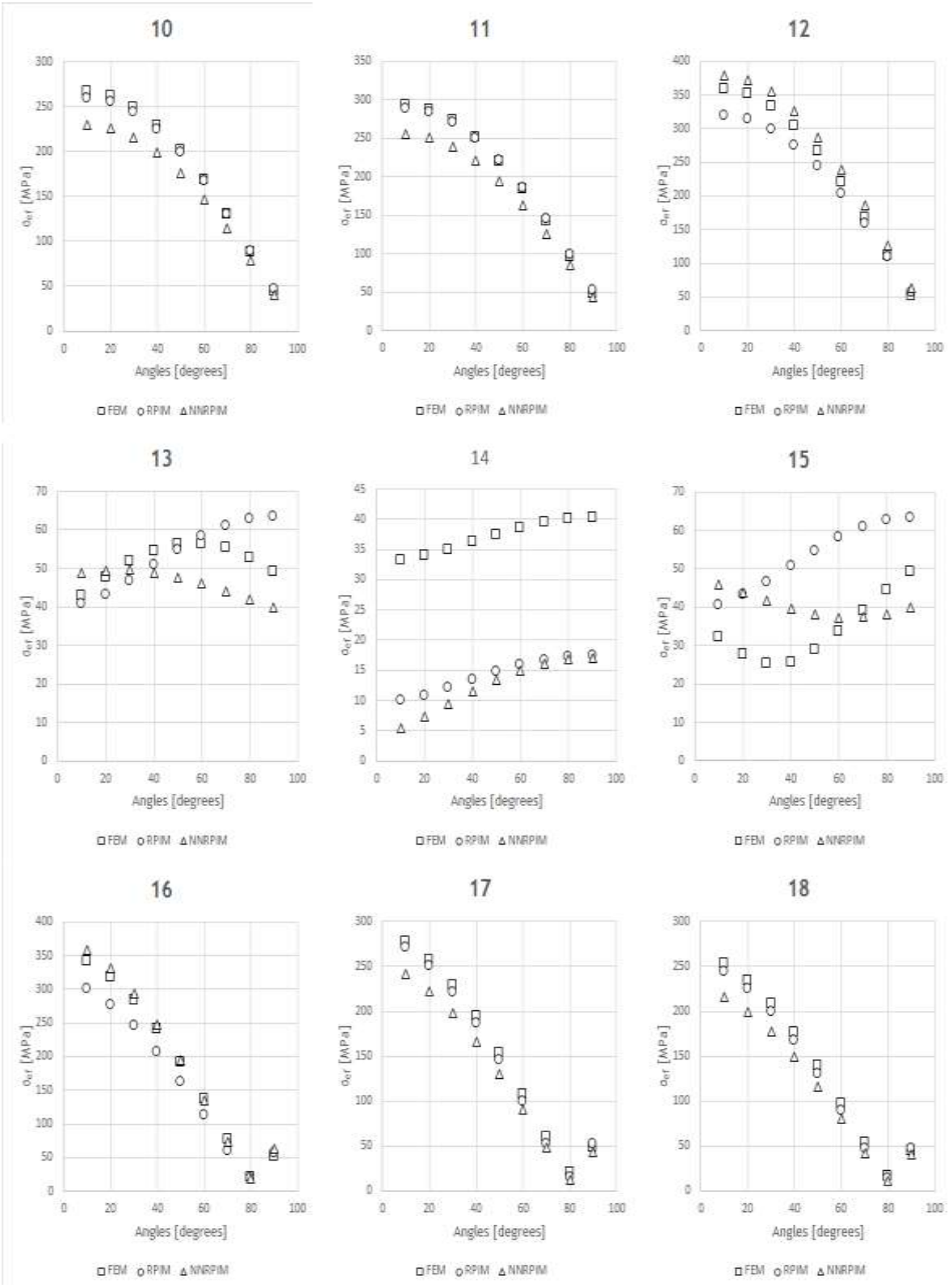

Figure A.40 Discrete stress values for type of bone 3, 'Model 1' and from implant side

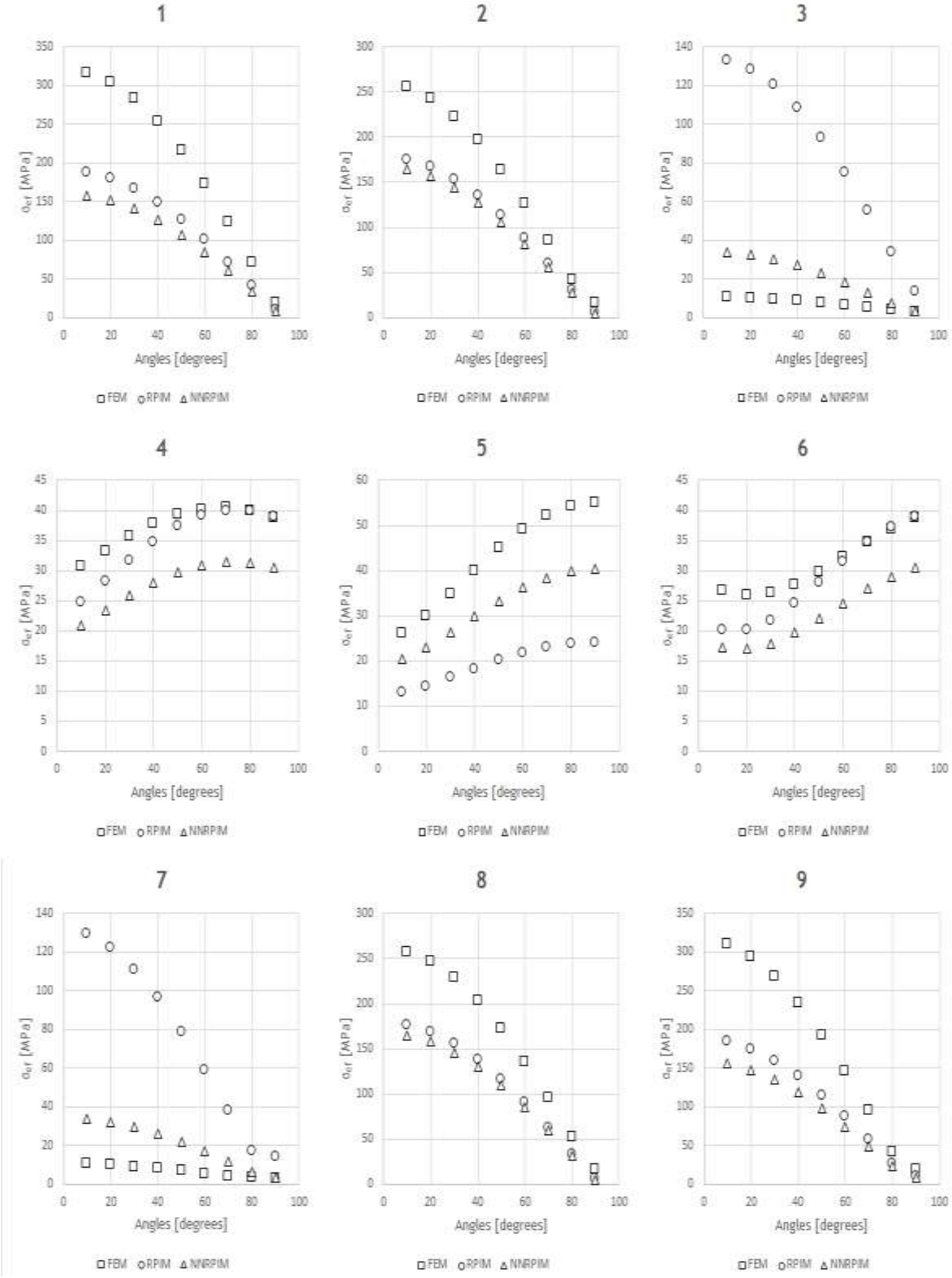

Figure A.41 Discrete stress values for type of bone 3, 'Model 2' and from bone side

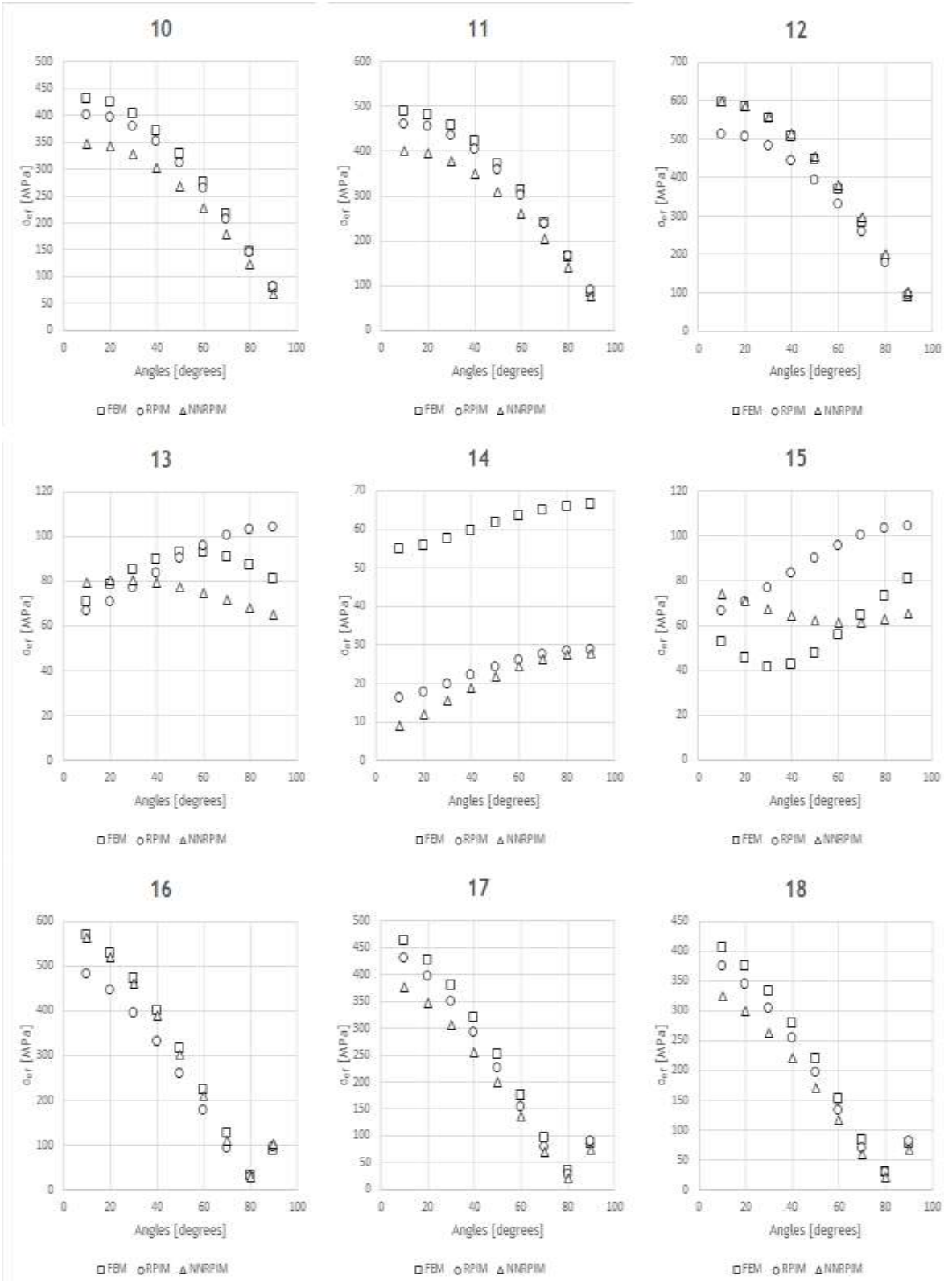

Figure A.42 Discrete stress values for type of bone 3, 'Model 2' and from implant side

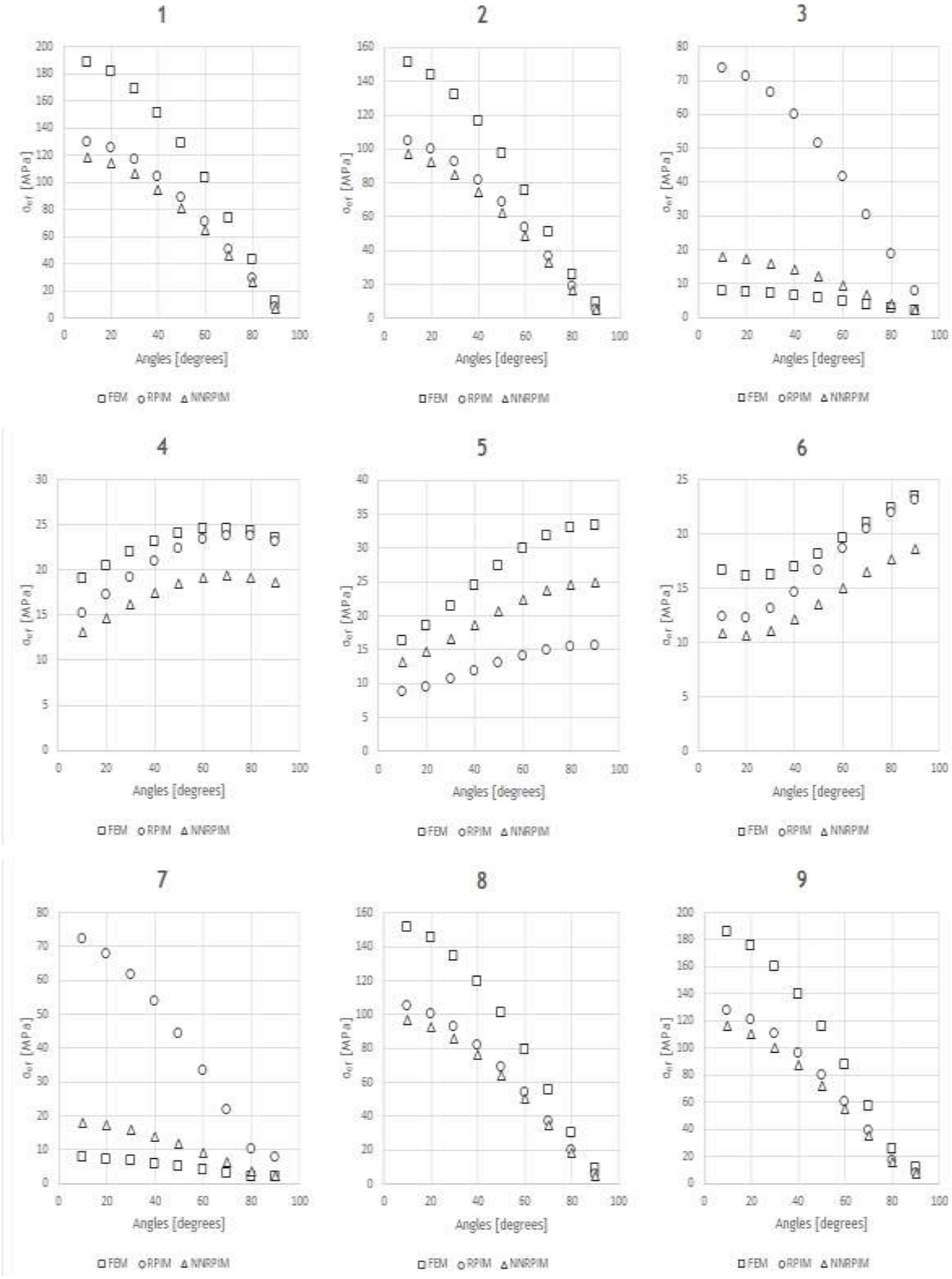

Figure A.43 Discrete stress values for type of bone 4, 'Model 1' and from bone side

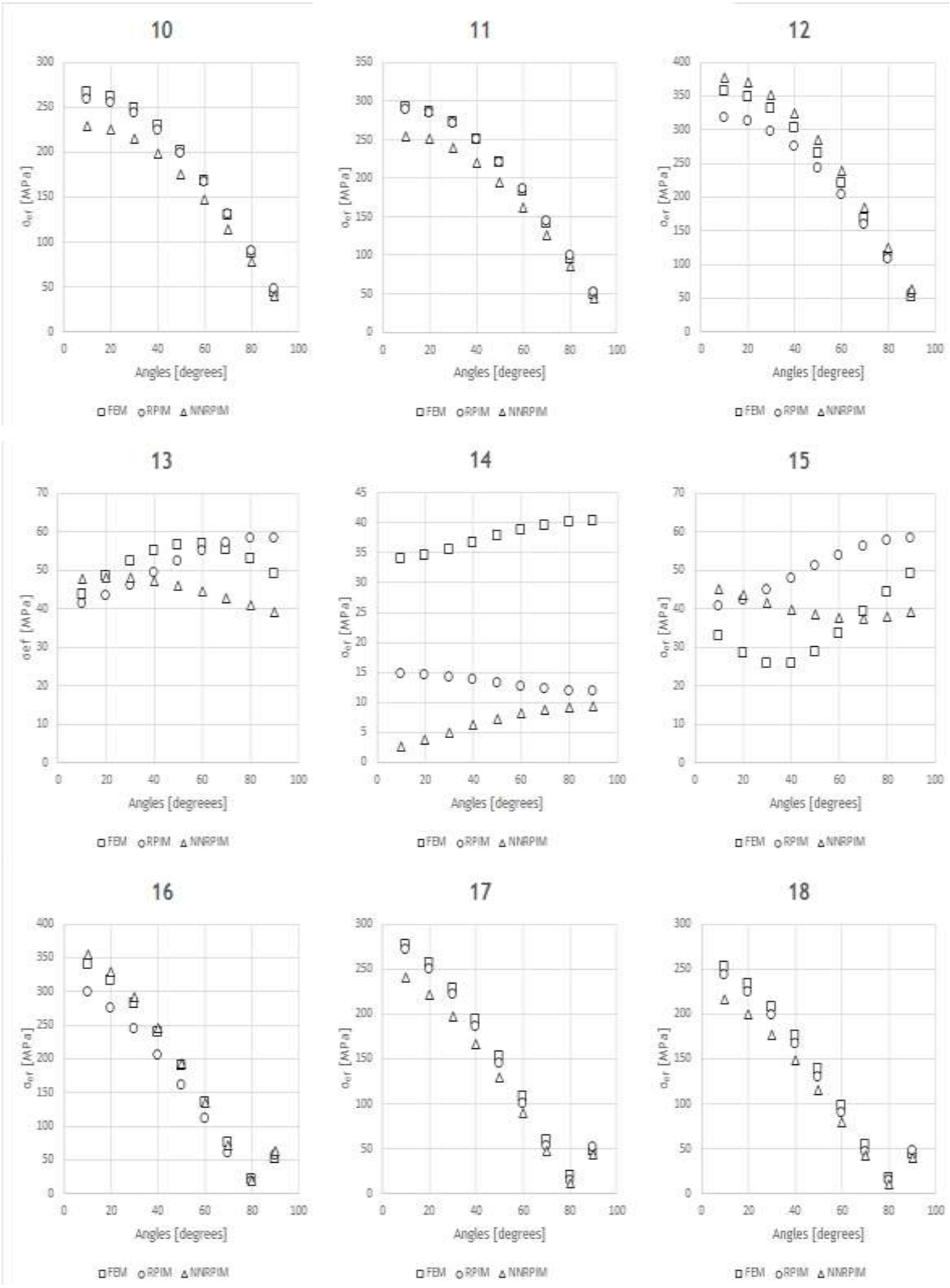

Figure A.44 Discrete stress values for type of bone 4, 'Model 1' and from implant side

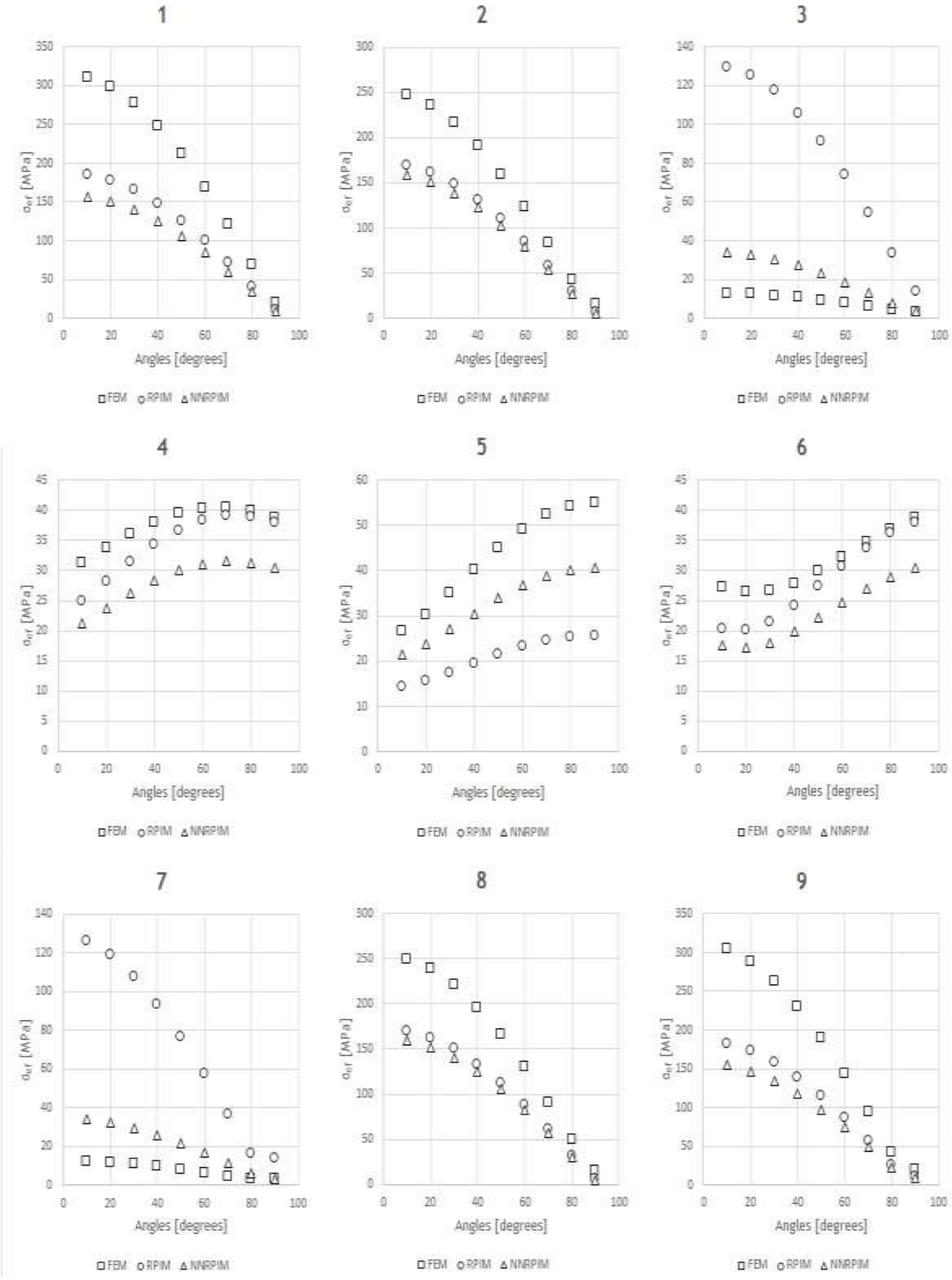

Figure A.45 Discrete stress values for type of bone 4, 'Model 2' and from bone side

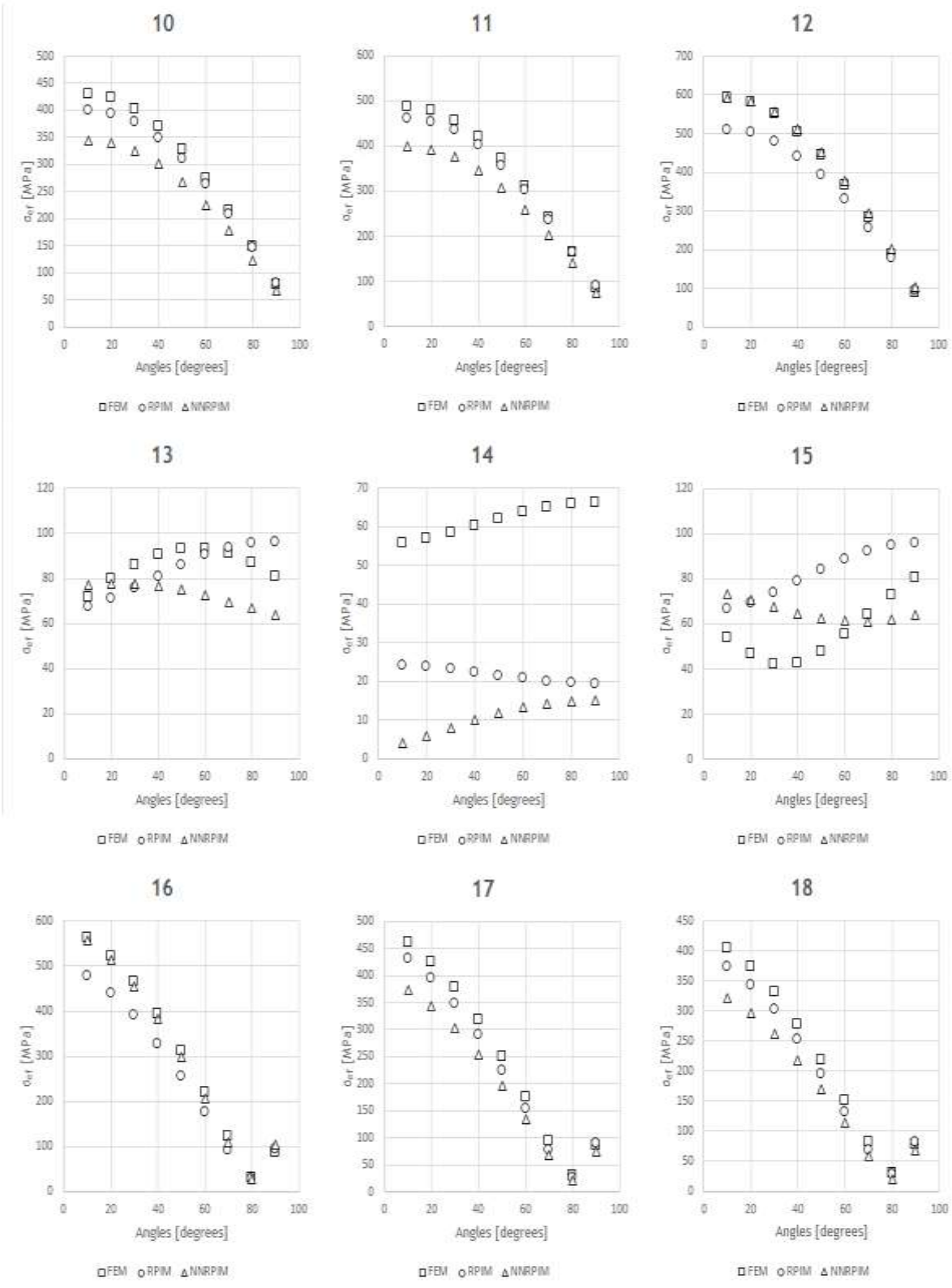

Figure A.46 Discrete stress values for type of bone 4, 'Model 2' and from implant side

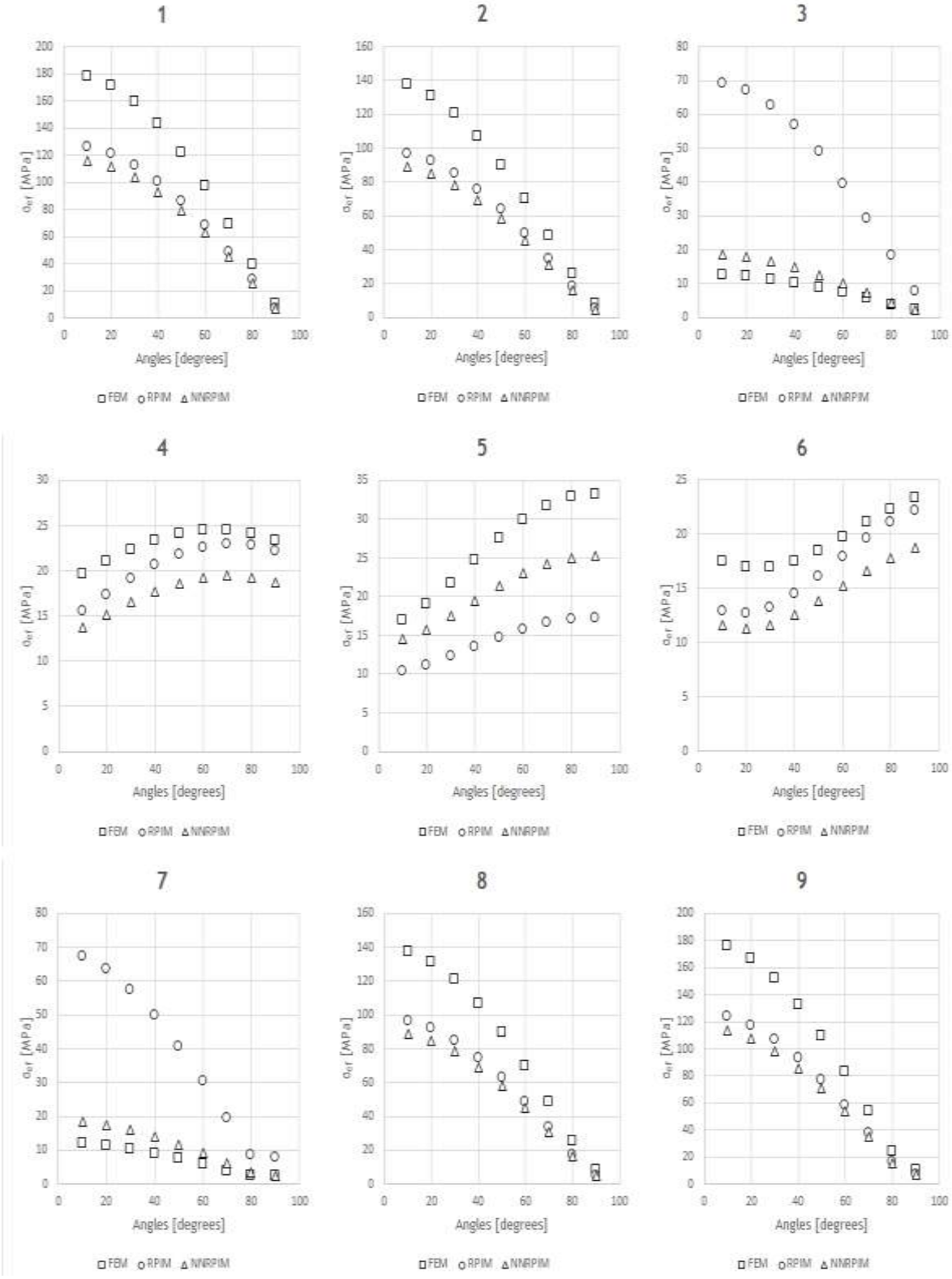

Figure A.47 Discrete stress values for type of bone 5, 'Model 1' and from bone side

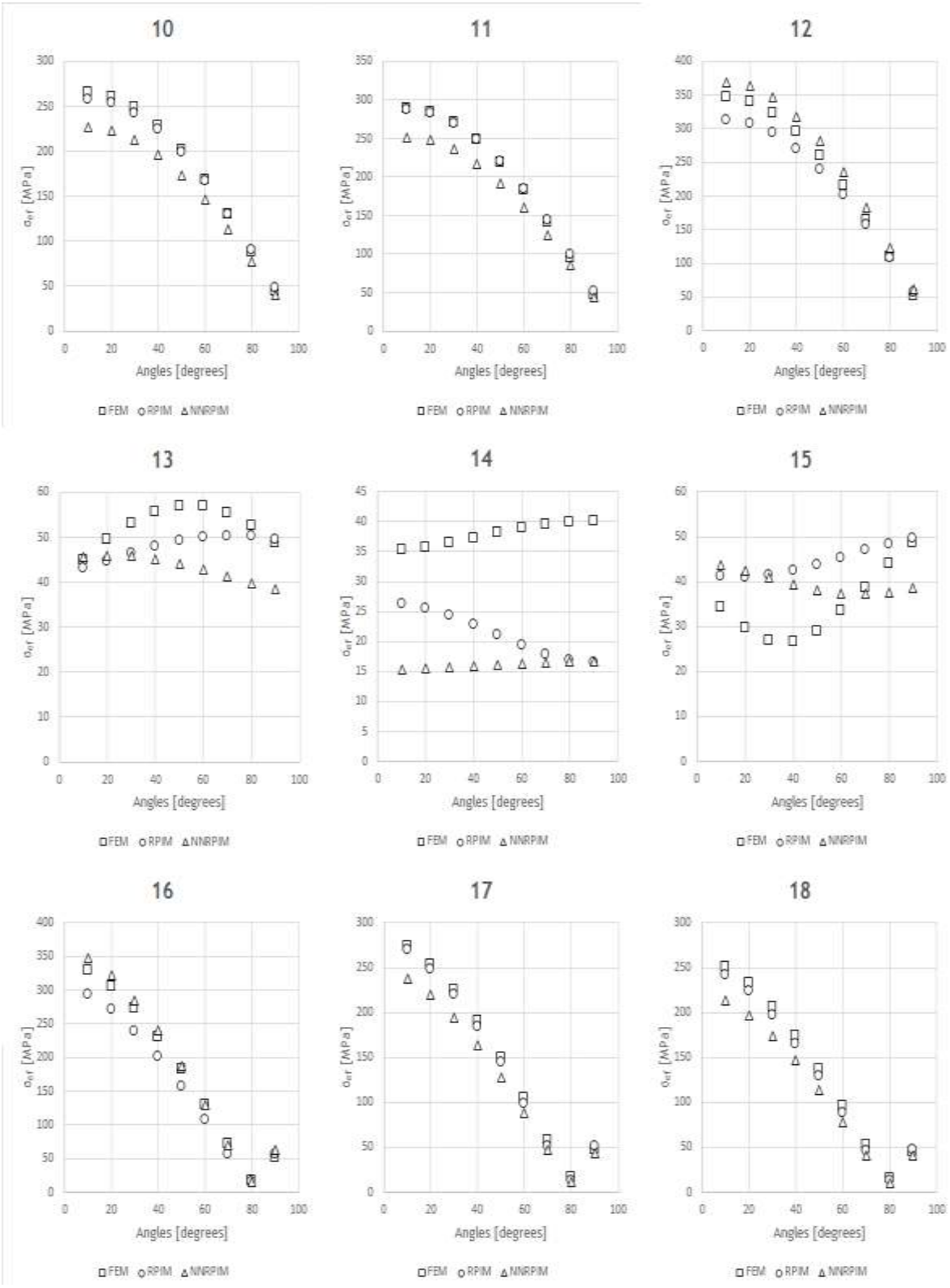

Figure A.48 Discrete stress values for type of bone 5, 'Model 1' and from implant side

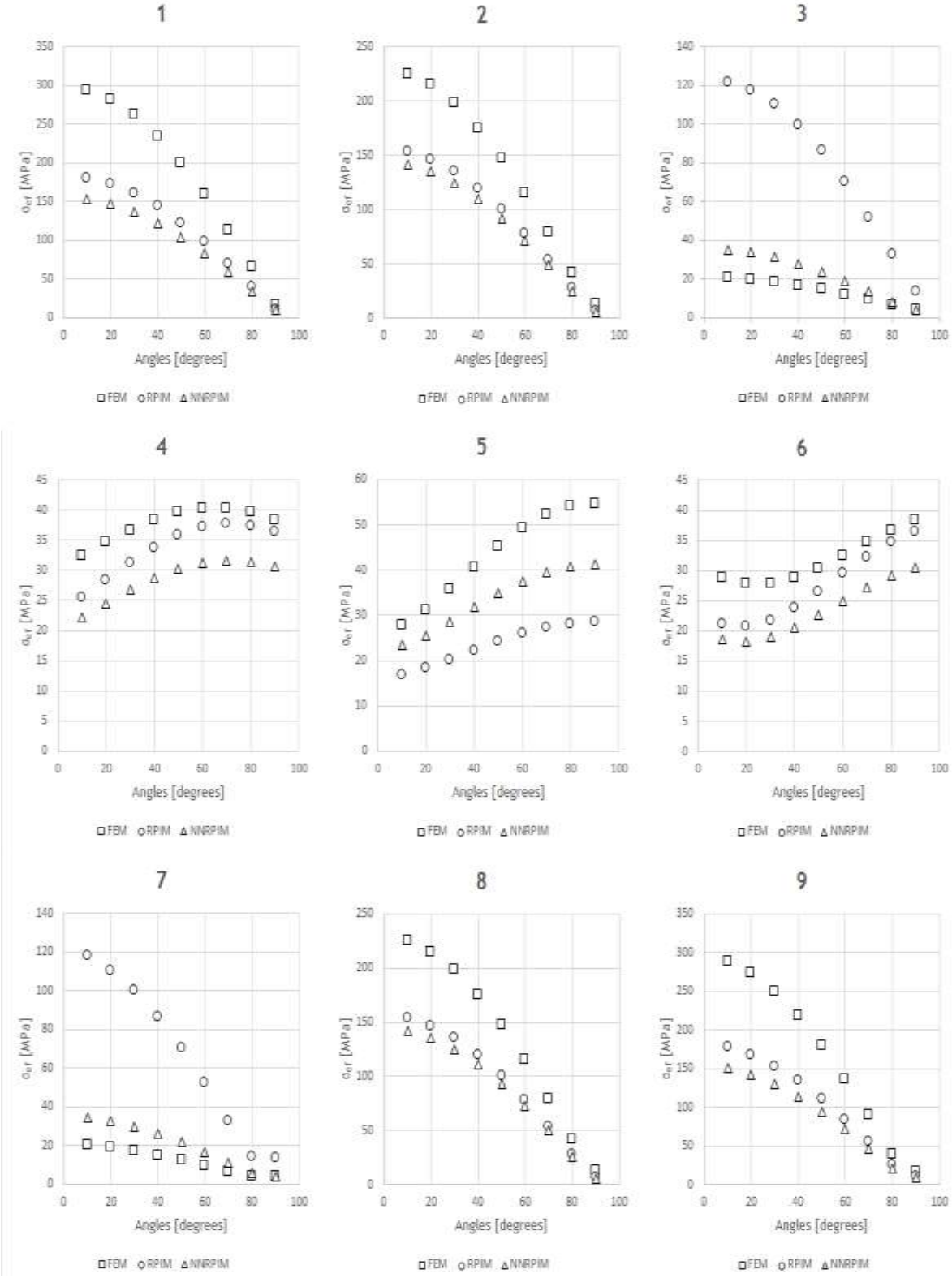

Figure A.49 Discrete stress values for type of bone 5, 'Model 2' and from bone side

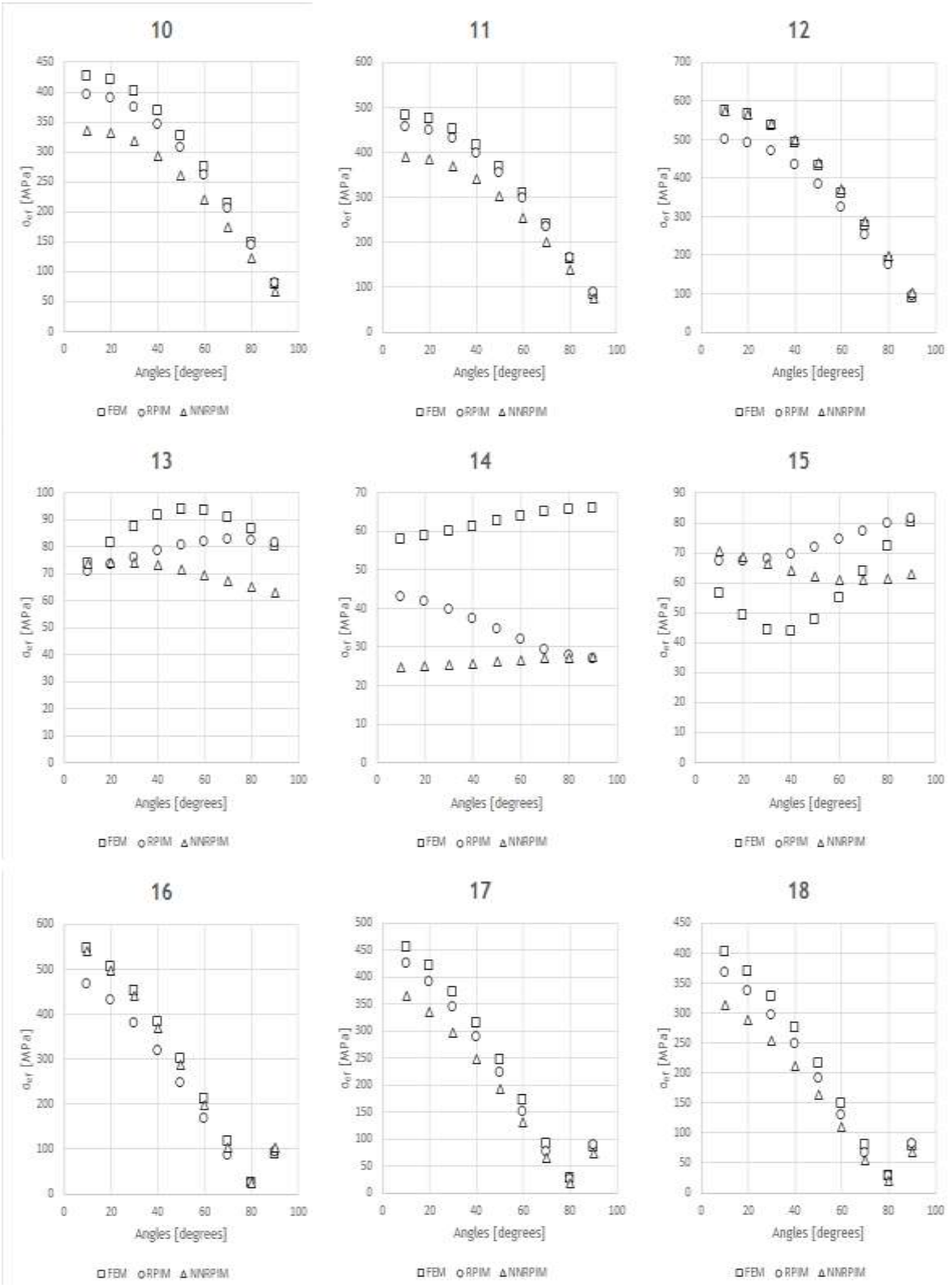

Figure A.50 Discrete stress values for type of bone 5, 'Model 2' and from implant side